UNIVERSITY OF ALBERTA

Investigation of Material and Optical Properties of Erbium-Doped Sputtered Glass Films

by

David W. Olsen ©

A thesis submitted to the Faculty of Graduate Studies and Research in partial fulfillment of the requirements for the degree of Master of Science

DEPARTMENT OF ELECTRICAL AND COMPUTER ENGINEERING

EDMONTON, ALBERTA, CANADA

SPRING, 1998

National Library of Canada
Acquisitions and Bibliographic Services
395 Wellington Street
Ottawa ON K1A 0N4
Canada

Bibliothèque nationale du Canada
Acquisitions et services bibliographiques
395, rue Wellington
Ottawa ON K1A 0N4
Canada

Your file Votre référence

Our file Notre référence

The author has granted a non-exclusive licence allowing the National Library of Canada to reproduce, loan, distribute or sell copies of this thesis in microform, paper or electronic formats.

L'auteur a accordé une licence non exclusive permettant à la Bibliothèque nationale du Canada de reproduire, prêter, distribuer ou vendre des copies de cette thèse sous la forme de microfiche/film, de reproduction sur papier ou sur format électronique.

The author retains ownership of the copyright in this thesis. Neither the thesis nor substantial extracts from it may be printed or otherwise reproduced without the author's permission.

L'auteur conserve la propriété du droit d'auteur qui protège cette thèse. Ni la thèse ni des extraits substantiels de celle-ci ne doivent être imprimés ou autrement reproduits sans son autorisation.

0-612-28972-9

Canada

University of Alberta

Faculty of Graduate Studies and Research

The undersigned certify that they have read, and recommend to the Faculty of Graduate Studies and Research for acceptance, a thesis entitled *Investigation of Material and Optical Properties of Erbium-Doped Sputtered Glass Films* submitted by David William Olsen in partial fulfillment of the requirements for the degree of Master of Science.

Steven Dew
Dr. S.K. Dew

Robert Fedosejevs
Dr. R. Fedosejevs

M Brett
Dr. M. Brett

J McMullin
Dr. J. McMullin

D Ivey
Dr. D. Ivey

Abstract

In this thesis, material and optical properties of sputtered erbium-doped glass films were investigated through experimentation and simulation. Erbium-doped glass is of interest for integrated optics applications because it exhibits a luminescent electronic transition near 1540 nm when excited by a 980 nm laser source. This can be utilized in all-optical waveguide amplifiers operating in the 1550 nm telecommunications window. The film properties studied include spontaneous emission as well as film adhesion, glass microstructure, and spatial uniformity of film thickness and refractive index. It was found that some of the films exhibited spontaneous emission and that this was often improved if the substrates were either heated during deposition or annealed after. It was also found that the refractive indices of some of the films sputtered from bulk glass targets increased from the centre of the wafer out to the radial edge. A wavelength dispersive microprobe was used to show that the concentration of heavy elements correspondingly increased outward toward the edge of the film.

Acknowledgements:

I would firstly like to express my gratitude to my research supervisor, Dr. Steven Dew, who has granted me a large degree of academic freedom over the course of this Masters program yet always seemed to steer me in the right direction. His financial assistance was also greatly appreciated and needed. Also, I am indebted to Dr. James Broughton who has been extremely generous with his time and experimental guidance at the Alberta Microelectronic Centre. Many thanks go out to Madhu Krishnaswamy, as well, who provided invaluable expertise with the laser system at TR Labs.

My program would not have been possible without the generous financial assistance of the Alberta Microelectronic Centre, so I would like to personally thank Chris Lumb and Graham McKinnon for this. I would also like to express thanks to TR Labs in Edmonton for use of their laser equipment and to Dr. Jim McMullin who was always available to field technical and theoretical questions.

I would also like to thank Dr. M. Brett and Dr. D. Koval in the Electrical Engineering Department at the University of Alberta, Dr. B. Heinrich at Simon Fraser University, Cyrus Shafai, Lianne Lester, Chris Backhouse, Nelson Poon, Ken Westra, Dino Corraza, David Clegg, Blair Harwood, George Braybrook, Paul Wagner, Lang Xi, the staff of the Spectral and Analytical Services Departments at the University of Alberta for providing their expertise and guidance, and Dr. D. Ivey for sitting on my defense committee.

I will never forget the faith that my parents, brother, sister, and friends have shown in me through this degree program and over the course of my life. Finally, I would like to thank Zoe Chatten for helping me start this program off on the right foot.

TABLE OF CONTENTS

Chapter 1. INTRODUCTION		1
1.1	Background	2
1.2	Optical Waveguiding Films	3
1.3	Sputter Deposition of Glass Films	9
1.3.1	Basic Sputtering Theory and Practice	9
1.3.2	RF Sputtering Method	11
1.3.3	Bipolar Pulsed DC Sputtering Method	11
1.3.4	Sputtering Multiple-Component Glass Targets	13
1.3.5	Sputtered Film Microstructure	14
1.4	Spontaneous Emission In Erbium-Doped Glass Films	16
1.4.1	Deleterious Effects Which Degrade Optical - Activity in Erbium Doped Films	18
1.4.2	Examples of Past Successes In Achieving Spontaneous Emission From Erbium-Doped Films	20
1.5	Organization of Thesis	21
Chapter 2. EXPERIMENTAL AND THEORETICAL CONSIDERATIONS		24
2.1	Introduction	25
2.2	Deposition System	25
2.2.1	Vacuum Chamber and Magnetron Assembly	25
2.2.2	Targets Used	26
2.2.3	RF Power Supplies	28
2.2.4	Bipolar Pulsed DC Power Supply	28
2.2.5	Substrate Heater And Film Annealing Equipment	29
2.3	Film Characterization Methods	34
2.3.1	Film Oxidation	34
2.3.2	Film Quality	35
2.3.3	Film Chemistry	35
2.3.4	Film Thickness and Refractive Index	37
2.3.5	Optical Absorption and Spontaneous Emission	38
2.4	Thin Film Simulation Tools - *SIMSPUD™* and *GROFILMS*	38
2.4.1	SIMSPUD™ *(SIMulation of SPUtter Distributions)*	38

2.4.2	GROFILMS *(GRain Oriented FILm Microstructure Simulator)*	41
2.4.3	Personal Objectives and Recognition of Approximations	42
2.5	Fabricating Raised-Ridge Waveguides	43
Chapter 3:	**EXPERIMENTAL RESULTS: Material Properties of Sputtered Glass Films**	48
3.1	Introduction	49
3.2	Deposition Conditions	49
3.3	Forming Glass Films on Silicon Substrates	53
3.3.1	Film Adhesion Problems	53
3.3.2	Film Oxidation	55
3.3.3	Film Quality	56
3.4	Film Thickness Profiles	57
3.4.1	Films From Fused Quartz Targets	57
3.4.2	Films From Erbium-Doped Bulk Glass Targets	60
3.4.3	Films From Powder Metal Targets	65
3.4.4	Summary from Thickness Measurements	67
3.5	Film Microstructure	67
3.5.1	Films From Fused Quartz Targets	68
3.5.2	Films From Erbium-Doped Bulk Glass Targets	73
3.5.3	Films From Compressed Powder Metal Targets	75
3.6	Annealing the Glass Films	76
3.6.1	Tube Furnace Annealing	76
3.6.2	Rapid Thermal Annealing (RTA)	78
3.7	Film Refractive Index Profiles	79
3.7.1	Films From Fused Quartz Targets	79
3.7.2	Films From Erbium-Doped Bulk Glass Targets	81
3.7.3	Films From Conductive Powder Targets	84
3.7.4	Summary From Refractive Index Measurements	87
Chapter 4.	**INVESTIGATION INTO RADIAL REFRACTIVE INDEX INCREASE IN ERBIUM-DOPED FILMS**	88
4.1	Introduction	89
4.2	Film Density Investigation	90
4.2.1	Density Measurements	90

4.2.2	Microstructure	92
4.3	Stoichiometry Variation	93
4.4	Films Deposited on Rotating Substrates	98

Chapter 5: INVESTIGATION INTO LIGHT ABSORPTION AND SPONTANEOUS EMISSION IN BULK GLASS AND FILMS 102

5.1	Introduction	103
5.2	Experimental Tools and Methodologies	104
5.2.1	Pump Absorption and Spontaneous Emission	104
5.2.2	Optical Test Bench	105
5.3	Examples of Some Waveguide Images	108
5.4	Experimental Results: Light Absorption In Bulk Glass and Films	110
5.4.1	Absorption In Bulk Glass Targets: *(from spectraphotometry)*	110
5.4.2	Absorption In Film PT00(3%): *(from spectraphotometry)*	111
5.4.3	General Absorption Measurements In All Films: *(using the optical test bench)*	113
5.5	Experimental Results: Spontaneous Emission Testing	117
5.5.1	Spontaneous Emission From 3% Erbium-Doped Bulk Glass *(using Bomen DA8 Infrared Interferometer)*	118
5.5.2	Spontaneous Emission From Unpatterned Film Slabs: *(using optical test bench)*	119
5.5.3	Spontaneous Emission From Ridge Waveguides: *(using optical test bench)*	120
5.6	General Discussion On Optical Activity of Films	126

Chapter 6. CONCLUSIONS 129

References: 132

APPENDIX A	Prism Coupler Operating Principles	140
APPENDIX B	Multiple-Oxide Film Simulation Procedure	147
APPENDIX C	Calculation Procedure For Uncertainty In Microprobe Data	151

LIST OF TABLES

Table 2.1	Some basic physical properties for the two erbium-doped glass targets.	27
Table 3.1	This is the labeling scheme used to identify the major films deposited in this thesis and the major run parameters associated with them.	50
Table 3.2	Several measured parameters for the RF sputtered films.	52
Table 3.3	Several measured parameters for the bi-polar pulsed DC sputtered films.	52
Table 3.4	Difference in film thicknesses of real and simulated films.	59
Table 3.5	Stoichiometry of source as determined by microprobe. Oxygen, boron, lithium, and chlorine impurities are not accounted for.	63
Table 3.6	Film thickness decrease fractions for real and simulated films.	65
Table 3.7	Specific annealing condition data for Er 1% film.	77
Table 4.1	Films chosen for Chapter 4 density assessment.	91
Table 4.2	Elemental stoichiometry analysis from the microprobe spectra.	95
Table 4.3	Stoichiometic summary for the oxides detected.	95
Table 5.1:	Summary table of films studied in this chapter.	104
Table 5.2	Throughput contrast and backscattered spontaneous emission test results.	115

LIST OF FIGURES

Figure 1.1	Conceptual example of a hybrid photonic electronic integrated circuit, OEIC.	3
Figure 1.2	Asymmetric planar slab waveguide.	4
Figure 1.3	Potential defects in waveguiding structures.	5
Figure 1.4	Raised ridge waveguide structure.	6
Figure 1.5	Waveguiding slab (a) versus patterned ridge waveguides (b).	
Figure 1.6	Schematic view of a magnetron-type sputtering system.	10
Figure 1.7	Ideal (a) and more realistic (b) target voltage waveforms for bipolar pulsed DC sputtering of conductive targets	12
Figure 1.8	Sputtered film microstructure.	14
Figure 1.9	Thornton zone structure model for the temperature and pressure-dependence of film microstructure.	16
Figure 1.10	Schematic representation of the energy levels and transitions associated with 980 nm optical excitation of Er^{3+} from ground state and the spontaneous and stimulated photon emission that results.	17
Figure 1.11	(a) Author's sketch of "expected" spontaneous emission spectra from 980 nm pumped erbium-doped glass (b) Desired exponential decay waveform of the chopped light through the slabs.	18
Figure 2.1	Multi-purpose vacuum sputtering system used for all sputter depositions.	26
Figure 2.2	Actual bi-polar pulsed DC waveforms using the ENI DCG-100 power supply.	29
Figure 2.3:	Schematic of heater assembly.	31
Figure 2.4	(a) Plane view of quartz film covered with voids and ejecta of various sizes. (b) Cross section of nodule growth resulting from the ejecta landing on surface.	32
Figure 2.5	Oscillation envelope of the bipolar pulsed DC waveform once heater is engaged.	34
Figure 2.6	Emission profiles that were used in the simulations.	40
Figure 2.7	Target erosion profile that was used in all simulations.	40
Figure 2.8:	Waveguide fabrication sequence.	46
Figure 2.9	Raised ridge waveguides patterned using Mask 2.	47
Figure 2.10:	Simulated modal shaped in ridge waveguides.	47
Figure 3.1	SEM photographs of (a) poorly adhering film and (b) properly adhering film.	55
Figure 3.2	A typical "speckle"	57
Figure 3.3	Film thickness profiles for films PT00(QZ) to PT11(QZ) sputtered from fused quartz glass targets, profiled using the prism coupler at 632.8 nm.	58
Figure 3.4	Simulated SiO_2 films overlaid with real films.	59

Figure 3.5 Film thickness profiles for films PT00(1%) to PT11(1%) sputtered from 1% erbium-doped bulk glass targets, profiled using the prism coupler at 632.8 nm. 61

Figure 3.6 Film thickness profiles for films PT00(3%) and PT10(3%); comparison of prism coupler output at 632.8 and 1550 nm. 62

Figure 3.7 Film thickness profiles for films PT00(3%) and PT10(3%); comparison of prism coupler output at 632.8 and 1550 nm. 62

Figure 3.8 Composite film thickness profiles for the glass films, PT00(3%) to PT11(3%). 64

Figure 3.9 Film thickness profiles for films PT10(AlSi_RF) and PT10(AlSi_bDC). 65

Figure 3.10 Film thickness profiles for films erbium-doped powder target glass. 66

Figure 3.11: Film 1 *(PT00)* at 40,000 times magnification. 69

Figure 3.12: Film 2 *(PT01)* at 40,000 times magnification. 69

Figure 3.13: Quartz target Film 3 *PT10* at 20,000 times magnification. 70

Figure 3.14: Quartz target Film 4 *PT11* at 20,000 times magnification. 70

Figure 3.15: GROFILMS simulation and actual film microstructure superimposed. 72

Figure 3.16 Cross section of PT11(1%) (deposited onto a flat substrate. 74

Figure 3.17 Cross section of PT11(1%) (deposited at an 80° angle). 74

Figure 3.18 PT11(1%) deposited at 80° and definition etched in 50:1 BOE. 74

Figure 3.19 SEM cross sections of RF and bipolar pulsed DC-sputtered films. 75

Figure 3.20 Voids in 1% Er-doped glass films created by annealing. 78

Figure 3.21 SEM of PT00(3%) waveguide array RTA'd for 30 seconds at 700°C. 79

Figure 3.22 Refractive index profiling for the quartz glass at 632.8 nm. 81

Figure 3.23 Refractive index profiling for the 1% erbium-doped glass at 632.8 nm. 82

Figure 3.24 Refractive index profiling for the 3% erbium-doped glass at 632.8 nm. 82

Figure 3.25 Refractive index profiling for the 3% erbium-doped glass at 1550 nm. 84

Figure 3.26 Refractive index profiles for the undoped glass films sputtered from metallic alumino-silicate powder pressed targets. 85

Figure 3.27 Refractive index profiles at 632.8 nm for Er-doped glass films sputtered from metallic alumino-silicate powder pressed targets. 86

Figure 3.28 Refractive index profiles at 1550 nm for Er-doped glass films sputtered from metallic alumino-silicate powder pressed targets. 86

Figure 4.1 Film density/refracive index correlation curves for the three chosen films. 92

Figure 4.2 Microprobe spectra from stoichiometric investigation. 94

Figure 4.3 Elemental concentration differentials plotted with respect to atomic mass 96

Figure 4.4 Comparison of simulated thickness profiles for La and Na with PT00 conditions 98

Figure 4.5 Rotating substarte tray assembly. 99

Figure 4.6 Thickness and refractive index profiles *on* and *off-axis* for films PT00(3%) and PT11(3%) deposited onto a continually sweeping substrate 100

Figure 5.1: Optical bench set-up used to test pump absorption and spontaneous emission. 106

Figure 5.2 Sample SEMs of PT00(3%) waveguides. 108

Figure 5.3 Sample SEM of PT10(3%) waveguide. 109

Figure 5.4 SEM of PT10(ErAlSi_RF) waveguide. This waveguide looks like all the other films made from powder targets. 109

Figure 5.5 Spectral Transmission scan and manufacturer's data for of the Er 1%, Yb co-doped target 110

Figure 5.6: Spectral Transmission scan and manufacturer's data for of the Er 3%-doped target. 111

Figure 5.7: Reflection scans of the uncoated quartz substrate as well as film PT00(3%) taken from 11,000 to 2500 cm^{-1}. This corresponds to 909 to 4,000 nm) 112

Figure 5.9: Spontaneous emission from 3% erbium-doped glass target. Measurement were performed with a Bomen DA8 Infrared Interferometer at Simon Fraser University. 117

Figure 5.10: Chopped beam and spontaneous emission decay. (decay lifetime τ) 118

Figure 5.10 Monochrometer output from film PT00(3%)_thick. The peaks suggest that spontaneous emission is occurring. 119

Figure 5.11 Oscilloscope traces of chopped pump beam and signal through the erbium-doped glass slab. 119

Figure 5.12 Waveguide output spectra from Film PT00(3%) pumped at 974 nm. Spontaneous emission peaks are observed between 1530 and 1550 nm. 121

Figure 5.13 Waveguide output spectra from Film PT00(3%) pumped at 978 nm. Spontaneous emission peak observed around 1534 nm. 121

Figure 5.14 Waveguide output spectra from Film PT00(3%)_RTA pumped at 974 nm. Spontaneous emission peaks are observed between 1528 and 1540 nm. 122

Figure 5.15 Waveguide output spectra from Film PT00(3%)_RTA pumped at 978 nm. Spontaneous emission peak observed around 1534 nm. 122

Figure 5.16 Backscatter spectra from Film PT00(3%)_heat pumped over a range of input wavelengths. Spontaneous emission peaks are observed with 976 nm pump. 123

Figure 5.17 Waveguide output spectra from Film PT00(3%)_heat_RTA pumped at 978 nm. Spontaneous emission peak observed around 1534 nm. 123

Figure 5.18 Waveguide output spectra from Film PT00(3%) pumped at 978 nm. Spontaneous emission peak observed around 1534 nm. 124

Figure 5.19 Waveguide output spectra from Film PT1,1/3(ErAlSi_RF) pumped at 978 nm. Spontaneous emission peak observed around 1533 and 1538 nm. 124

Chapter 1:

INTRODUCTION:

1.1 Background:

The wide-spread proliferation of the Internet over the past few years has fueled an unprecedented demand for communications bandwidth. As a result, traditional electronics and metallic telecommunication networks are quickly becoming an "information bottleneck" that cannot handle the data rates that many multi-media applications will require. Optical communication systems, on the other hand, offer a solution to this problem. If optical fibres were, for instance, run directly into the home or office then extremely high data rates could be achieved at the destination hardware.[1] In order to implement such a system, integrated optical and electronic circuitry would have to be in place at both ends of the fibre in order to handle such signal processing applications as optical signal modulation, interconnection, switching, routing, and amplification.[2] On-chip amplification is important in order to minimize the effects of light loss on integrated optics chips.

The concept of "Integrated Optics" was proposed in 1969 by S.E. Miller of Bell Laboratories.[3] It is a burgeoning discipline within the spectra of semiconductor and telecommunications engineering, the ultimate purpose of which is to develop integrated circuits which can propagate and manipulate optical information signals. An optoelectronic integrated circuit, or OEIC, is a thin film circuit in which optical and electronic devices are integrated onto a single substrate, usually silicon.[4] Such devices include laser diodes, detectors, switches, transistors, and waveguide interconnections. The motivation for research in this field is, in essence, to create chips which facilitate high speed computing by keeping the information in optical form as long as possible. A conceptual schematic of a simple hybrid photonic/ electronic chip is shown in Figure 1.1.

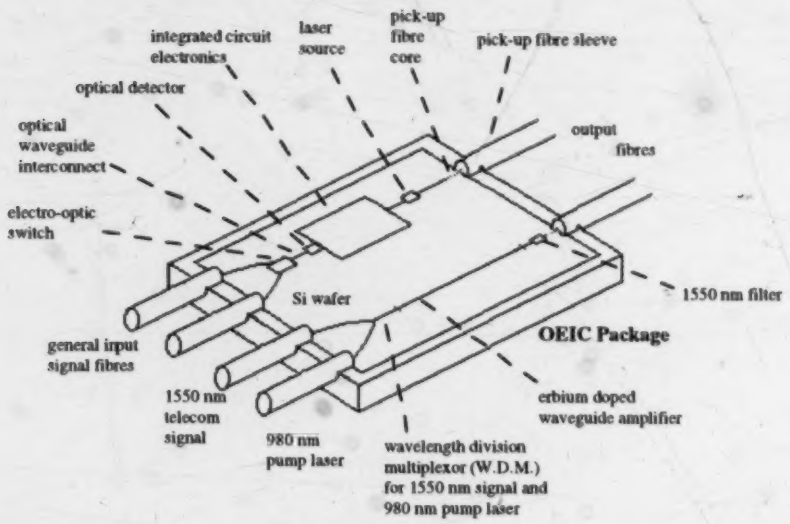

Figure 1.1 Conceptual example of a hybrid photonic electronic integrated circuit, alternatively referred to as an OEIC, opto-electronic integrated circuit.[5]

1.2 Optical Waveguiding Films:

An essential element in any integrated optics device is the thin film optical waveguide which provides the optical pathways necessary to distribute light signals on the chip. A waveguide is formed when a high index material is surrounded on either side by two lower index layers. Light will be confined in the middle "guiding" layer if the angle of incidence with respect to the waveguide/cladding interface exceeds the critical angle for total internal reflection. The critical angle is defined as

$$\Theta_{critical} = \arcsin(n_{air}/n_{film}) \qquad (1.1)$$

and is illustrated for the waveguide/air interface in Figure 1.2.[6]

If this condition is maintained, then electromagnetic modes will propagate through the guide. If not, then light will escape as radiative modes. The higher the index of the guiding region with respect to its neighboring adjacent layers, the tighter the mode will be confined.[7]

There has been considerable research into waveguides for integrated optics in recent years, and silica-based glass has emerged as a prime candidate to meet the objectives.[4][8-11] The

reasons are as follows: Firstly, silicon dioxide occurs in abundance in nature and is relatively inexpensive and simple to process. In addition, its high transparency from UV to near IR and its amorphous structure make it a low loss medium with a high degree of insensitivity to light polarization.[12] Further, it can easily be doped with network modifying impurity elements that can be used to either raise the refractive index of the glass or to transform it into an optically "active" medium.

Erbium, a rare earth element, is the dopant of primary interest in this thesis. In general, silica glass is an excellent host material for rare-earth oxides, however, it cannot incorporate them in amounts greater than about 1000 ppm and still provide effective photoluminescence.[13] Increasing the erbium concentration above this level introduces a very serious complication for waveguide amplifier production. That is, ion interactions cause the erbium to segregate into "clusters" which degrade amplifier performance.[14] In Section 1.4 the related problems will be discussed.

The simplest practical example of a waveguide is an asymmetric slab structure, composed of a high-index dielectric waveguiding layer on top of a lower index SiO_2 cladding layer. An example is shown in Figure 1.2. Air acts as the upper cladding.. The SiO_2 cladding layer is usually deposited using CVD, or chemical vapour deposition.

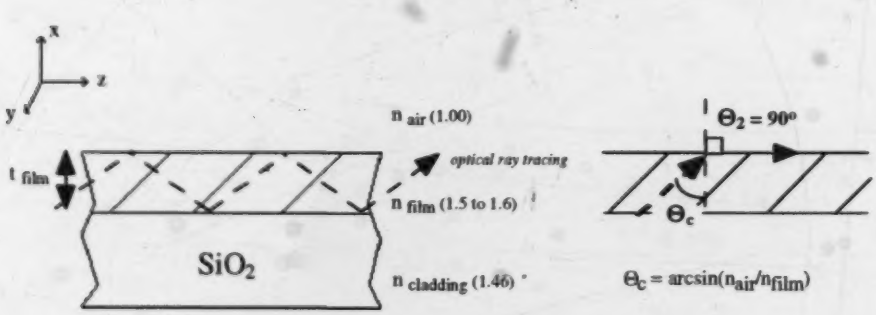

Figure 1.2 Asymmetric planar slab waveguide. ($n_{film} > n_{cladding} > n_{air}$) Critical angle for total internal reflection

Film imperfections such as porosity, refractive index and thickness inhomogeneity, optical absorption, and surface roughness, can promote radiative losses in a waveguiding film. Some common loss mechanisms are shown in Figure 1.3.

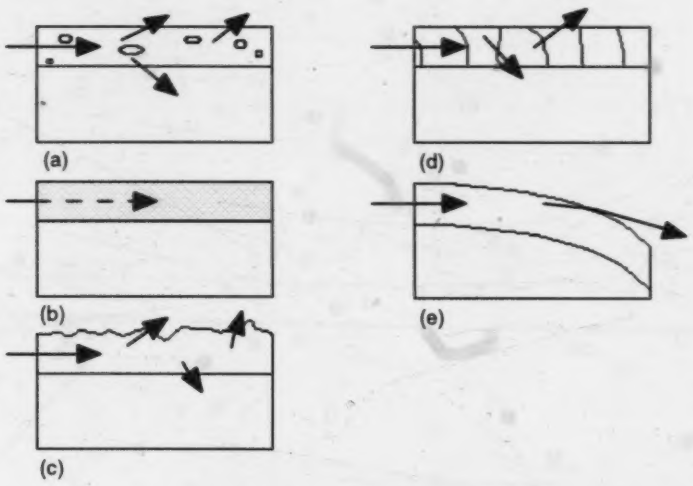

(a) Bulk scattering from defects caused by clusters, compositional gradients, voids, or refractive index discontinuities.

(b) Loss from photoabsorption.

(c) Surface roughness or large-scale defects and cracks.

(d) Scattering from microstructure column boundaries.

(e) Thickness and refractive index variation.

Figure 1.3 Potential defects in waveguiding structures that can all promote light intensity decrease in a guided beam. [15]

Raised Ridge Waveguides:

Originally, it was hoped that waveguide patterning could be avoided entirely in this thesis. The goal was to test the optical properties of plain slabs and draw correlations between deposition conditions and spontaneous emission characteristics. Even though one film slab was successfully tested for spontaneous emission, it was found that some method of laterally confining the light was generally required in order to minimize losses in thin film waveguides. The rectangular dielectric film waveguide is the most common way to achieve this goal.[15]

Rectangular dielectric film waveguides are relatively easy to pattern and provide tight modal confinement.[15] An example of a rectangular *raised ridge* structure, fairly typical of the ones fabricated in this thesis, is shown in Figure 1.4.

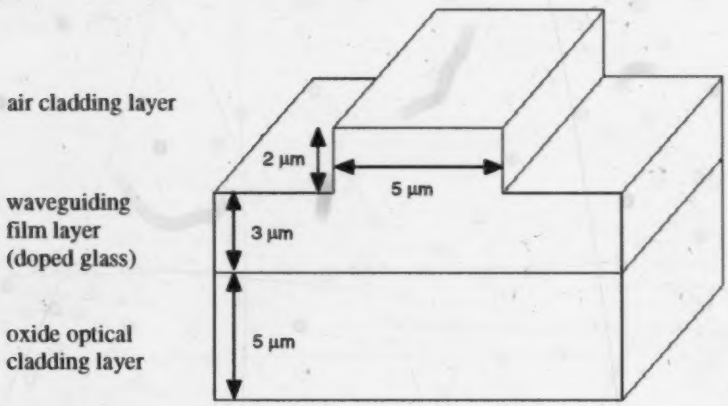

Figure 1.4 Raised ridge waveguide structure.

Lateral mode confinement is particularly important for light that is launched into waveguides from fibres since the natural tendency of a beam to diverge out of the tip (refer to Figure 1.5). The maximum angle of spread (or acceptance) is given by

$$\Theta_{max} = \sin^{-1} [1/ n_{air} \times NA], \qquad (1.2)$$

where "NA" is the numerical aperture of a step-index fibre and is equal to

$$NA = (n_{film}^2 - n_{SiO_2}^2)^{1/2}. \qquad (1.3)\ [6]$$

Without a mechanism for lateral mode confinement, a beam launched from a fibre may spread out to such an extent as it propagates forward through the film that a pick-up fibre at the output only captures a small fraction of its power. This leads to inefficient throughput and high loss. This must be minimized in integrated optics devices. The situation is illustrated in Figure 1.5.

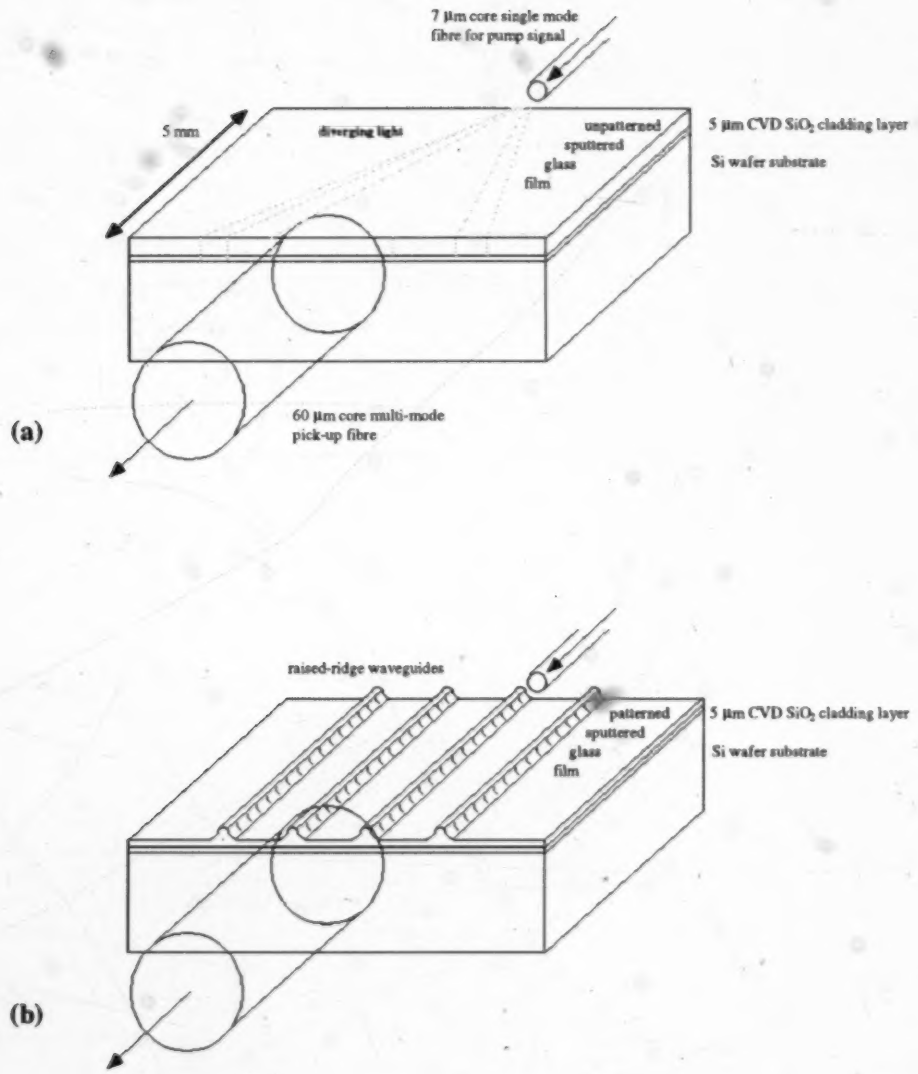

Figure 1.5 Waveguiding slab (a) versus patterned ridge waveguides (b). Lateral mode confinement is improved through waveguide patterning. This reduces light loss at the pick up fibre.

Raised ridge waveguides are made by selective etching. This is accomplished by first spinning photoresist onto a wafer and then transferring a waveguide mask pattern into the photoresist using photolithography. Etching of the exposed surface is often performed using BOE (buffered oxide etch). Its primary constituent is hydrofluoric acid, HF - a common glass etchant. Depending on the type of glass being etched, the process can often, unfortunately, lead to considerable surface roughness and light loss, especially if the material is composed of many different oxides.

Erbium-Doped Films:

The purpose of this thesis research was to study erbium-doped sputtered glass films. Erbium-doped glass is of particular interest in integrated optics because the trivalent ion, Er^{3+}, exhibits a spontaneous or stimulated luminescent transition at a wavelength near 1540 nm when excited with a 980 nm (or 1480 nm) laser.[16] As a result, it can be utilized in all-optical amplifiers in the low-loss 1550 nm telecommunications window. (Only a 980 nm excitation source was considered in this thesis.) In principle, erbium-doped waveguide amplifiers have the potential to entirely eliminate the need for electronic repeaters on opto-electronic integrated circuit chips. The physics behind spontaneous and stimulated emission will be expounded upon more thoroughly in Section 1.4.

Erbium-doped *fibre* amplifiers, or *EDFA's*, are a fairly well understood technology and are already implemented in some long-haul fibre optic systems around the world.[17] EDFA's have been used, in fact, to send light signals over 1000 km without electronic regeneration. Individual amplifier gains of over 50dB have also been reported.[18] This is good news for telecommunications companies because EDFA's will simplify signal regeneration and reduce equipment and maintenance costs over the long run.[19]

Nonetheless, as of 1996, the highest gain per length reported in an Er^{3+} doped fibre was only 0.5 dB/cm.[20] As a result, an EDFA must stretch several meters in order to provide any significant gain. Waveguide amplifiers on silicon, on the other hand, are designed to be integrated onto reasonably small silicon chips so they are constrained to only a few centimeters. In order to get as much optical activity as possible, the erbium concentrations must be a few orders of magnitude higher in waveguides than in fibres or comparable optical amplification will not be achievable with a single device.[21][22]

1.3 Sputter Deposition of Glass Films:

A sputtering chamber at the Alberta Microelectronic Centre was used to deposit all waveguiding films described in this thesis. Sputtering is a highly flexible technology that offers a good degree of control over deposition conditions. It is also relatively simple and inexpensive, so it would be desirable if it could be utilized as a standard fabrication process for erbium-doped glass films. Other deposition processes considered include ion implantation, ion exchange, and chemical vapour deposition (CVD).

In the literature, some excellent spontaneous emission and decay lifetime results have been reported for erbium-doped optical waveguides produced from ion implantation and ion exchange.[23][24][25] The former technique was not used because the necessary equipment was not available at the Alberta Microelectronic Centre. Ion exchange was not investigated because that would have overlapped with some work being undertaken by Madhu Krishnaswamy, another graduate student in the department studying erbium-doped glass films.

Chemical vapour deposition, the other technique considered, is actually the most extensively used technique to deposit SiO_2 layers, and has successfully been used to fabricate rare-earth doped waveguides. [26] The process is very difficult, however. The reason for this can be explained by examining the processes involved. In chemical vapour deposition, film layers are deposited when gaseous reactants in a CVD chamber chemically interact at the surface of a substrate, leaving behind a desired solid product.[12] Dopants can be incorporated into the surface chemistry only as long as they can be chemically associated with volatile gas-phase molecules which can situate the dopant at the reaction surface and then preferentially remove themselves from the vicinity.[12] Unfortunately, heavy rare earth metals are uncommonly found in the gas phase. As a result, CVD seems a difficult method of forming rare-earth doped waveguides.

1.3.1 Basic Sputtering Theory and Practice:

In a sputtering chamber, a low pressure noble gas, typically argon, is ionized by energetic electrons near a high voltage cathode.[27] Argon ions accelerate toward the negative electrode until they collide with the target surface. Upon impact, if the kinetic energy is high enough,

target atoms will be ejected.[27] The plasma is sustained by secondary electrons that are also released from the target by electron impact ionization.[28] The angular distribution of the flux is roughly cosine-shaped with typical ejection energies of near 10 eV.[27][28]

Figure 1.6 displays a typical sputtering chamber. A film is made by positioning a substrate in front of the target in order to intercept some fraction of the ejected flux. In the fabrication sequence for optical waveguides, sputter flux lands directly on top of the SiO_2 cladding layer which was previously deposited using CVD. The target is usually pre-sputtered for 10-15 minutes with the substrate shutter closed while the magnetron power supply is slowly ramped up to full power. This minimizes the chances of target cracking due to thermal shock and also prevents unwanted target surface contamination from getting onto the film.

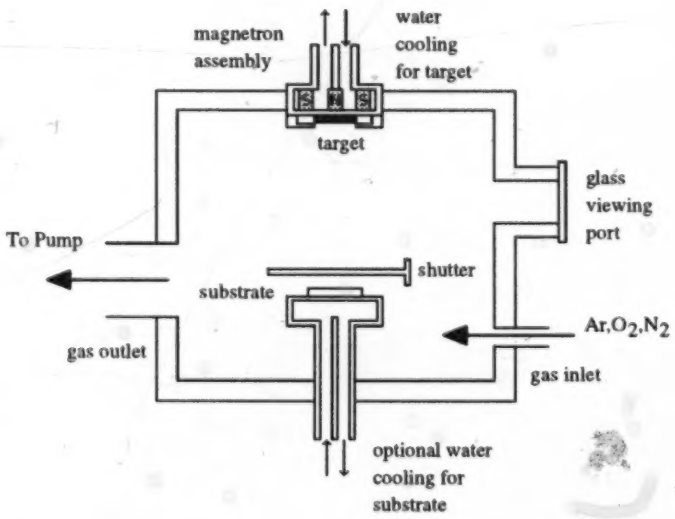

Schematic view of a magnetron-type sputtering system.

Figure 1.6

Target to substrate transport is usually assumed to be atomic or diatomic.[28] As a result, oxygen from the target compound can inadvertently be pumped away by the vacuum system before it reaches the substrate. Insufficient background oxygen can lead to compositional inconsistency between the target and film resulting in incomplete film oxidation.[29] The problem can be minimized by adding excess oxygen to the background gas in the chamber to ensure that it does not become a limiting reagent in surface re-combination. This technique is called *reactive sputtering* and was used throughout this thesis. One price of introducing oxygen in this manner is a reduced sputtering rate.

Dielectric films can be sputtered directly from insulating or metallic targets.[30] Metal targets have the advantage that they have higher thermal conductivity and are more durable, so they can be operated at higher powers without cracking. As a result, higher deposition rates can be achieved.[30] Dielectric targets can be RF sputtered either reactively or non-reactively; while metal targets must be strictly reactively sputtered using either an RF, DC, or bipolar pulsed DC source. "Bipolar pulsed DC" sputtering is a relatively new deposition technique that will be summarized shortly.

1.3.2 RF Sputtering Method:

Because direct current cannot conduct through a dielectric material, glass targets cannot be sputtered using DC. Instead, charge ends up building up on the surface and prevents sputtering from occurring. The standard way to overcome this is to use an RF power supply to capacitively couple the sputtering potential to the target surface. In the process, the electrode develops a negative "DC self bias" which allows sputtering to occur. This net DC sputtering voltage is approximately 5/12 of the peak RF voltage.[28]

1.3.3 Bipolar Pulsed DC Sputtering Method:

In this thesis a relatively new method of sputtering was investigated. It uses an asymmetric bipolar pulsed DC power supply to allow dielectric films to be reactively sputtered from conductive targets. It was originally developed as a superior alternative to reactive DC sputtering and boasts high deposition rates like reactive DC sputtering but produces films with higher uniformity and considerably fewer defects.[31]

The problem with basic DC reactive sputtering is that insulating compounds end up forming all over the chamber, substrate, and target surface. Since DC current cannot flow through these insulating layers, no sputtering can occur there, and the target is said to be "poisoned."[31] If it so happens that the insulating layers break down under the applied bias then arcing results, and unwanted debris sprays all over the films.[32] This often degrades their condition beyond what is tolerable for integrated optics applications.[31]

Arcing can be reduced significantly if asymmetric bipolar pulsed DC sputtering is employed.[31] It was designed to enable the capacitive insulating layers to be sputtered just before the target material and with a higher sputtering yield.[31] The process exploited is called "preferential sputtering" and will be explained as follows: Under forward bias, positively-charged argon ions accumulate on the insulating layers. As they do, the sputtering potential of the argon ions decreases by the amount of voltage built up across the resulting capacitor. The probability that the contaminated target will be sputtered is reduced as the charge builds up.

In bipolar pulsed DC sputtering, the applied target voltage is interrupted periodically with a (positive-valued) reverse bias in order to disperse built up charge and surface contamination. In steady state, electrons will accumulate on the insulating layers and charge them to - *Vrev*. At the precise moment the cathode is switched back to the original negative sputter voltage, the magnitude of the bias on the insulating layers becomes equal to *Vsput* + *Vrev*. Depending upon power supply settings, this value can be high enough to cause the insulating materials to be battered off by the extra-highly excited argon ions. In other words, the higher the voltage, thie higher the sputter yield. This helps minimize the chances of electrical breakdown and film contamination.[31]

Target waveforms for the generator and target are shown in Figure 1.7. Typical operation frequencies range between 80 to about 200 kHz.[31]

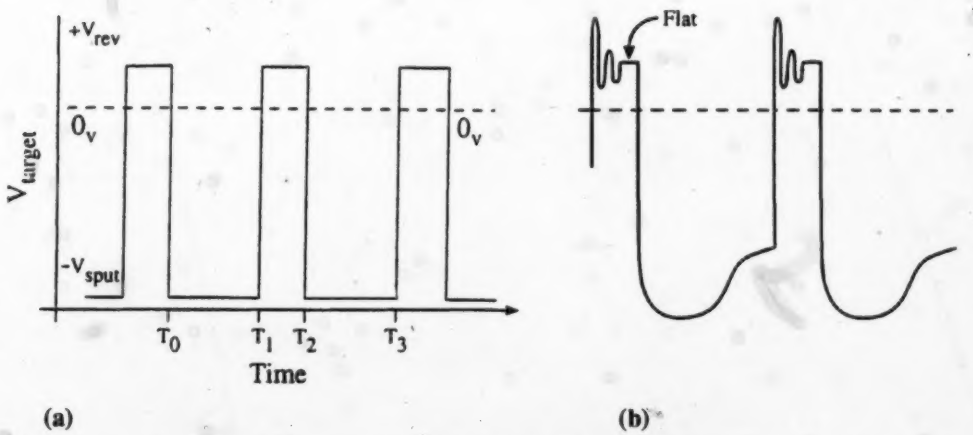

Figure 1.7 Ideal (a) [31] and more realistic (b) [32] target voltage waveforms for bipolar pulsed DC sputtering for conductive targets

Users of this technology have reported reactive sputter rates of 60% to 100% of the metallic deposition rate. and 1.75 times higher than reactive RF sputtering rates under identical conditions. Film uniformity also improves because the plasma is more energetic than an RF plasma. The explanation for this is that the plasma is sustained not only by the 10^2 kHz pulse frequency but also by the ultra high frequency harmonics generated from the sharp pulse edge transitions.[31]

1.3.4 Sputtering Multiple-Component Glass Targets:

Erbium-doped glasses are commercially available as RF sputter targets for experimental use. Typically, these targets are two inches in diameter and are composed of numerous materials, including silicates and other metal oxides. Such complex material composition poses some unavoidable obstacles to understanding and utilizing sputtering for waveguide applications.

It is well known, for instance, that different atoms display different *sputtering yields*.[29][33] Because of this, each species will evolve into the sputter flux at a different rate at a given target bias, and this could promote significant stoichiometric variation between the substrate and target. The effect is somewhat compensated for, however, because as one species is preferentially depleted from a target the others assume a higher fraction. As such, they have a higher likelihood of being sputtered.[33]

Another potential source of stoichiometric inconsistency is the variation in *sticking coefficients* of particles impacting a substrate surface.[12] The sticking coefficient is the probability that an incident molecule will be adsorbed on the surface of a film. If the sticking coefficient is not unity then incident molecules will deflect off the film when they collide with it. Like sputter yield, this property can vary significantly from element to element.[12]

Background pressure and throw distance are other sources of stoichiometric variation between the erbium-doped target glass and the film. Momentum considerations suggest that heavier species, like erbium, will arrive in disproportionately larger amounts relative to lighter species, like silicon. The lighter species are subject to more lateral deflection upon impact with background gas molecules and scatter more as a result. Thus, it seems that a lower percentage of

lighter elements would actually end up reaching the film.[34] The higher the pressure and longer the throw distance, the greater the opportunity this effect has to manifest itself.

1.3.5 Sputtered Film Microstructure:

In general, sputtered films exhibit columnar microstructure. This can be seen in the SEM cross section as well as the SIMBAD[34] film simulations shown in Figure 1.8. Broader columns were obtained by increasing the diffusion length parameter two and then three times from (a) to (b) to (c). SIMBAD will be summarized briefly in Chapter 2, as well.

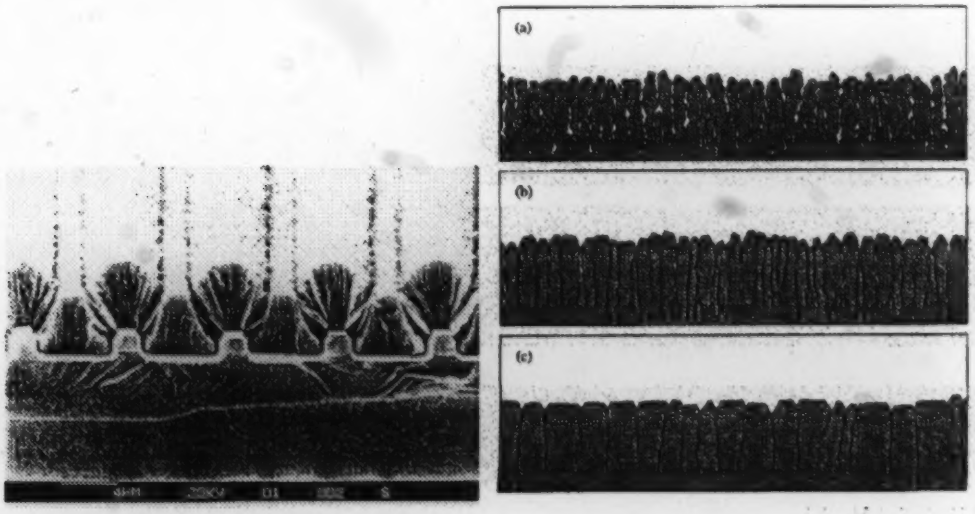

(a) Example of columnar film structure over topology

(b) Example of columnar film structure variation caused by increasing particle diffusion length by a factor of 2 and then 3

Figure 1.8 Sputtered film microstructure. (reproduced with permission of S.K. Dew [34])

Vertical film growth patterns arise primarily due to "self-shadowing" of portions of the deposited material by regions which have grown slightly higher. In other words, as the peaks grow, loftier ones get pelted with a greater proportion of the sputter flux than their neighbors. As a result, peaks grow upwards in a columnar fashion. Some material re-distribution may also

occur due to surface, bulk, and column boundary diffusion. The extent of this depends on material properties and temperature.

Since, in a thin film waveguide, guided light propagates perpendicular to the column boundaries, scattering losses will occur at columnar interfaces and gaps. As a result, light propagation is strongly-dependent on microstructure and, hence, on sputtering conditions.[36] The "Thornton Zone model" is a graphical index for how the structure of sputtered layers varies as a function of two such conditions, temperature and pressure (see Figure 1.9). Since glass materials do not display sharp melting points it should be understood that this indexing system is targeted primarily for polycrystalline materials. Nonetheless, its physical characterizations are still of some value.

"Zone 1" structure, which is representative of lower deposition temperatures and high pressure runs, is porous and has low density. At mid-scale temperatures in "Zone 2," more surface diffusion occurs, so the columns are more closely packed and possess higher density. At higher temperatures in "Zone 3" bulk diffusion becomes pronounced, and films take on a more granular form. "Zone T" structure is presumed to result from *re-sputtering* caused by negatively charged particles and energetic neutrals in the chamber. Under these conditions, the columns become dense and fibrous.[34]

Film microstructure is also important because it will affect how erbium ions segregate in the film. Boundaries between columns act as diffusion pathways for erbium atoms. At elevated temperatures, erbium can diffuse through these pathways and coalesce with other erbium atoms in segregated "clumps." Furthermore, at a certain level of erbium doping in the glass, the microscopic clusters can evolve into full-fledged crystalline phase growth.[37] Clearly, since erbium concentrations as low as 1000 ppm have been found to produce deleterious effects on photoluminescence,[38] film microstructure introduces a serious materials and device fabrication challenge to the development of integrated optic waveguide amplifiers.

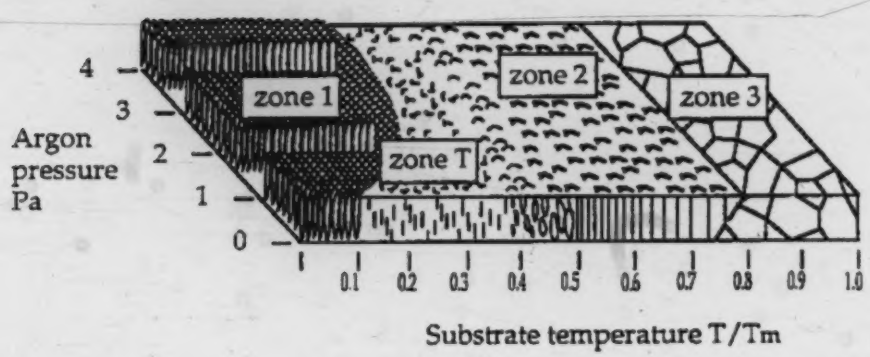

Figure 1.9 Thornton zone structure model for the temperature and pressure-dependence of film microstructure. (reproduced with permission of R.N. Tait) [39]
Note: 1 Pa = 7.5×10^{-3} torr

1.4 Spontaneous Emission In Erbium-Doped Glass Films:

The principle behind erbium-doped waveguide amplifiers can be explained in quantum mechanical terms. It has already been mentioned that erbium exhibits spontaneous luminescence near 1540 nm when the trivalent ion is pumped with a 980 nm or 1480 nm laser source. Optical "pumping" refers to the process whereby an electron is excited to a higher energy level through the absorption of a photon with energy $E = {}^{hc}/\lambda_{pump}$. Electronic transitions from the intra-4f orbital of the Er^{3+} ion produce infrared radiation when electrons decay to the ground state from a metastable energy level near 1540 nm.[23][40] It can be seen in Figure 1.10 that a 980 nm pump beam excites the electrons into the $I_{11/2}$ state where they rapidly decay to $I_{13/2}$. (A 1480 nm laser pumps electrons directly into $I_{13/2}$.) The band structure labeling-method is called "Russel-Saunders" notation.[41]

Figure 1.11(a) is an artistic rendering of a typical spontaneous emission spectra. The main reference for this figure was [42]. The dual peaks are thought to be a result of a "Stark splitting" of the 4f orbitals. Stark splitting of electron orbitals occurs due to the influence of electric fields. In the case of rare-earth-doped glass, the erbium ions are subject to electric fields from the other neighbouring atoms within the host matrix. These are called "crystal fields." [19]

With continued pumping, an electron population inversion is created at the metastable state. When a 1550 nm telecommunications signal passes through the doped medium, electrons are stimulated and decay to the ground state. As a result, photons are released. These photons add energy to a degraded information signal, thereby amplifying it. This process is called amplified stimulated emission, *ASE*, and is the basis of optical waveguide amplification.[17] In this thesis, with rare exception, only spontaneous emission was studied since it is a more fundamental film property.

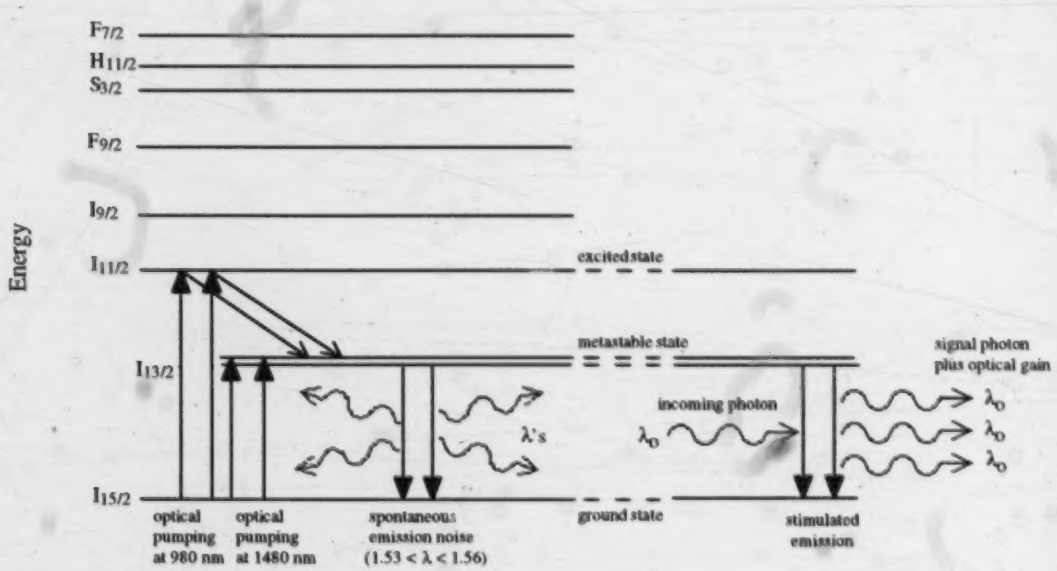

Figure 1.10 Schematic representation of the energy levels and transitions associated with 980 nm optical excitation of Er^{3+} from ground state and the spontaneous and stimulated photon emission that results. (compiled from [17][19][24][42][43])

There are a few important measures of a glass' degree of optical activity. Its ability to absorb an optical pump and fluorescence at the proper wavelength are the obvious ones. Another critical parameter for the success of optical waveguide performance is the lifetime of the metastable state. A long metastable lifetime is required to ensure that effective stimulated emission can occur. Transitions from the metastable state occur in two main types - radiative and non-radiative. It is, of course, radiative transitions that are of interest here.

Research has shown that the intrinsic 1/e lifetime of Er^{3+} is on the order of 10 ms.[22] In thin films, this value usually varies from microseconds to milliseconds depending on the composition and fabrication conditions of the glass.[43] The decay lifetime is exponential and can be measured by chopping the pump signal and measuring the light intensity at the output of the waveguide on an oscilloscope. An idealized example of this is shown in Figure 1.11 (b).

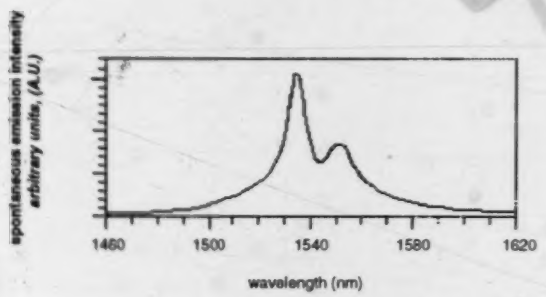

(a)

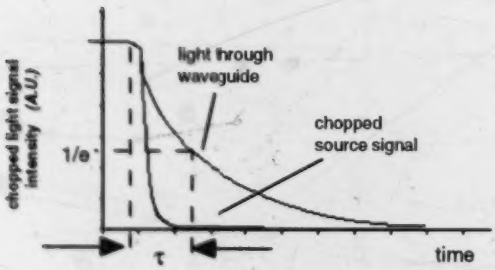

(b)

(a) Author's sketch of "expected" spontaneous emission spectra from 980 nm pumped erbium-doped glass (adapted from reference [19])

(b) Desired exponential decay waveform of the chopped light through the slabs.

Figure 1.11

1.4.1 Effects Which Degrade Optical Activity in Erbium-Doped Films:

As described earlier, the level of spontaneous emission that erbium-doped glass films exhibit is very sensitive to the erbium doping level. It has been concluded that even at fairly low levels

of erbium-doping, approximately 100 ppm, ion-ion interactions result in erbium clustering.[14] These significantly reduce the metastable state lifetimes and the spontaneous emission ability of the film. Cluster sizes have been estimated at between 4-6 ions, and they are deleterious to optical activity. In addition, close proximity erbium ions often interact such that one or both of the ions relax to the ground state without giving off a photon. Instead, they lose energy in the form of heat or by photon release at an undesired wavelength.[40][43][45][46] Some dissipative processes related to high concentration and will be summarized as follows:

Multi-Phonon Emission (thermal quenching):

One method of non-radiative relaxation is through multi-phonon emission. In this process, erbium electrons interact with the dynamic lattice of the glass host causing phonons to actually bridge the energy gap and lower the system into the unbleached state. According to reference [43], "the higher the energy of the phonons...the fewer are required to bridge the gap and the faster the non-radiative rate."[43] It is possible that laser-heating of a glass waveguide could exacerbate this problem.

Excited State Absorption (ESA):

Excited state absorption is another effect that can play a significant role in degrading amplifier performance at higher pump powers. In this process, an additional 980 nm pump photon is actually absorbed from $I_{11/2}$ rather than from $I_{15/2}$. This excites the erbium ion into the $F_{7/2}$ state. From there it decays rapidly to $S_{3/2}$ where it further decays back to ground. The photon released in this transition has a nominal wavelength of 550 nm. Since this wavelength is in the visible region of the electromagnetic spectrum, ESA can be identified by green light being emitted from the film.[19][43]

Upconversion:

Upconversion is believed to be the most significant inhibiting factor in Er-doped glass performance. In this process two close proximity ions that have already been excited to $I_{13/2}$ interact such that one transfers its energy to the other. As a result, the donor decays to the ground state non-radiatively, and the acceptor is excited up to $I_{9/2}$. This electron will most likely decay via multi-phonon emission back down to $I_{13/2}$.[43] It has been observed that a 980 nm photon is sometimes also emitted directly from $I_{11/2}$.[19] Again this effect is most dominant at

high pump powers and is manifested by very rapid, non-exponential decay and decreased amplifier gain.[43]

Possible Solutions:

There are several host glass modifiers that have been known to improve spontaneous emission characteristics. For instance, Al_2O_3 and phosphorous added to silica glass is an effective way to reduce clustering effects. [14][38][45][47][48] According to some sources, it increases the solubility of rare earths in a silica glass network.[38][47] In addition, ytterbium is often added to erbium-doped glass to increase pumping efficiency. Ytterbium has the effect of broadening the absorption band near 980 nm. [40][45][46] The metastable state of ytterbium is very close to erbium, and electrons energy transfer between them with reasonable efficiency.[49]

1.4.2 Examples of Past Successes In Achieving Spontaneous Emission From Erbium-Doped Films:

Several authors have actually reported achieving outstanding lifetimes of 10 ms or more in erbium-doped waveguide systems.[22][23][42][47][50][51] Three such examples will be discussed shortly. In several of these reports, it was further noted that spontaneous emission peak intensities and decay lifetimes are often enhanced by depositing the films onto heated substrates and/or by annealing them afterwards.[50][51]

Some examples of the fabrication techniques used include ion-exchange, ion implantation, and RF sputtering. Three particularly good examples of these three areas are Ohtsuki [47] at the University of Arizona who observed $I_{13/2}$ decay lifetimes of 8.4 ms and a sharp spontaneous emission peak near 1540 nm using dry silver-film ion exchange; A. Polman [23] of AT&T Bell Laboratories in New Jersey who also observed sharply-peaked photoluminescence spectra and between 6 and 15 ms lifetimes using ion-implantation, and J. Schmulovich [50] who has fabricated and characterized many RF-sputtered films with lifetimes of 2 to 15 ms.

Schmulovich's work is of particular interest because he used sputtering to obtain impressive spontaneous emission results. For example, he developed a 2.4 cm long, 6 μm wide, and 1.3^{+}/-0.1 μm thick optical waveguide amplifier that provided 0 dB throughput loss in a normally 21 dB-loss optical system. It was annealed in dry O_2 for 1 hour after deposition at 700°C. This

represents 126 times gain in optical power at the signal wavelength through the waveguide. The film was sputtered from a bulk glass target at 50 Watts with 3:1 argon to oxygen partial pressures at a 5 nm / minute deposition rate. It was pumped with a 125 mW, 975 nm pump beam. The decay lifetime was between 5 and 8 ms.[51] Owing to his success, some of his deposition conditions were adopted in this thesis.

1.5 Organization of Thesis:

Research Focus:

For several years prior to this thesis work, there had been work done at the University of Alberta on erbium-doped films. These experiments had met with varied levels of success, but none as pronounced as has been reported in the literature.[22][23][42][47][50] The relative lack of success at obtaining measurable spontaneous emission and decay lifetimes (especially in the face of the reported successes in the literature) was a major impetus for undertaking this thesis.

Several authors have stated that host glass composition and fabrication methods have a pronounced effect on amplifier performance. As a result, one of the intents of this research was to make basic, general, and specific observations / conclusions about how deposition conditions and target material affect erbium-doped sputtered glass films. Thus, the first experimental approach taken in this thesis was to fabricate and investigate some fundamental material properties of erbium-doped sputtered glass films.

The materials were chosen based on availability, and simulation and experimentation were both performed in order to promote understanding of the physical processes involved with sputtering erbium-doped glass films. It was not well understood, for instance, how the composition of films sputtered from multi-component targets differ from the target. Nor was it well understood how much microstructure sputtered glass films would exhibit. These effects are relevant because stoichiometric inconsistency or excessive microstructure could have detrimental effects on absorption, spontaneous emission, and light loss. To this end, different methods of sputtering dielectric materials were examined to see if deposition rates and/or optical activity could be improved.

The second approach came from an applications perspective. The goal was to produce optically active films that absorb 980 nm pump light and spontaneously re-emit in the far infrared near 1550 nm. The ultimate goal was not necessarily to obtain light *amplification* from the films. As mentioned previously, this was more in the graduate research domain of Madhu Krishnaswamy. Instead, it was to obtain spontaneous emission from the films, try to produce measurable lifetimes, and characterize the performance of the films with respect to fabrication conditions.

Chapter Breakdown:

Chapter 1:

Erbium-doped sputtered glass films were introduced and described within the context of hybrid photonic / electronic integrated circuits. The remainder of this chapter has discussed optical waveguide fundamentals, sputtering theory and techniques, film microstructure concerns, and spontaneous emission in erbium-doped glass materials.

Chapter 2:

In Chapter 2, many of the experimental and theoretical approaches considered and adopted in this thesis will be summarized. These include the deposition system, sputtering targets, power supplies, substrate heater, and annealing equipment. (I designed and constructed the substrate heater myself because the deposition system was not equipped with one.) In addition, the film characterization techniques will be highlighted as will the essential details of the numerical simulation algorithms.

Chapter 3:

Chapter 3 presents a large fraction of the experimental results obtained in this thesis. The topics relate to the *materials* side of this investigation. Properties studied include film adhesion to silicon substrates, oxidation, microstructure, response to annealing, and thickness and refractive index uniformity across a wafer surface. Simulations of film thickness profiles and microstructure were also performed to correlate experiment with theory. The targets used were undoped fused quartz, 1 and 3% erbium-doped bulk glass, as well as undoped and erbium-doped compressed conductive powder. The powder targets were introduced as a potentially faster way

to deposit erbium-doped dielectric films. They were sputtered using conventional RF power as well as the newer bipolar pulsed DC technique.

Chapter 4:

A curious phenomenon was observed in the work reported in Chapter 3. The refractive indices of the films sputtered from erbium-doped bulk glass targets increased in value from the centre to edge of the film while the other films' index profiles tended to be flat or decrease in value. This radial refractive increase was counter-intuitive for a number of reasons that will be described. The purpose of Chapter 4 was to discuss my investigation into this behaviour and present the interesting conclusion that was drawn.

Chapter 5:

The final body chapter of this thesis contains all the results from the study of light absorption and spontaneous emission in the films. The techniques employed include spectraphotometry and direct optical pumping of films using a 980 nm laser.

Chapter 6:

This Chapter summarizes the conclusions of this thesis.

Chapter 2:

EXPERIMENTAL AND THEORETICAL CONSIDERATIONS:

2.1 Introduction:

Over the course of this project, a fairly broad array of experimental and diagnostic approaches were utilized. This chapter gives a detailed look at most of the experimental tools that were used and describes the essential experimental methodologies and developments. In addition, since some important thin-film simulations are included in the thesis, the relevant computational algorithms are briefly discussed.

2.2 Deposition System:

2.2.1 Vacuum Chamber and Magnetron Assembly:

The deposition system used for all sputtering runs in this thesis is represented in Figure 2.1. The system was designed for general purpose usage on a variety of projects at the Alberta Microelectronic Centre and incorporates multiple magnetron guns and a rotatable substrate stage that can hold up to 6 substrate trays at one time. The top magnetron was used for all runs in this thesis. It has an adjustable throw distance, and it houses a two inch water-cooled source. Unfortunately, the vacuum chamber's large volume, surface area, and baffled cryo-pump did not facilitate rapid pump down. With this system the lowest base pressure achieved was in the mid 10^{-6} Torr range. During deposition, flowing high purity Ar and O_2 gas raised the deposition pressure to between 5 to 15 mTorr.

There are several experimental parameters that can be varied in this system. Most obvious are the target-to-substrate throw distance and the working pressure in the chamber. Throw distance is varied by manually raising or lowering the magnetron gun. Working pressure is controlled by the argon and oxygen flow-rate settings on the gas inlets and by the throttle valve setting on the chamber outlet. The system was not equipped with a substrate heating mechanism, but one was fashioned for test purposes. This will be described in Section 2.2.5.

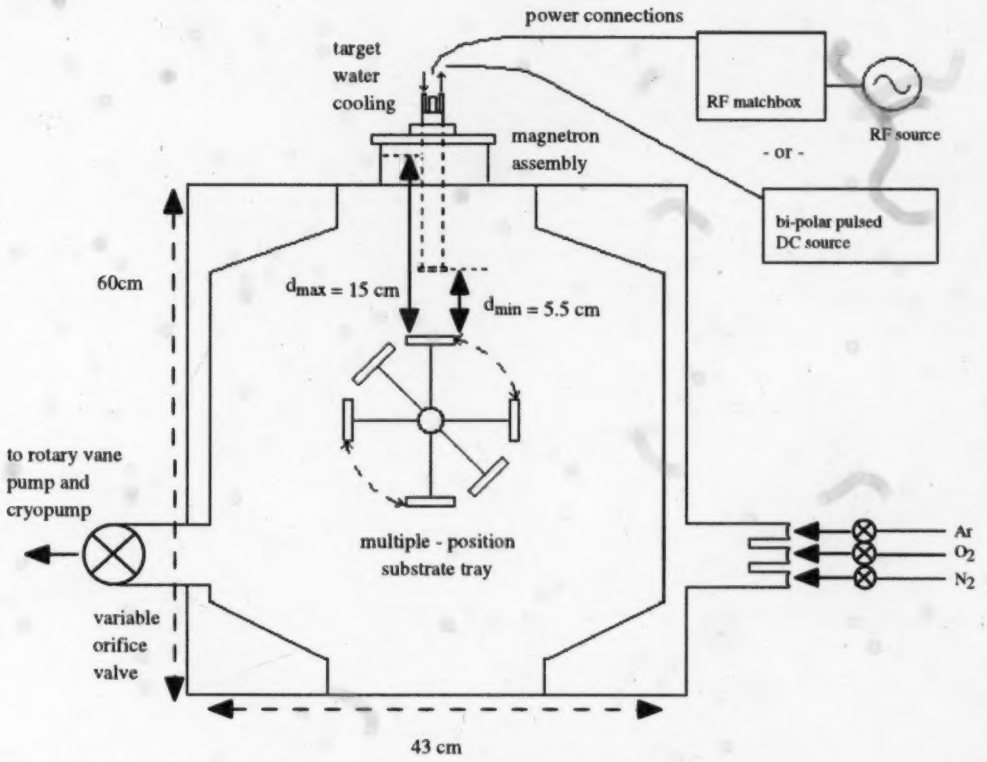

Figure 2.1 Multi-purpose vacuum sputtering system used for all sputter depositions.

2.2.2 Targets Used:

Fused Quartz:

Although this thesis is dedicated to erbium-doped sputtered glass films, for comparison purposes it is of scientific interest to look into un-doped dielectric films, as well. To this end, it seemed logical to start with fused quartz bulk glass targets. Sputtered quartz films served not only as a sort of control group for the erbium-doped glass experiments but as a reference for a series of numerical simulation studies. Using SIMSPUD - one of two programs that will be described in Section 2.3.4, the thickness uniformity profiles of all of the SiO_2 films were modeled. All films were sputtered in an oxygen-rich environment to promote proper oxidation of

the films. The other program, GROFILMS[52] was used to simulate the microstructure of one particular film.

Erbium-Doped Bulk Glass:

There were two erbium-doped bulk glass targets available for use. For comparison purposes they were called "Glass A" and "Glass B." The manufacturer will not be identified for sake of propriety, but both were doped with several metal-oxides. In fact, the compositions were veritable soups of oxides of Na, Si, K, Zn, Ba, La, Ce, and Er. Bulk Glass A was also co-doped with ytterbium.

The two dopants of primary interest in the samples were erbium and ytterbium. As described in Chapter 1, ytterbium is often added to erbium-doped glass to increase the width of the absorption band near 980 nm and thus increase pumping efficiency.[52] The quoted doping levels of Er and Yb in Glass A are 1% and 10-20%, respectively. Glass B has 3% Er and no Yb. The missing weight percentage was compensated for with increased lanthanum oxide levels.

The following table presents some quoted and measured refractive index values for bulk Glasses A and B. As with the fused quartz targets, these targets were also sputtered in an oxygen-rich environment to ensure formation of properly oxidized films.

		Glass A (1% Er,Yb co-doped)	Glass B (3% Er Glass)
Colour:		transparent light pink	darker shade of transparent pink
Density: (g/cm^3)		3.358	3.33
Refractive Indices:	wavelength (nm)	Index value	Index value
	587	N/A	1.609
	633	1.606	1.606**
	980	1.598	1.598
	1529	1.595	N/A
	1550	1.595*	1.594
		* *Extrapolated Data*	** *Interpolated Data*

Table 2.1 Some basic physical properties for the two erbium-doped glass targets (The colour variation was due to the variation in Er percentage.)

Compressed Conductive Powder:

Two compressed conductive powder sputter targets were also available. They were custom-designed coarse-grained disks composed of silicon, aluminum, and erbium on 2" copper backing plates. Aluminum was added as a potential preventative measure to help counter erbium clustering in the films. The first target was not doped with erbium. Rather, it consisted of 97% silicon and 3% aluminum. The second was made up of 97% silicon, 2% aluminum, and 1% erbium. Because there was no oxygen in the targets, themselves, it was absolutely essential for it to be present during reactive deposition. Otherwise the films would not sufficiently oxidize.

2.2.3 RF Power Supplies:

Two different RF power systems were used in this project. The first, an *Advanced Energy RFX-600* supply and model *ATN500* matchbox were used for sputtering the erbium-doped bulk glass targets. The reflected power with this equipment was quite high, and it was consequently replaced with *Plasma Products RF5S* series equipment. This system exhibited lower reflected power and was used for all the quartz and powder target RF sputtering runs. It was also used for all RF sputtering of films onto heated substrates.

2.2.4 Bipolar Pulsed DC Power Supply:

The power supply used in the asymmetric bipolar pulsed DC experiments was the ENI DCG-100. It provides full control over frequency and duty cycle of the pulsed signal. In this experiment, those values were kept constant. In order to coordinate my activities with other researchers' experiments, I used the same supply settings, namely a 195 kHz frequency with roughly 20% positive and 80% negative duty cycle. This seemed to provide acceptable, if not optimal, performance.

Figure 2.2 shows three experimental waveforms superimposed on each other. In these three waveforms the variable being manipulated is the relative oxygen content flowing in the chamber. It was observed that the higher the oxygen content the smaller the sputtering portion and the lower the rms voltage of the wave for a given power (100W).

It was also observed that the higher the oxygen content, the lower the deposition rate and the less stable the plasma. In fact, the plasma often extinguished itself at low pressure and high oxygen partial pressure. It is possible that this effect was a result of target poisoning. It was also probably exacerbated by the highly degraded condition of the confinement magnets in the magnetron source at the time of experimentation.

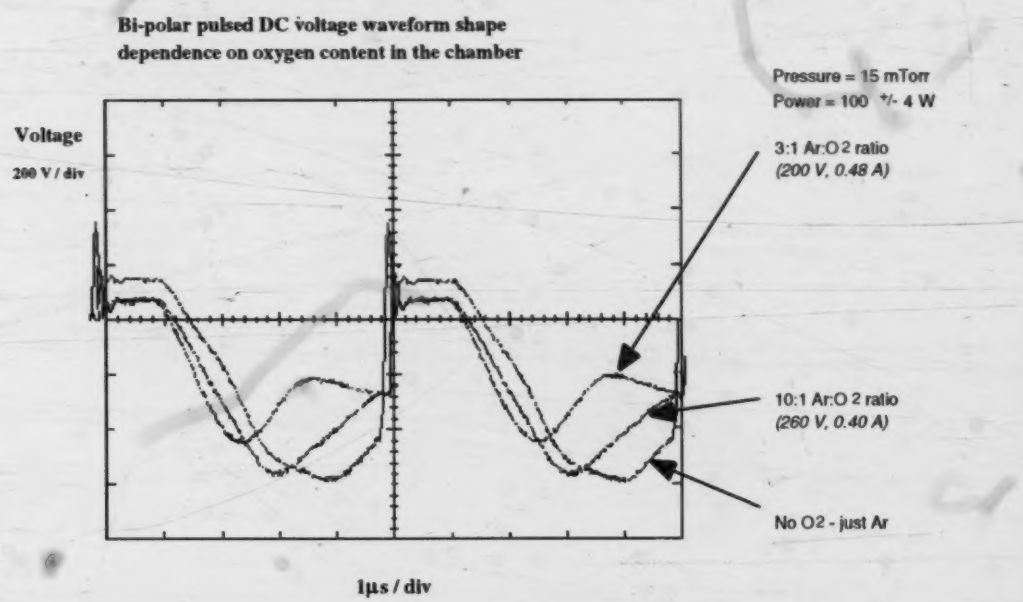
Bi-polar pulsed DC voltage waveform shape
dependence on oxygen content in the chamber
Pressure = 15 mTorr
Power = 100 +/- 4 W
Voltage
200 V / div
3:1 Ar:O 2 ratio
(200 V, 0.48 A)
10:1 Ar:O 2 ratio
(260 V, 0.40 A)
No O2 - just Ar
1µs / div

Figure 2.2 Actual bi-polar pulsed DC waveforms using the ENI DCG-100 power supply. As noted, traces correspond to different oxygen concentrations.

2.2.5 Substrate Heater And Film Annealing Equipment:

According to several sources, depositing erbium-doped glass films onto heated substrates and/or annealing them afterwards improves their spontaneous emission and decay lifetime characteristics as compared to untreated films.[22][43] It is possible that erbium ions assume the required Er^{3+} valence state more readily under these conditions. I thought it would be very useful to attempt some basic substrate heating and annealing experiments in this thesis to try to take advantage of any such effect. Unfortunately, the sputtering system was not equipped with a substrate-heating mechanism, so one was constructed.

(a) ***Substrate Heater:***

To this end, I designed and assembled a vacuum-compatible heater. I postulated that heating the films could enhance molecular diffusion to the point that it might reduce the columnar nature of the films. This might reduce energy losses from light scattering off column boundaries. In addition, reducing the number physical pathways that the erbium could segregate through might reduce the probability that erbium clusters would form.

The heater schematic is shown in Figure 2.3. It consists of a thoroughly cleaned resistive heating element on which an aluminum plate was bolted to disperse the heat. A retort stand was used to mount the entire mechanism, and the separation distance between the target and plate was 5.5 cm. Copper power cables were bolted to the heating element leads on the underside and a commercial thermocouple wires were butted in contact with the bottom of the aluminum plate. Unfortunately, the thermocouple cables could not stretch high enough to touch the top of the plate, where the substrate was situated.

All the cables were fed through to the outside of the chamber using a multi-purpose cable feed-through located on the bottom of the vacuum chamber. Adjoining cables on the outside of the feedthrough had already been soldered to a standard 2-prong electrical plug, so it was used. This plug was connected to a Variac variable transformer to drive the heating element. The thermocouple wires were soldered to a K-type connector which was connected to a FLUKE digital temperature gauge.

The Variac was calibrated over a range of transformer settings. In the end, only one temperature setting was used. The value chosen registered a temperature of roughly 280°C on the underside of the aluminum plate aluminum under vacuum. (Unfortunately, the thermocouple could not reach the top surface.) This setting was chosen because higher temperatures resulted in poor quality films from the bulk glass targets. The result was similar to the "surface bubbling" observed when these films were annealed too long at too high a temperature -see Section 3.6.1.

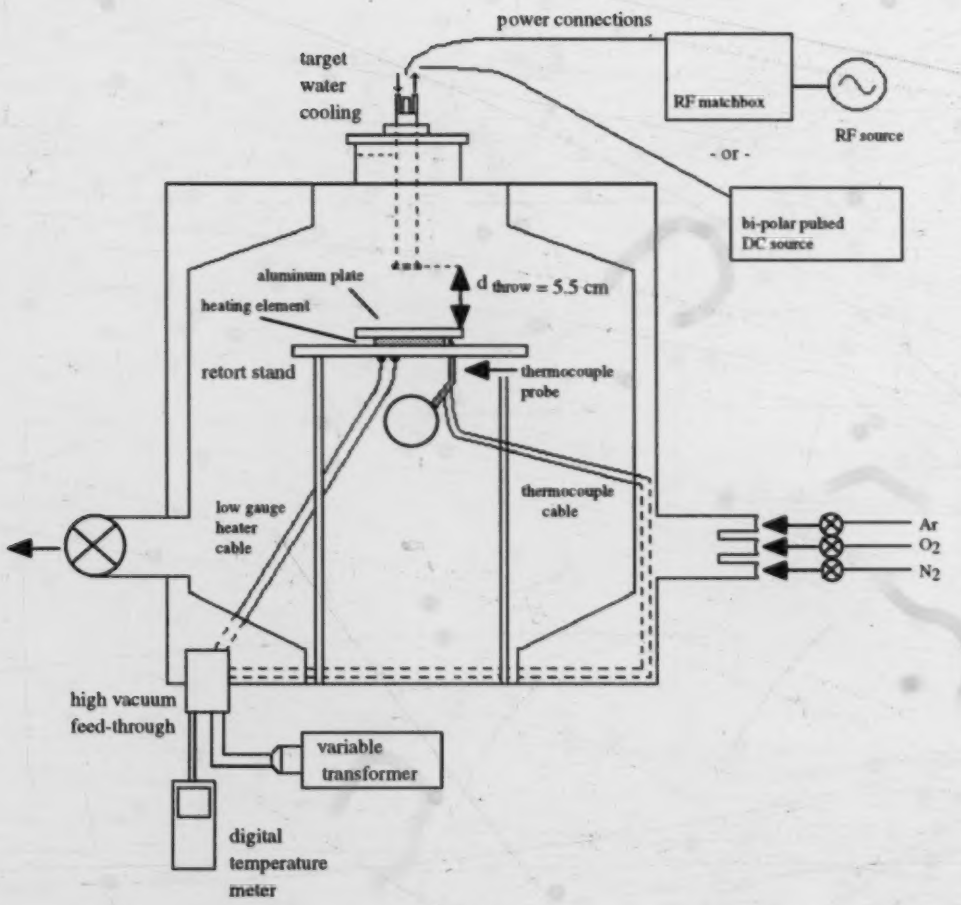

Figure 2.3: Schematic of heater assembly.

Observations:

After the heater was ramped up to temperature and the plasma was engaged, a considerable amount of arcing and sparking could be seen around the rim of the target-opening on the magnetron shield. The sparks caused the shield to become covered with jagged bumps. Fortunately, the effect was temporary, and the magnetron could easily be cleaned afterwards by sand-blasting and thorough rinsing.

The rate of shield-contamination was observed to subside after some period of time if the power was ramped up slowly enough. As a result, the power had to be ramped up in steps, with long pauses to let the sparking subside. Each pause could take up to 10 minutes depending on the power level.

Heated Substrate Deposition Procedure:

After some trial and error, a consistent heated-deposition strategy was adopted. Prior to this, the films had all been covered with spots. It was determined that these were voids and nodules resulting from ejecta that had splattered all over the surfaces. An example can be seen in planar view in Figure 2.4(a) and in cross section in Figure 2.4(b). The latter figure shows that the "spots" were classic nodule growths.[54]

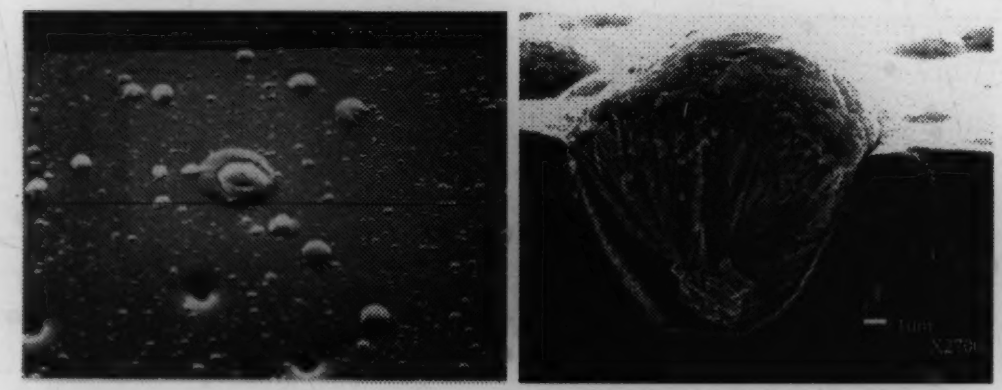

(a) **(b)**

Figure 2.4

(a) Plan view of quartz film covered with voids and ejecta of various sizes. (magnification is 1260 times)

(b) Cross section of nodule growth resulting from the ejecta landing on the surface during film deposition.

The heating procedure was as follows: The chamber was pumped down to a base pressure in the 10^{-6} torr range, and the heater was turned on to the pre-calibrated power setting. It was then allowed to warm up to temperature. At that point, the argon and oxygen gas supplies were turned on and adjusted to the desired flow ratio settings. The target power supply was then turned on and the plasma engaged. The power was slowly ramped up to its operating level, 5 to 10 Watts at a time.

The time interval between power steps was left long enough for most of the arcing to subside, typically about 5 to 10 minutes. Once maximum power was reached, the system was left alone for up to 30 minutes until the arcing visible to the naked eye stopped completely. At this point, the substrate cover was slid back and deposition was initiated. It was imperative that the substrate shutter remained over top of the silicon wafer at all times during ramping so that arcing debris would not contaminate the film.

After the deposition was completed, the shut-down procedure took place as follows: The shutter was closed, and the power supply was ramped down to zero. (This ramp-down was designed to minimize thermal shock to the target and had nothing to do with arcing effects.) The heater was then ramped down from operating voltage to zero over a one minute interval. After this, the chamber was vented to quench the films with nitrogen gas. Once the chamber door popped open, outside air would quench the film further. Once the heater assembly cooled somewhat, the wafer was removed, and the film colour and transparency were inspected. It was allowed to cool to room temperature on this plate before it was further handled.

Observation:

When the bipolar pulsed DC supply was used in combination with the heater, an interesting effect was observed. The pulsed sputter waveform oscillated up and down quite noticeably at the 60 Hz heater frequency. The envelope of this oscillation is shown in Figure 2.6. The trace looked very unstable and troublesome, but actually turned out to be *exceptionally stable*. It would not extinguish itself even at a 2-to-1 argon to oxygen ratio with pressure as low as 8.4 mTorr.

There was no way that such run conditions could have been used without the heater in place. The plasma would most certainly have extinguished itself. Such pronounced improvement in stability was curious and probably had to do with electrical interaction between the plasma and the current carrying wires of the heater. In principle, this effect could be utilized to help keep the plasma engaged at low pressures. However, I suspect that better magnets would probably produce the same result and not introduce as much contamination from arcing incidents.

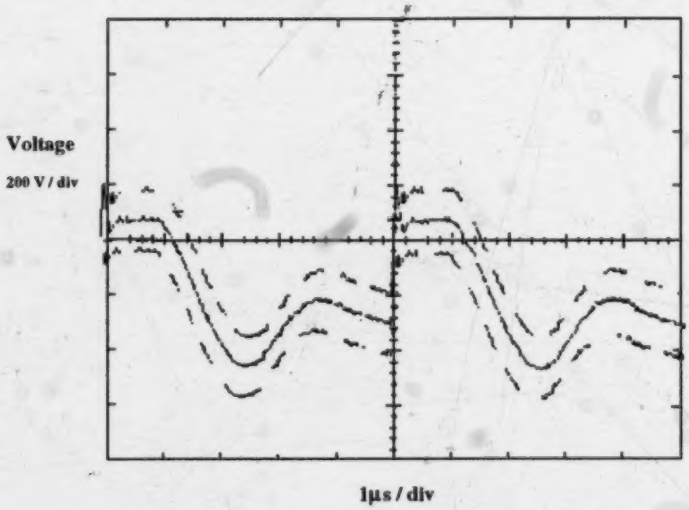

Figure 2.5 Oscillation envelope of the bipolar pulsed DC waveform once the heater is engaged.

(b) *Film Annealing Equipment:*

Two annealing methods were adopted in this thesis. In the first, samples were annealed in a *Thermco* tube furnace on top of a ceramic tray that sat on top of a glass boat. The second method was rapid thermal annealing (RTA). In this method samples were placed on a ceramic tray which gets lowered onto a hot plate surface. The RTA unit was made by *Micro Pyretics Heaters International*. Both methods will be described more in Section 3.6.

2.3 Film Characterization Methods:

2.3.1 Film Oxidation:

For the most part, visual inspection of the films was used to determine whether the films were fully oxidized. During deposition, clear glass cover slips were situated conveniently under

the sputter flux alongside of the substrate. If these films were clear then the films were deemed "oxidized" and glassy.

2.3.2 Film Quality:

The surface and cross-sectional film quality of the films were both investigated. Surface defects and etch uniformity were assessed by eye as well as a Cambridge Instruments Stereoscan 120 scanning electron microscope (SEM). Film microstructure required a higher resolution, so a JEOL JSM 6303 FXV scanning electron microscope was used. All of these high resolution photos were taken by George Braybrook in the Department of Earth and Atmospheric Science at the University of Alberta.

2.3.3 Film Chemistry:

One major goal of this thesis was to determine if the chemical composition of the films differed from that of the target. To this end, several quantitative element identification approaches were considered. For instance, X-ray Photoelectron Spectroscopy (X.P.S.) was considered, but the facility at Simon Fraser University was not equipped with automated quantitative analysis software, and since this is a surface technique, its results are extremely dependent on the cleanliness of the film surface.

Inductively-coupled plasma (ICP) was also considered. In this method, the film is dissolved in solution, and highly sensitive quantitative measurements are taken. With this technique, oxygen could not be accounted for and too much film was required to perform an accurate analysis so it was abandoned. I also considered using Rutherford backscattering (RBS) because it had been used by Schmulovich and others[51] to quantify the elemental composition of his erbium-doped films. Unfortunately, it was found to be cost and time-prohibitive and was also abandoned.

Eventually, two composition-measuring methods were attempted - energy dispersive X-ray analysis (EDX) and wavelength dispersive microprobe analysis. Both of these diagnostic systems were available on campus, so both were attempted. The first technique was quickly

abandoned, however, because it was found to be too inaccurate, with an uncertainty on the order of a few percent. The electron microprobe operates on a similar principle to EDX, but it is considerably more accurate, so it was used. The theory and practice of microprobe operation can be referenced in most good surface science texts[55],[56] and will only be briefly summarized here.

Microprobe Operation:

A collimated beam of electrons, commonly referred to as the "probe," is directed at a material sample. An excited volume of film emits characteristic secondary X-rays which can be analyzed to provide compositional information about the sample.[55] The depth of penetration depends on the energy of the beam. In my particular case, the beam energy was 15.0 kV, the beam diameter was 5 μm, and the depth was approximately 8 μm. As a result, a fairly thick film was needed.

Quantitative compositional analysis can be performed on the unknown sample provided that standards are available for all the film constituents. The standards are calibrated by illuminating them with a fixed-energy beam for a certain period of time. The number of counts given off inside each element's major spectral peaks are tabulated and stored by the computer. Once this is done, an unknown sample can be investigated.

A sample is probed at the same beam energy as the standards, and a broad spectrum is given off. The computer consults the standards' spectra and identifies the elements that produced the peaks. Based on the number and height of the characteristic peaks that each element gives off in the sample, its concentration can be determined. Sometimes there is a slight discrepancy between the standards and the elements depending on how they are bound inside the host. For instance, lanthanum, erbium, and cerium standards used phosphate as the anion rather than oxygen. Corresponding oxide standards were unfortunately not available. As a result, there will be a slight error in determining the absolute concentration values of the elements. Nonetheless, the JEOL 8900 microprobe used in this project was known to be very self consistent, so comparing relative concentrations changes among different film samples should be valid.

2.3.4 Film Thickness and Refractive Index:

Film thickness uniformity, deposition rate, and refractive index uniformity are important properties from a fabrication perspective. Variation in feature size and sharpness will occur from inconsistencies in mask-film separation. In addition, waveguides whose thickness and refractive index vary significantly over a couple of centimeters are also subject to unpredictable effects including high propagation loss. Refer to Figure 1.10 (e).

Film uniformity can be achieved if the target to substrate throw distance is made large enough to allow sputter flux to disperse uniformly over the wafer's surface by the time it is reached. The drawback to this approach is that considerable material is lost outside the deposition zone, so deposition rate drops considerably. Low deposition rates slow down film production, increase cost, and increase the likelihood that unwanted molecular debris will accumulate on the film surface over time. Thus, there is a trade-off between deposition rates and film uniformity.

A production deposition system would, of course, demand utmost film uniformity and quality. This thesis research work does not necessarily have as strict standards because many of the optical properties of interest can be investigated with non-uniform films. Nonetheless, if the research is intended to influence future film production, issues like uniformity, quality, and refractive index are still very important.[7]

There are several techniques available to measure film thickness - for instance, interferometry, profilometry, ellipsometry, reflectance spectroscopy, and prism coupling.[28] All of these techniques were available and each was attempted to some degree over the course of my research. In the end, prism coupling was adopted as the method of choice for most films. It is regarded as the most accurate method available for determining film thickness and refractive index of thin non-absorbing films.[57]

A Nanospec Interferometer was also used to measure very thin films approximately 100 to 300 nm thick and an Alpha-Step Profilometer was used to measure etch depth during film etching. The profilometer was also used as a calibration cross check to test the prism coupler.

Ellipsometry was attempted for thicker films but was abandoned because very inconsistent results were obtained with the instrument I had at my disposal. It was more accurate for thin films. Reflectance spectroscopy was also looked into but was never needed because a Metricon Model 2010 prism coupler was available. The prism coupler is accepted as a highly accurate tool for measuring film thickness and refractive index for dielectric films. Its operating principles are discussed in detail in Appendix A.

2.3.5 Optical Absorption and Spontaneous Emission:

(The relevant experimental tools used for this investigation will be discussed in Chapter 5. The main diagnostic approaches used were spectraphotometry and an optical fibre test bench.)

2.4 Thin Film Simulation Tools - *SIMSPUD*™ and *GROFILMS*:

As stated in Chapter 1, it was my goal to incorporate computer simulations into this thesis in order to correlate the theory and practice of glass film deposition. First, I wanted to attempt to simulate the film uniformity profiles for some sputtered quartz experiments. The intention of this was to see if the deposition profiles measured with the prism coupler agreed with theory. Also, I wanted to see if SIMSPUD could accurately simulate films sputtered from a multiple-oxide bulk glass target. The relative concentrations of the elements were provided by stoichiometric analysis using a wavelength dispersive microprobe. Also, I wanted to make use of the recently-developed film growth simulator, GROFILMS, to try to mimic glass microstructure. The purpose of this section is to describe these simulation tools and how I plan to incorporate them.

2.4.1 SIMSPUD™ *(SIMulation of SPUtter Distributions)*:

SIMSPUD, "SIMulation of SPUtter Distribution," is the vapour transport component of the film deposition simulator program, SIMBAD, "SIMulation of Ballistic Deposition." These programs were jointly developed at the University of Alberta, Carleton University, and the Alberta Microelectronic Centre. They use a three-dimensional Monte Carlo algorithm to

generate angular and energy distribution files which SIMBAD uses to predict film growth and microstructure over IC topography. For the purpose of these simulations, it is important that SIMSPUD can also "directly predict uniformity profiles and relative deposition rates" of sputtered materials.[34] The higher the pressure and the farther the chamber throw distance, the more the flux gets scattered by the background gas. As such, the pressure and target-substrate separation in the simulation volume are very important parameters and strongly affect how the flux propagates. The bombarding energy of the argon ions at the target is inferred from the DC cathode voltage.

The SIMSPUD computational algorithm can be described as follows: Sputtered atoms are ejected in straight lines from the target and proceed until they collide with background gas and change their trajectory. SIMSPUD generates the spatial, angular, and energy distributions of ejected flux from a single species target and then computes particle evolution from target to substrate.[34] Some essential experimental parameters such as bulk material binding energy, magnetron throw length, chamber working pressure, and target erosion profile are set to match experimental run conditions.

By default, SIMSPUD uses a *cosine* emission angle distribution for the incident sputter flux. This is the commonly accepted methodology in sputtering simulations, but because targets can have various grain structures and material compositions and because various experimental conditions can influence the flux distribution, this function is not exact.[27][34] Therefore, in order to improve correlation with observed film properties it can be arbitrarily changed by the user. In the simulations in this thesis, both cosine and cosine^8 distributions were used in simulations. The two emission profiles can be seen in Figure 2.6. Cosine^8 was chosen somewhat arbitrarily because it is a sharper emission distribution. It was used as an attempt to improve correlation with the experiments.

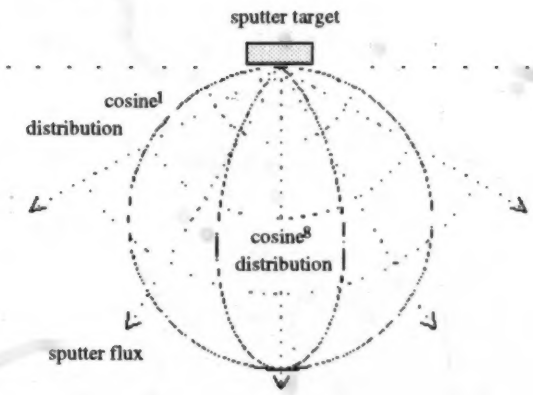

Figure 2.6 Emission profiles that were used in the simulations.

The program can also take into account the *annular-shaped* erosion profile of a magnetron target caused by magnetic confinement of the plasma. This profile is often referred to as the "race track."[28] The user simply enters a surface erosion profile description file, and the program incorporates this when generating ejected flux.[34] The following figure shows the plot of an empirically determined radial target erosion profile. The data points were obtained with a profiling tool used on an eroded target surface from this magnetron source.

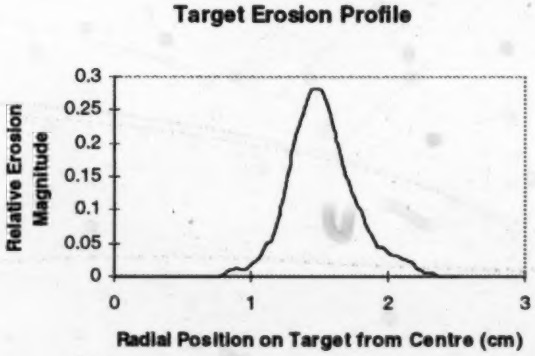

Target erosion profile that was used in all simulations.

Figure 2.7

Collisions between the sputtered atoms and background gas are assumed to be elastic, and collisions with other sputtered atoms or energetic neutrals are neglected.[34] The free path of the

sputtered atoms is randomly determined from a Poisson distribution about λ_m, the mean free path of a sputtered particle.

$$F_\lambda(\lambda)d\lambda = {}^{d\lambda}/_{\lambda_m} e^{-\lambda/\lambda_m} \qquad (2.1)$$

The mean free path is the average distance the atoms travel in a sputter flux before they collide with an argon ion. It is described by the formula,

$$\lambda_m = {}^{kT}/_{P\sigma}, \qquad (2.2)$$

which depends on thermal energy, pressure, and collisional cross-section, σ.

Collisional cross section, σ, is an energy dependent parameter. When $E>E_o$(=1 eV) sigma is defined as

$$\sigma(E) = \sigma(Eo)(E/Eo)^{-0.29} \qquad (2.3)$$

Below this energy, it is assumed that the particle is completely thermalized and sigma becomes:

$$\sigma_t = \pi (1 + m/m_g)^{0.5}(r_{st} + r_{gt})^2 \qquad (2.4)\ [34]$$

Both $\sigma(Eo)$ and σ_t have been measured at the Alberta Microelectronic Centre for elements Al, Ti, Cu, Mo, and W, but, unfortunately other data was not available. As a result, it had to be judiciously approximated. I was actually able to draw a correlation between measured collisional cross sections and atomic mass, so interpolations and extrapolation could be done for the other elements. The approximations are discussed in Appendix B, and they actually may turn out to be of some significance to SIMBAD customers around the world.

2.4.2 GROFILMS *(GRain Oriented FILm Microstructure Simulator)*:

GROFILMS is a two dimensional thin film simulator developed at the University of Alberta to model the fundamental properties of thin film growth.[52] It uses a unique calculation algorithm that employs a line-segment / nodal description of film surfaces in order to calculate properties like surface curvature, interfacial energies, crystal surface orientation, and film microstructure.[52] It was my intention to give this software a new challenge - to simulate the microstructure of sputtered glass.

GROFILMS simulates ballistic impingement and growth of sputtered material by randomly selecting particles based on the angular distribution of the incident vapour flux. SIMSPUD can be used to generate this information or else a cosine default can be chosen. Film growth is initiated when impinging vapour particles start to nucleate. These particles either reflect off the surface or adsorb and diffuse until they coalesce with other adsorbed atoms.

Surface diffusion and grain boundary migration effects are modeled using Gibbs free energy considerations from thermodynamics. That is, in any equilibrium thermodynamic process at constant temperature, the mathematical quantity called "Gibbs free energy," G = E - TS, is always minimized.[58] (E = energy and S = entropy.) For convenience, GROFILMS minimizes the *rate of change* in free energy. The results dictate where a diffusing particle with a given diffusion length will come to rest. Mathematical computation of interface energies, localized potentials, and nodal movement is performed at different "nodes" defining the surface of a growing film. Line segments connect nodes together and represent grain outlines. As the film surface and microstructure evolve, nodes are added to or deleted from the simulation dynamically. In this thesis, an equilibrium model is used; although a kinetic model is also available to calculate time-dependent effects such as copper re-flow.[52]

2.4.3 Numerical Simulation Objectives:

My objective with SIMSPUD was to use it to simulate the thickness profiles of RF sputtered oxide films. I began by simulating quartz, *a simple compound*, and then progressed to more complicated multiple-oxide glass. Simulating such a complicated non-metallic material - is not the intended usage of the program, so some approximations and limitations were recognized.

One important approximation arises from binding energy considerations within a multiple-component material. The binding energy of a single element is "the energy required to separate neutral atoms in their ground state from the solid at 0 K at 1 atm."[58] In a SIMSPUD simulation, binding energy is represented by one single value. In a multiple-component species atomic bond strengths of material in the glass will undoubtedly be complicated by dissimilar neighboring atoms within the material matrix. This makes it difficult to feed SIMSPUD a single representative binding energy value for a multiple species simulation. This technique assumed

that individual components would not be affected by their neighbors which is not true, but I could not predict the extent of the variation, so I assumed that the influence would be negligible. In addition, collisions with background oxygen were neglected. It was hoped they would not change scattering dynamics significantly.

My methodology for simulating a multiple component material was to run simulations for each element and combine the results in an average that is weighted according to the percentage and volume of each oxide in the bulk glass sample. To do this, each individual element was simulated in isolation, using its own binding energy value. Then, individual deposited particles were sized by assuming that each one had the volume of the most common oxide molecule. These "volumetrically-sized" thickness distributions were assembled in accordance with the deposition efficiency and percent fraction of each element in the target.

My objective with GROFILMS was to generate a glass microstructure simulation based on experimental observations. Glass microstructure is not typically observed or simulated, so this would be a novel experiment, as well.

2.5 Fabricating Raised-Ridge Waveguides:

As discussed earlier, raised-ridge waveguides were patterned in order to provide lateral confinement during optical characterizations. The following paragraphs lists the complete fabrication steps used to deposit and pattern a film. The photolithography process was finalized after some trial and error, but the basic chemicals and times were adapted from standard AMC photolithography procedure. The goal was to produce raised-ridge waveguides etched as evenly as possible with a minimum number of defects.

Complete Fabrication Sequence:

Figure 2.8 shows the complete fabrication sequence. First, packaged wafers were removed from the plastic containers and cleaned in a hot piranha etch for one hour. (Dipping substrates in a *piranha* bath is a highly effective technique to remove organic material from wafers; the mixture is made up of 2/3 sulfuric acid and 1/3 hydrogen peroxide.[30]) Then the wafers were coated with 5 μm of CVD silicon dioxide which served as an adhesion layer and a cladding layer

for the waveguides. The films were then placed into the sputtering system, deposition conditions were set, and an erbium-doped film was sputtered on top. The film was visually inspected, and its thickness and refractive index profiles were measured using the prism coupler.

The photolithography process was initiated by heating the wafer section to be patterned under vacuum for two minutes at 120°C. This allowed any adsorbed water vapour to evaporate off. This was necessary to allow the photoresist to adhere properly and was performed in lieu of an HMDS vapour-priming step. After the wafer was heated, it was quickly cooled under a nitrogen gas gun and placed on the photoresist spinning chuck. Olin Hunt HPR 504 photoresist was then applied evenly to the wafer surface and then spun on. The spinning cycle was a 500 rpm spread for five seconds followed by a 30 second spin at 3500 rpm. After this, the wafer was soft baked for 50 seconds at 110° and placed into the mask aligner.

There were two positive masks available at AMC with waveguide features on them. One had 3 bands of 5, 7, and 9 μm strips. The other had waveguides ranging from 5 to 100 μm. Both were used in these experiments depending on the size and shape of the wafer chunk being patterned. For instance, it was often inconvenient to use Mask 1 because the waveguide features were over to one side of the mask, and smaller wafer sections could not be lined up properly underneath. As a result, Mask 2 had be used. In order to promote as much consistency between the runs as possible, only the narrow guides were used for spontaneous emission testing when Mask 2 was used.

Each wafer section was lined up under the waveguide features on the mask and exposed for 4.5 seconds. Originally, a shorter time of 1.5 seconds was attempted, but the photoresist did not expose fully. The patterned wafer was then developed in Shipley 354 developer for 20 to 24 seconds and inspected under a microscope. Assuming the process was successful, the wafer was then hard-baked for one minute at 120°C on a heated vacuum chuck. After this, the wafer was moved to an enclosed oven and baked for another 30 minutes at 120 °C.

The final stage of the fabrication process was etching. The goal - provided there was enough film - was to produce roughly 2 μm deep waveguides by wet-etching in 10:1 BOE. An alpha-step profilometer was used to measure the initial step height, and then the wafer was BOE dipped

for one minute. After this time, it was washed thoroughly in de-ionized water and re-profiled. The difference in step height gave a rough indication of the etch rate. It was a "rough" indication because the etch rates were inconsistent from minute to minute. They seemed to vary between 140 to 370 nm per minute for any given film.

All the films to be studied were of different thicknesses, so there was an inevitable variation in ridge height from waveguide to waveguide being studied. Although this variation introduced some inconsistency into the experimentation process, I did not consider this a major problem because the intended purpose was not to produce perfect waveguides. Rather, it was to improve light confinement in the films in order to facilitate observation of spontaneous emission.

After the waveguides were patterned and rinsed, the photoresist was removed with acetone. After being rinsed again, they were cleaned in a hot piranha bath for approximately one hour to clean the surface. Figure 2.9 gives an example of some waveguides patterned using Mask 2.

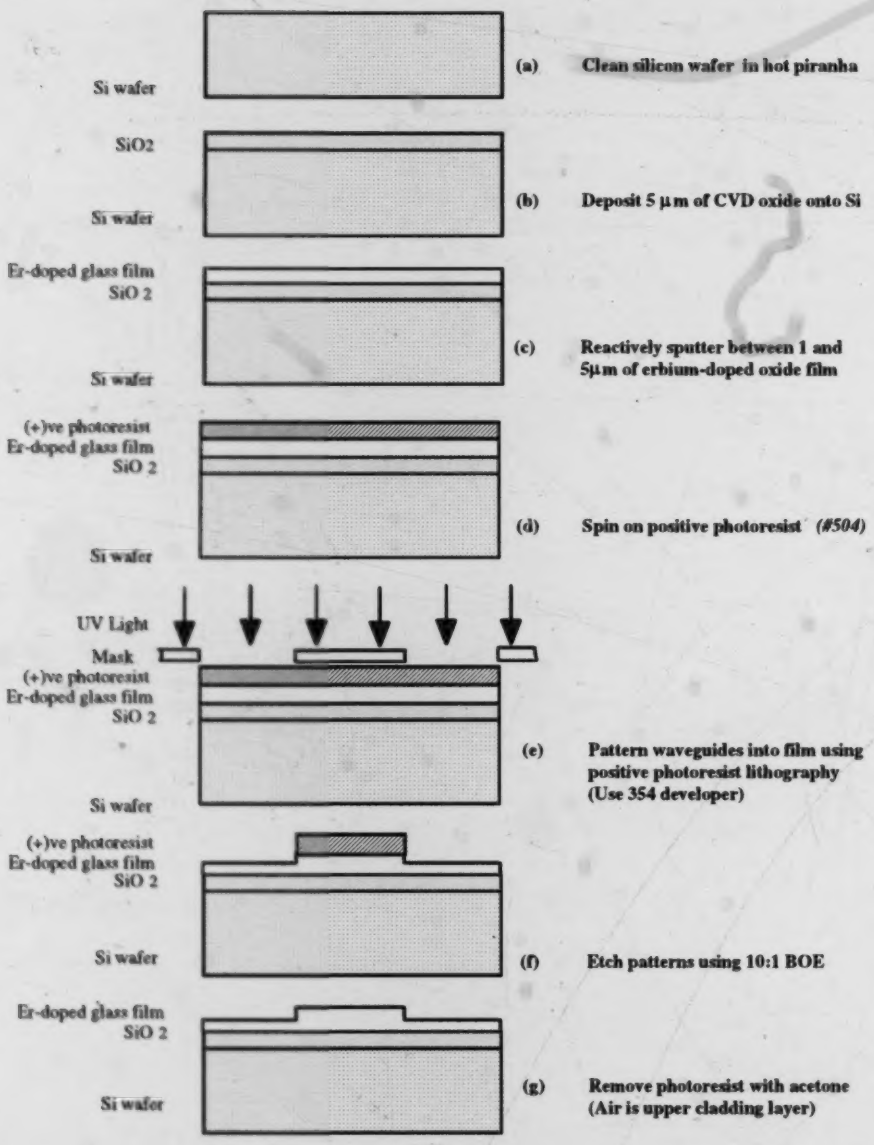

Figure 2.8: Waveguide fabrication sequence.

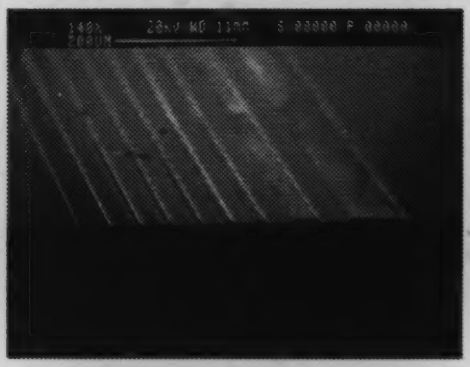

Raised ridge waveguides patterned using Mask 2.

Figure 2.9

The desired individual waveguides resemble those shown in the Figure 2.10. The fundamental modes were simulated using F-Wave[60] for two of the films that will be introduced shortly in Chapter 3. Notice that the higher the index difference between the film and the oxide cladding layer, the tighter the modal confinement. (This figure is included here for completion and comparison purposes only. I do not dwell on the electromagnetic wave propagation as this is beyond the scope of this investigation.)

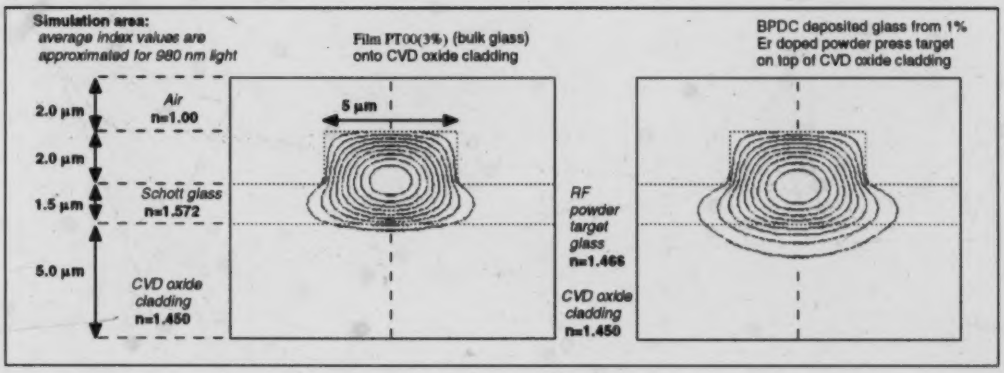

Figure 2.10: Simulated modal shaped in ridge waveguides.

Chapter 3:

EXPERIMENTAL RESULTS:

Material Properties of Sputtered Glass Films

3.1 Introduction:

This chapter presents a large fraction of the experimental results obtained in this project. The focus was on determining some basic material properties of sputtered glass films and how they are affected by deposition conditions. The main experimental parameters that were varied were sputtering pressure, magnetron target-to-substrate throw length, target material, power supply, and deposition method. The active optical properties, absorption and spontaneous emission, will be discussed in Chapter 5.

The fabrication issues addressed are film adhesion to and oxidation on silicon substrates, thickness uniformity, extent of glass microstructure, response to annealing, and refractive index uniformity across a wafer surface. The motivation was to gain a better understanding of the major issues involved in sputtering the chosen material with the techniques available.

An assortment of targets was used - fused quartz, 1% and 3% erbium-doped bulk glass, and undoped and erbium-doped alumino-silicate compressed conductive powders. Since glass targets are non-conductive, they were sputtered strictly with an RF power source. The powder targets, on the other hand, were conductive and were reactively sputtered using both RF and bipolar pulsed DC supplies.

3.2 Deposition Conditions:

The purpose of this section is to discuss the deposition conditions that were used to produce all of the major films characterized in this thesis. Apart from the type of target and the method of sputtering used, the two quintessential deposition variables to be manipulated throughout this thesis are the working pressure in the chamber and the target-to-substrate throw distance. In order to study as broad a range of deposition conditions as possible, these values were set to reasonable extremes of high and low values achievable within the limitations of the deposition system.

The deposition conditions are shown below in Table 3.1 and are enumerated by the pseudo-binary notation, PT##. For example, PT00 refers to a pressure of 3.3 mTorr and a throw of 5.5 cm, and PT11 refers to a pressure of 10.8 mTorr and a throw of 15.0 cm. The other cases are derivatives of these values which were adopted for convenient representation of the conditions. At first, only integer indices were used, but as the experiment evolved and slightly different pressure / throw combinations were incorporated, fractional enumeration had to be used, as well. The type of target and sputtering method are included in parentheses after the name index.

Pressure / Throw Lengths and Chamber Gas Ratios:

Film Name	Deposition Method	Target Used	Pressure / Throw Combination	Pressure (+/- 0.2 mTorr)	Throw Length (+/- 0.25 cm)	PT_Product (mTorr cm)	Reactive Gas Ratios Ar:O2	(sccms)
PT00 (QZ)	RF	Fused	low / short	3.1	5.5	17.1	3:1	18.0 : 5.6
PT01 (QZ)	RF	Quartz	low / long	3.1	15.0	46.5	3:1	17.5 : 5.8
PT10 (QZ)	RF		high / short	10.8	5.5	59.4	3:1	27.9 : 9.3
PT11 (QZ)	RF		high / long	10.8	15.0	162	3:1	27.9 : 9.4
						base pressure = 2.0×10^{-5} mTorr		
PT00 (1%)	RF	1% Er-	low / short	3.1	5.5	17.1	3:1	15.5 : 5.1
PT01 (1%)	RF	Doped	low / long	3.1	15.0	46.5	3:1	15.1 : 5.0
PT10 (1%)	RF	Glass	high / short	10.8	5.5	59.4	3:1	15.3 : 5.0
PT11 (1%)	RF		high / long	10.8	15.0	162	3:1	15.4 : 5.1
						base pressure = 5.0×10^{-6} mTorr		
PT00 (3%)	RF	3% Er-	low / short	3.1	5.5	17.1	3:1	17.5 : 5.6
PT00 (3%)_thick	RF	Doped	low / short	3.1	5.5	17.1	3:1	17.4 : 5.6
PT01 (3%)	RF	Glass	low / long	3.1	15.0	46.5	3:1	18.9 : 6.1
PT10 (3%)	RF		high / short	10.8	5.5	59.4	3:1	25.0 : 8.0
PT11 (3%)	RF		high / long	10.8	15.0	162	3:1	25.0 : 8.0
						base pressure = 6.5×10^{-6} mTorr		
PT10 (AlSi_RF)	RF	Un-doped	high / short	15.0	5.5	82.5	3:1	45.0 : 15.0
PT10 (AlSi_bDC)	bi-Polar DC	Alumino-	high / short	15.0	5.5	82.5	3:1	45.7 : 15.2
		Silicate Conductive Powder Press				base pressure = 4.5×10^{-6} mTorr		
PT10 (ErAlSi_RF)	RF	Er-doped	high / short	15.0	5.5	82.5	4:1	46.5 : 11.7
PT1,1/3 (ErAlSi_RF)	RF	Alumino-	high / mid	15.0	8.5	127.5	4:1	47.9 : 12.1
PT10 (ErAlSi_bDC)	bi-Polar DC	Silicate	high / short	15.0	5.5	82.5	4:1	50.7 : 12.5
PT1,1/3 (ErAlSi_bDC)	bi-Polar DC	Conductive	high / mid	15.0	8.5	127.5	4:1	47.6 : 11.9
		Powder Press				base pressure = 4.5×10^{-6} mTorr		

Table 3.1 Labeling scheme used to identify the major films deposited in this thesis and the major run parameters associated with them.

Pressure was measured with a capacitance manometer, and the meter fluctuation was observed to be approximately +/- 0.2 mTorr. The throw length measurements were performed with a hand held ruler and the uncertainty was determined to be +/- 0.25 cm from the vantage point at which they had to be taken.

It was not intended that the gas flow ratio be a manipulated variable in these experiments. Rather, it was intended that enough oxygen be present to ensure that films were fully oxidized. In a paper by Schmulovich *et al* on the subject of erbium-doped thin film waveguides, he described how his group at Lucent successfully obtained spontaneous emission with measurable decay lifetimes using a 3:1 Ar to O_2 ratio.[51] Owing to this reported success and that "glassy-looking" films were made under these conditions, this ratio was adopted here wherever possible, as well.

The argon to oxygen ratios in the chamber were controlled by the mass flow controller knob settings (refer to Figure 2.1). Gas flow settings varied among runs at the same pressure because the manual positioning on the chamber throttle valve was usually in a different setting each time, and its positioning was difficult to reproduce consistently.

The lowest base pressure value the system could attain after 8 or 9 hours of cryo-pumping was usually somewhere in the mid 10^{-6} Torr range - this is the *high vacuum* regime. During the quartz depositions, the system was experiencing some problems with pump-down, and the lowest pressure that could be obtained was $2x10^{-5}$ Torr. This value was higher than desired, but film purity was not of utmost priority for these *control group* films.

The fifth column in Table 3.1 shows the "pressure_distance product." This figure of merit is a way of quantifying the extent to which sputter flux collides with background gas and scatters. From gas scattering considerations, the number of collisions that sputter flux encounters is proportional to this product.[34]

It was decided that long-throw runs would not be performed on the erbium-doped material. Instead, short and medium-range throws of 5.5 and 8.5 cm were used for the erbium-doped powder target. The medium-throw runs were denoted PT1,1/3(ErAlSi_RF) and PT1,1/3(ErAlSi_bDC).

Voltage and Power Levels:

In Tables 3.2 and 3.3 some other key experimental parameters are shown including film name, deposition method, power and voltage levels, deposition times, and nominal deposition rates averaged from the centre out to 2 cm from the centre. Table 3.2 has all the data for the RF runs; whereas Table 3.3 has the data for the films sputtered using bipolar pulsed DC.

Film Name	Deposition Method	Target Used	Pin (Watts)	Preflected (Watts)	Bias Voltage Developed (V)	Deposition Time (hrs:min)	Dep. Rate Ave. Over 2 cm (Angstroms/min)
PT00 (QZ)	RF	Fused	100	3	289	04:40	79
PT01 (QZ)	RF	Quartz	150	2	390	24:00	16
PT10 (QZ)	RF		100	0	379	05:20	71
PT11 (QZ)	RF		150	0	250	24:00	10
PT00 (1%)	RF	1% Er-	50	14	172	23:00	35
PT01 (1%)	RF	Doped	50	15	170	23:00	6
PT10 (1%)	RF	Glass	50	11	191	23:00	27
PT11 (1%)	RF		50	11	188	23:00	3
PT00 (3%)	RF	3% Er-	50	9	185	25:30	55
PT00 (3%)_thk	RF	Doped	50	9	185	52:00	
PT01 (3%)	RF	Glass	50	10	183	25:30	12
PT10 (3%)	RF		50	10	160	25:30	48
PT11 (3%)	RF		50	10	187	25:30	5
PT10 (AlSi_RF)	RF	Un-doped Conductive	100	1	220	02:00	139
PT10 (ErAlSi_RF)	RF	Er-doped	100	1	194	05:17	142
PT1,1/3 (ErAlSi_RF)	RF	Conductive	100	1	194	07:10	79

Table 3.2 Several measured parameters for the RF sputtered films.

Film Name	Deposition Method	Target Used	Power (Watts)	Current (Amps)	Voltage (V)	Deposition Time (hrs:min)	Dep. Rate Ave. Over 2 cm (Angstroms/min)
PT10 (AlSi_bDC)	bi-Polar DC	Un-doped Conductive	100	not taken	not taken	02:00	205
PT10 (ErAlSi_bDC)	bi-Polar DC	Er-doped	100	0.47	214	04:00	169
PT1,1/3 (ErAlSi_bDC)	bi-Polar DC	Conductive	100	0.48	208	05:30	113

Table 3.3 Several measured parameters for the bipolar pulsed DC sputtered films.

Quartz Targets:

Since glass has a low thermal conductivity,[56] sharp thermal gradients can develop across a 3 mm thick target slab from the sputtered surface to the side being water-cooled. As a result, it can heat up dramatically until it cracks. Because quartz targets were fairly robust and inexpensive, they could be run at 100 and 150 Watts with little concern for cracking. Films were sputtered with the *Plasma Products* power supply and matchbox at these two powers for

different times - the goal being to generate films with similar thickness. Although it would have been more consistent to run at one power level only, these films were mainly intended for general comparative purposes, so power inconsistency should not be a major issue.

Doped Bulk Glass and Powder Targets:

The 1% and 3% erbium-doped glass targets were much less robust than fused quartz, so the magnetron power had to be kept to 50 W. This is one of the major problems with sputtering from bulk glass targets. To compensate for the extremely low deposition rates encountered at this power, all the films were sputtered for extended periods. The 1% Er-doped films were sputtered for 23 hours while the 3% films were run for 25.5 hours. One extended run was also performed for 52 hours in order to make an extremely thick film for a microprobe analysis. Both sets of runs were done with the *Advanced Energy* power supply and matchbox. The compressed powder metal targets were sputtered using both RF and bipolar pulsed DC. They were reasonably robust and could be sputtered at 100 Watts without being damaged.

3.3 Forming Glass Films on Silicon Substrates:

3.3.1 Film Adhesion Problems:

It was intended in this investigation that all the films be deposited onto silicon wafers. The first step of the process was to pre-clean the wafers for approximately one hour in "piranha" solution prior to deposition to remove contamination. The films sputtered from the powder targets all adhered well to the silicon surfaces, but none of the films produced from the quartz or erbium-doped bulk glass adhered particularly well. In fact, their film surfaces were for the most part very noticeably rippled, almost resembling a crinkled metal foil to the naked eye. In the SEM image in Figure 3.1(a), the 1% Er-doped film can actually be seen to be "flaking" off from the wafer.

It is possible that excessive film stresses could have developed during deposition and that the films actually lifted off as some sort of stress relief mechanism. It is also possible that the flux never bonded properly at all. The first theory seemed plausible and was investigated to a superficial degree using an in-house Ionic Systems Stress Gauge. It could not be pursued to any

real depth, however, because the gauge was found to give unreliable data, and its numbers had to be discarded.

Glass film adhesion had not been such an insidious problem in past sputtering work at the AMC. In the past, though, a 5 μm CVD oxide layer had always been pre-deposited onto the wafers prior to sputtering. The function of the film was as an optical cladding layer for waveguide applications. It was postulated that this under-layer may have provided a more compatible chemical state for impinging flux bonding than just a plain silicon wafer, thereby enabling it to adhere better. It was further postulated that perhaps the coefficients of thermal expansion would be more closely matched between the sputtered glass and silicon dioxide than with silicon. The latter theory was briefly investigated and was found to be unsupported.

The linear coefficients of thermal expansion for the *films* are not known exactly, but the bulk glass and silicon wafer coefficients are as follows:

SiO_2	$5x10^{-7}/^{\circ}K$ [56]
1% erbium-doped glass	$9.7x10^{-6}/^{\circ}K$ [*proprietary*]
silicon	$2.4x10^{-6}/^{\circ}K$ [61]

This data suggests that silicon is actually a better thermal match for doped glass than SiO_2. This would seem to contradict the thermal compatibility theory. In actuality, though, the theory still may be valid because bulk data may not be completely relevant.

Whether any of these hypotheses are accurate or not, CVD oxide coatings were found to be quite an effective adhesion mechanism for either sputtered quartz or doped glass. This is demonstrated in Figure 3.1(b), where a typical film surface is shown. Clearly, the look of this film surface is a stark contrast to that of the rippled film in Figure 3.1(a) which did not adhere. As a result, all films were deposited on top of CVD oxide. For the films for spontaneous emission testing, 5 μm of CVD oxide was deposited. This acted as both an adhesion layer and optical cladding.

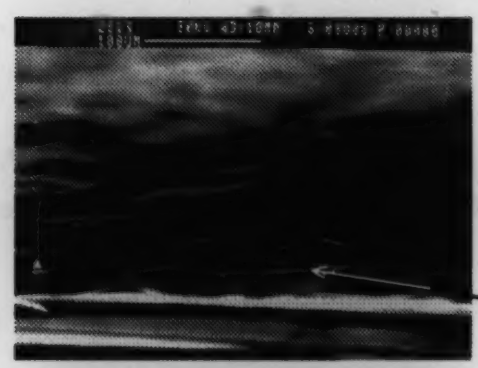

A typical SEM micrograph from the first group of films sputtered directly onto silicon wafers It is evident that the films suffered from very poor adhesion to the wafer surface.

Magnification is 281 times.

(surface ripples)

(a)

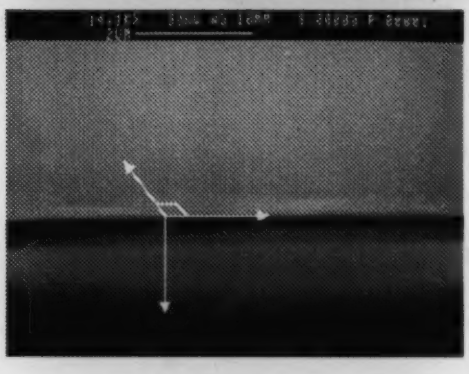

This is a typical SEM micrograph from the second group of sputtered films. In this case, a CVD oxide layer was deposited onto the blank silicon wafer first.

The magnification is 14,100 times

(b)

Figure 3.1 SEM photographs of (a) poorly adhering film and (b) properly adhering film.

Summary:

In general, sputtered glass films did not adhere well to blank silicon wafers, so a CVD oxide adhesion layer was deposited first in order to correct the problem. Fortunately, CVD oxide was used as the optical cladding layers for the waveguides anyway, so this step did not introduce any new variables.

3.3.2 Film Oxidation:

The determining criteria for whether or not films were "glassy" was somewhat crude in this thesis. The procedure was to visually inspect the films deposited onto clear microscope cover slides and assess their transparency by eye. If they were optically transparent then they were assumed to be fully oxidized, or at least oxidized enough for the purposes of this thesis.

For the bulk glass targets this was an easy task because all the films were clear. Producing oxidized films from the powder targets using the bipolar pulsed DC supply was a little more tricky because the plasma was very difficult to sustain with a 3:1 Ar:O_2 working gas flow ratio. In general, it was observed that high oxygen content made low pressure runs very difficult.

This problem could be the result of a combination of factors. First, the magnets in the magnetron were highly degraded, so it would be difficult to contain the plasma near the target. Additionally, oxygen could be promoting "target poisoning" which generally reduces the secondary electron generation which sustains the plasma.[31] Whichever the case, the plasma was not particularly stable and would extinguish itself regularly if the percentage oxygen content was too high and/or the pressure was too low.

In fact, the lowest stable pressure sustainable with the 2" gun was 8.4 mTorr, at quite a high argon to oxygen ratio of 21:1. Although the resulting film appeared to be clear, another film, deposited onto an angled substrate in a 6:1 Ar:O_2 environment, did not oxidize completely. It was partly silvered and part glassy. Thus, it was determined that a higher proportion of oxygen would have to be used to confidently produce oxidized films every time. In order to be as consistent as possible with the RF runs with bulk glass targets, 3:1 (and 4:1) ratios were adopted. In order to do this and maintain a robust plasma that would not randomly and spontaneously extinguish itself, the background pressure had to be raised to at least 15 mTorr.

3.3.3 Film Quality:

Film quality was crudely assessed by eye by estimating the extent to which the film surfaces were covered with tiny spots, or *speckles*. (A SEM micrograph of a typical speckle is shown in Figure 3.2.) The powder target film surfaces all appeared to be fairly clear; whereas the bulk glass films were more corrupted. In both cases thicker films suffered the most. Higher pressure was also seen to be a contributor to this effect. It is likely that internal stresses could have built up in the thicker films and that the spots are a manifestation of stress relief in the films. The conclusion would be to try to run at lower pressures and deposit thinner films.

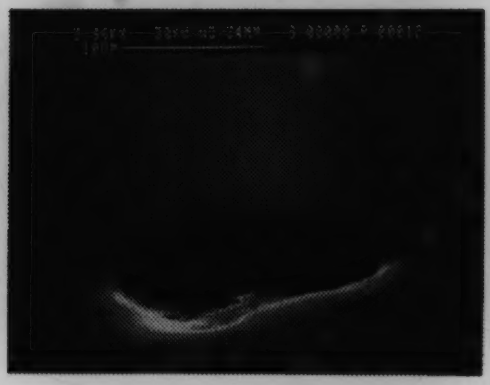

A typical "speckle" of oblong shape magnified at 3360 times. Like all the other observed speckles, it was observed to be a slight depression in the film surface

Figure 3.2

3.4 Film Thickness Profiles:

3.4.1 Films From Fused Quartz Targets:

Figure 3.3 shows the radial thickness profiles of the films sputtered from fused quartz targets. Tables 3.1 and 3.2 give the experimental conditions and deposition times. The thickness profiling was done with the prism coupler using the 632.8 nm HeNe laser. It was assumed and later confirmed that the sputter flux would be symmetric on both sides of the wafer, so only one half was profiled. This policy was adopted for all the films investigate in this thesis.

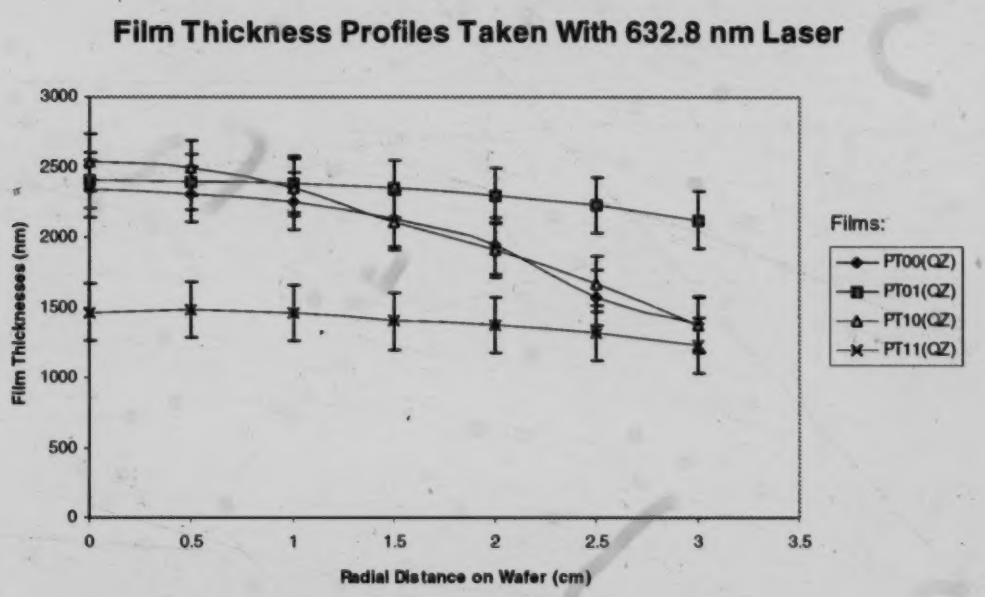

Figure 3.3 Film thickness profiles for films PT00(QZ) to PT11(QZ) sputtered from fused quartz glass targets, profiled using the prism coupler at 632.8 nm.

Thickness Uniformity:

The films deposited from close range had the highest deposition rates and were the least uniform. The result follows from the geometrical considerations of the chamber. In other words, the least number of particles are lost from short throw / low pressure runs. Conversely, long throw runs have the lowest deposition rates but are the most uniform.[34] The dominant effect is the geometry, and pressure is secondary. The ranking of deposition rates from highest to lowest was PT00(QZ), PT10(QZ), PT01(QZ), then PT11(QZ).

Simulation Results:

Sputtered SiO_2 film thickness profiles were simulated using SIMSPUD. The algorithm was described in Section 2.6, and the essential parameters described there were set to match the specific experimental parameters laid out in Tables 3.1 and 3.2. Although I simulated oxide films, the algorithm was designed to simulate elemental Si only. One of the challenges of this investigation was to see if this approximation was valid.

To this end, simulations of 900,000,000 particles were performed for each run, and two different initial flux distributions - cosine and cosine[8] were used. I wanted to see if changing the flux distribution would improve the accuracy of the simulations. The results are displayed in Figure 3.5, and some important observations are summarized in Table 3.4.

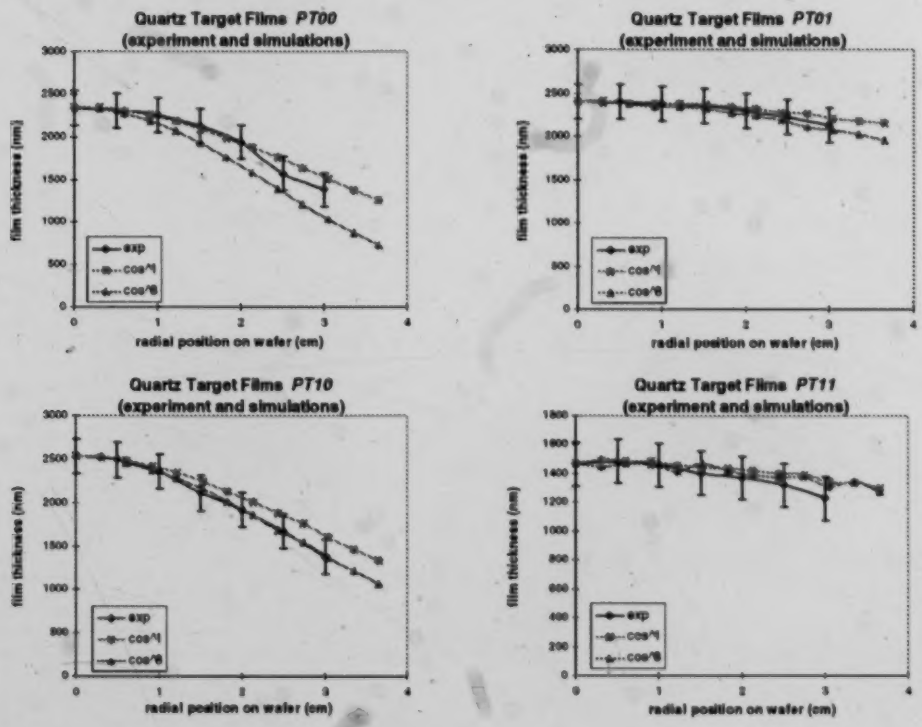

Figure 3.4 Simulated SiO_2 films overlaid with real films.

	PT00 (QZ)	PT01 (QZ)	PT10 (QZ)	PT11 (QZ)
Experimental Results: t(3cm) / t(0cm)	0.59	0.88	0.54	0.84
Cosine[1] Simulation: t(3cm) / t(0cm)	0.65	0.92	0.64	0.93
Cosine[8] Simulation: t(3cm) / t(0cm)	0.45	0.86	0.56	0.90
Least Difference: lexp - siml	0.06	0.02	0.02	0.06

Table 3.4 Difference in film thicknesses between real and simulated films. The lower the difference between the edge and centre of the films, the more accurate the simulations.

It can be seen that, SIMSPUD can actually predict the film thickness profiles of reactively sputtered SiO_2 to a fairly high degree of accuracy. It can also be concluded that, with the exception of film PT00(QZ), a cosine[8] distribution produces a somewhat better representation of

the data than a cosine^1 distribution. For this film, a cosine^1 simulation is quite accurate up until r=2 cm but then diverges somewhat thereafter. Using cosine^8, the simulation curves for Films PT01(QZ), PT10(QZ), and PT11(QZ) hug the data profiles quite accurately and are well within the data value error bars for the entire 3 cm radius.

This result shows how manipulating simulation parameters can affect the quality of simulations. It is possible that manipulating other parameters could also improve the results. The collision cross section is another obvious candidate that could be modified. Perhaps after testing out both these ideas more thoroughly under a number of different run conditions, some improvements could eventually be written into SIMSPUD's code to expand its capabilities to better simulate reactively RF-sputtered materials.

3.4.2 Films From Erbium-Doped Bulk Glass Targets:

Thickness Uniformity:

In this section, the results from the 1% erbium / ytterbium co-doped glass and the 3% erbium-doped bulk glass targets will be shown. The thickness profiles for the first material are shown in Figure 3.5. As before, the film thickness profiles were measured using the prism coupler with the 632 nm laser. For the 3% films, a 1550 nm - *telecommunications wavelength* - laser was used, as well. The profiles for the 3% Er-doped glass are shown in Figures 3.6, 3.7, and 3.9. Because 1550 nm is the telecommunications wavelength of interest for the amplification function of these films, the refractive indices measured at 1550 nm are actually more useful numbers. Time constraints (and lack of real need) prevented me from testing all the films at this wavelength.

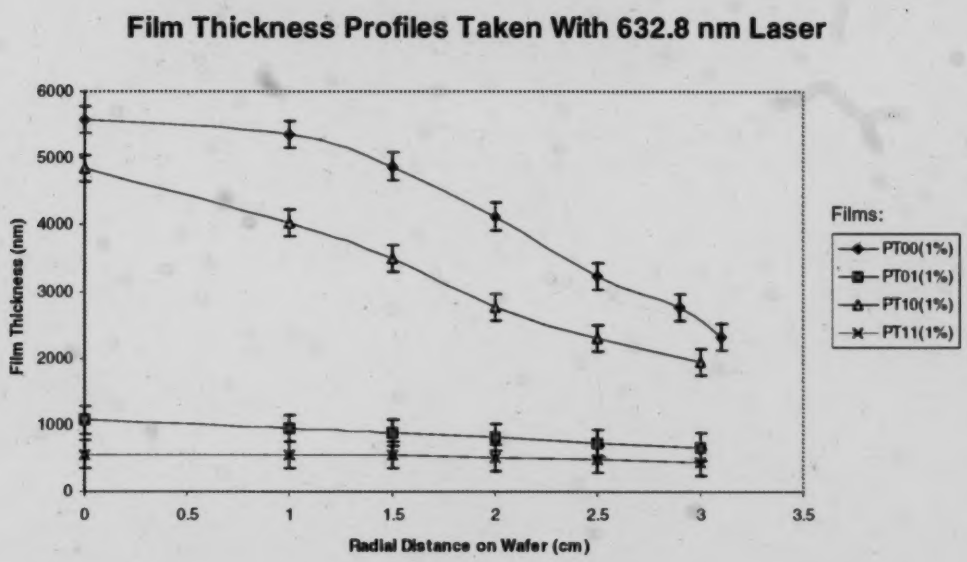

Figure 3.5 Film thickness profiles for films PT00(1%) to PT11(1%) sputtered from 1% erbium-doped bulk glass targets, profiled using the prism coupler at 632.8 nm.

The average deposition rates are clearly very low for these films. They range from a minimum of 3 to a maximum of 3.5 nm / minute when averaged over 2 cm. These runs took 23 hours to complete and the films ranged in height from roughly 0.5 μm to a little over 6 μm. Such a low deposition rate is not desirable from a production standpoint. Also, with the exception of the two long-throw runs, these films were quite non-uniform over their 3 cm radii. Although PT11(1%) was fairly uniform, it also happened to have the lowest deposition rate.

It is clear that the system power limitations imposed by the glass target's thermal stress susceptibility were a problem. Deposition is very slow, and the deposition times required for, say, a 1 μm thick film with reasonable uniformity would take a couple of days. Running for this long is not only cumbersome, but it adds a lot of general wear and tear to the pumping systems.

The 3% erbium-doped films' thickness profiles are taken with the 632.8 and 1550 nm lasers and are shown in Figures 3.6 and 3.7. The average deposition rates over 2 cm are also very low for these films. They range from a minimum of 5 to a maximum of 5.5 nm / minute. These runs were performed for 25.5 hours, and the films ranged in height from roughly 0.8 μm to a little

over 8 μm. It is not known why this material had a slightly higher deposition rate than 1% material.

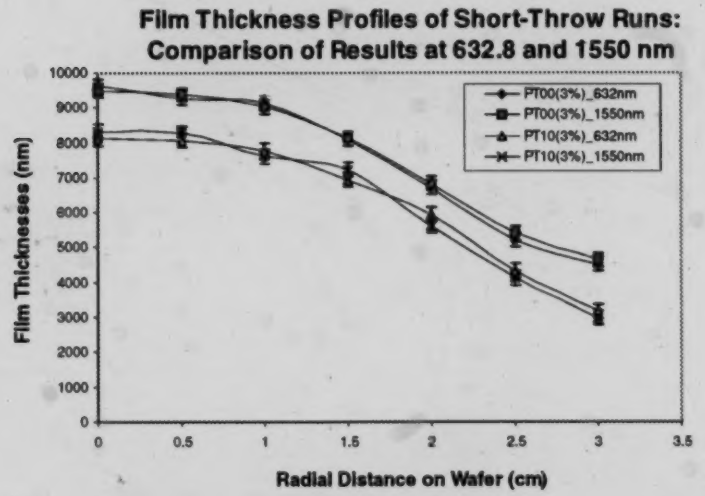

Film thickness profiles for films PT00(3%) and PT10(3%); comparison of prism coupler output at 632.8 and 1550 nm wavelength.

Figure 3.6

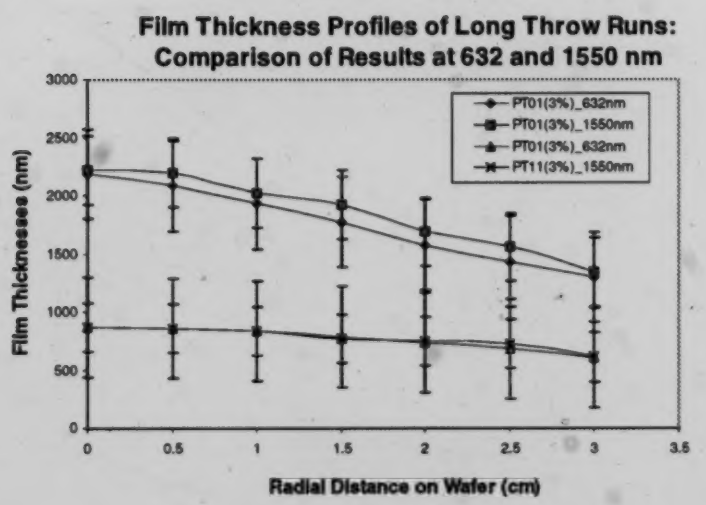

Film thickness profiles for films PT00(3%) and PT10(3%); comparison of prism coupler output at 632.8 and 1550 nm wavelength.

Figure 3.7

From the two sets of profiles of the 3% film it is also clear that there is a slight difference between the film thickness values measured at 632.8 nm versus 1550 nm. The average differences are 190, 95, 230 , and 10 nm for films PT00(3%) to PT11(3%), respectively. This is within the error bars.

Simulation Results:

In Section 3.4, SIMSPUD was used to simulate the thickness profiles of SiO_2 films sputtered from quartz substrates. In general, it was found - with the exception of PT00(QZ) - that simulation accuracy was somewhat improved if a cosine^8 flux emission distribution was used instead of a cosine^1 distribution. It was not necessarily concluded that this was the most important parameter to be manipulated.

In this section composite SIMSPUD thickness profiles were assembled in order to simulate the 3% erbium doped glass films, PT00(3%) to PT11(3%). It was possible to perform these simulations because the chemical composition of the source glass was available from the microprobe analysis (see Table 3.5). Each simulation was complied as an algebraic summation of the thickness profiles for the individual elements. Each element was weighted according to its atomic occurrence fraction in the target, its deposition efficiency, and estimated molecular volume. The algorithm is described in Appendix B.

The purpose for attempting this simulation was to determine whether it could be done with any accuracy and, if so determine if it could account for the observed experimental results. The hope was that this method of simulation could be explored more thoroughly in the future and perhaps one day become an algorithm improvement that could be incorporated into the SIMBAD/SIMSPUD code.

La	Si	Na	Ba	Er	Zn	K	Ce
23.38	21.48	7.30	4.72	2.81	2.43	1.69	0.14

Table 3.5 Chemistry of source as determined by microprobe. Oxygen, boron, lithium, and chlorine impurities are not accounted for. (see also Table 4.2)

The simulations were not as smooth in appearance as the simulated quartz films. This was a direct result of launching 100 times *fewer* particles for any given element than for the SiO_2 simulations. If each simulation had been run with 900,000,000 particles as was done for SiO_2 rather than 9,000,000 then the profiles would be less erratic, but it would have taken an extremely long time to run 64 simulations.

The composite film simulations are not in as good agreement with experiment as the quartz simulations. They were still fairly reasonable, however, especially considering that numerous simplifying assumptions were made. The general conclusion is that the cosine^8 simulations were more accurate in all four cases; although PT01(3%) agreement was not very good in either case. Film PT00(3%) was the best simulation and Film PT11(3%) was good, as well. These results are shown in Table 3.6.

It can be seen in Table 3.6 that the $t(3\ cm)/t(0\ cm)$ ratios for these composite simulations are actually very similar to the Si simulation results from the quartz target in Table 3.3. A reasonable explanation for this is that the most abundant element, Si, dominates the simulation results and essentially sets the trend.

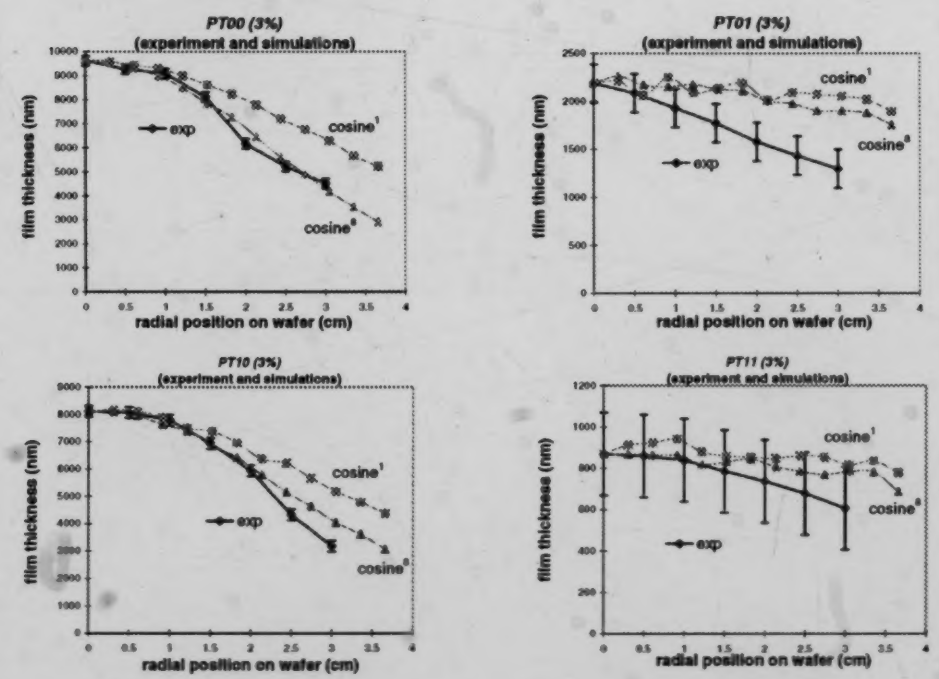

Figure 3.8 Composite film thickness profiles for the glass films, PT00(3%) to PT11(3%).

	PT00 (3%)	PT01 (3%)	PT10 (3%)	PT11 (3%)
Experimental Results: t(3cm) / t(0cm)	0.47	0.59	0.39	0.70
Cosine[1] Simulation: t(3cm) / t(0cm)	0.66	0.89	0.65	0.92
Cosine[8] Simulation: t(3cm) / t(0cm)	0.43	0.85	0.50	0.85
Least Difference: lexp - siml	0.04	0.26	0.11	0.15

Table 3.6 Film thickness decrease fractions at 3.0 cm and 0.0 cm for real and simulated films.

3.4.3 Films From Powder Metal Targets:

Figure 3.9 shows the thickness profiles for the films made from the undoped alumino-silicate powder targets. Both of these runs were done for two hours.

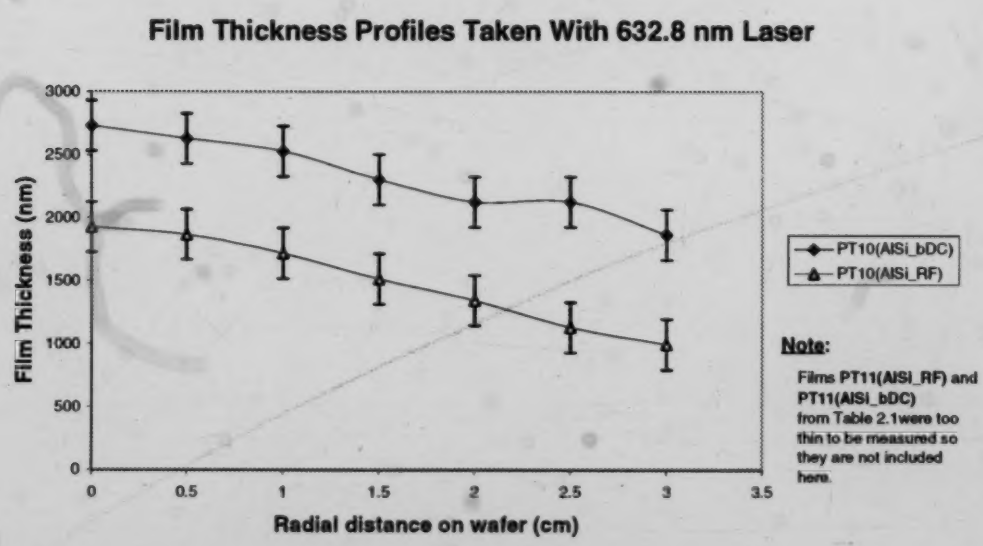

Figure 3.9 Film thickness profiles for films PT10(AlSi_RF) and PT10(AlSi_bDC).

It is clear from the graph that the bipolar pulsed DC supply produces a higher deposition rate. The rates, averaged over 2 cm are 20.5 and 13.9 nm / minute, respectively. Thus, bipolar pulsed DC was found to provide 1.47 times faster deposition than RF. This substantiates the manufacturer's claims; although it was not as high as the 1.75 times difference that they observed and quoted.[31] Nonetheless, it is still obvious that higher deposition rates were possible with this system than with bulk glass targets. This, in itself, is a process improvement.

Another one of the manufacturer's claims about the powder targets was that bipolar pulsed DC sputtering produces more uniform films than RF. The plots do not clearly support this claim, but detailed examination of the actual numbers suggests that it is true. For example, the percent decrease in thickness over 3 cm for the bipolar pulsed DC run is 31.8% while it is 48.4% for the RF run. This translates to a real drop in thickness of 868 and 933 nm, respectively. As such, it can be concluded that, for a given power, the pulsed DC sputtering technique produces thicker, more uniform films.

Figure 3.10 shows the thickness profiles for the films made from the Er-doped alumino-silicate powder targets. The individual deposition times for these films are shown in Table 3.2.

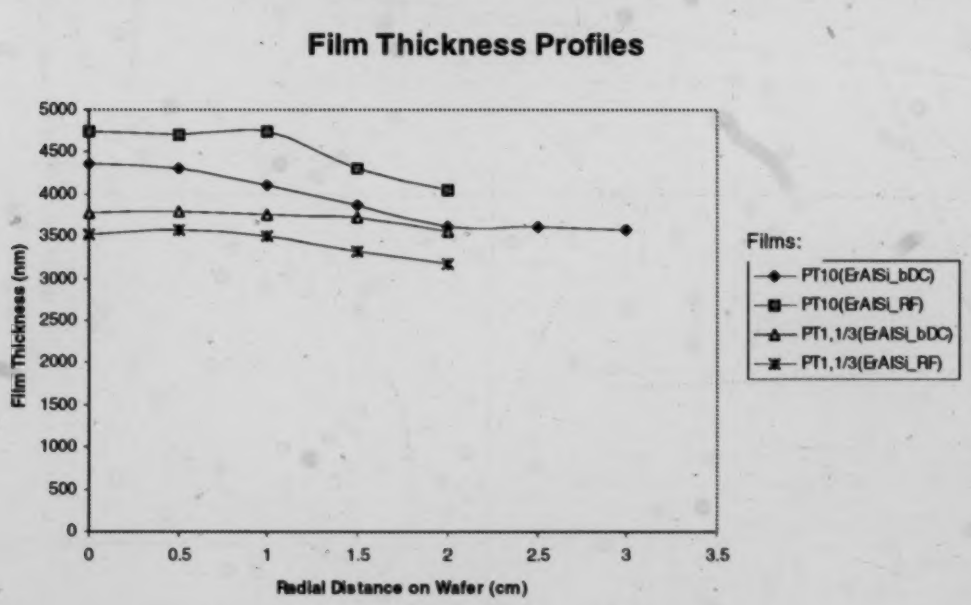

Figure 3.10 Film thickness profiles for films erbium-doped powder target glass.

3.4.4 Summary from Thickness Measurements:

Experiments:

The highest deposition rates achieved were for the low pressure, short throw runs. Unfortunately, these films were quite non-uniform. More uniform films could be made by increasing the target-substrate separation, but the deposition rates dropped off to unacceptably low values. In principle the situation could be alleviated if the substrates were deposited onto a planetary motion variable-position substrate tray. With such a system modification, the deposition rates would be kept up without compromising uniformity. Overall, the highest deposition rate obtained for the erbium-doped films was for PT10(ErAlSi_bDC).

Simulations:

The numerical simulation tool, SIMSPUD was used to generate the thickness uniformity profiles for multiple-oxide sputtered glass films. Quite good accuracy was found for SiO_2 films, and reasonable accuracy was obtained for a complex multiple oxide glass. It was found that in some cases the simulations were improved dramatically if the initial flux distribution profile was changed from cosine^1 to cosine^8.

3.5 Film Microstructure:

The purpose of this section was to determine whether the sputtered glass films possess a columnar microstructure. The motivation for this was two-fold. First, it was to further general understanding of the sputtered glass to possibly illuminate some film growth mechanisms. Second, it presents an opportunity to utilize the new film growth simulator program, GROFILMS, and test whether it can emulate the microstructure of a sputtered glass film. In this case SiO_2 film PT11(QZ) was simulated because it displayed the most prominent microstructure.

In Chapter 1 how it was described that column boundaries in glass films would contribute to energy loss from light-scattering and most likely exacerbate erbium segregation and clustering effects. As a result, microstructure could be a significant performance factor and could potentially reduce or completely eliminate spontaneous emission.

3.5.1 Films From Fused Quartz Targets:

In this section, SEM photographs of the four films are presented in Figures 3.11 to 3.14 and are divided into two columns. The left column shows unetched film; while the right column shows films which have been lightly etched in 50:1 BOE solution to accentuate structural details. The upcoming qualitative observations will not be expounded upon in too much depth here - just enough to show if and when a basic correlation between sputtered glass microstructure and deposition conditions can be made.

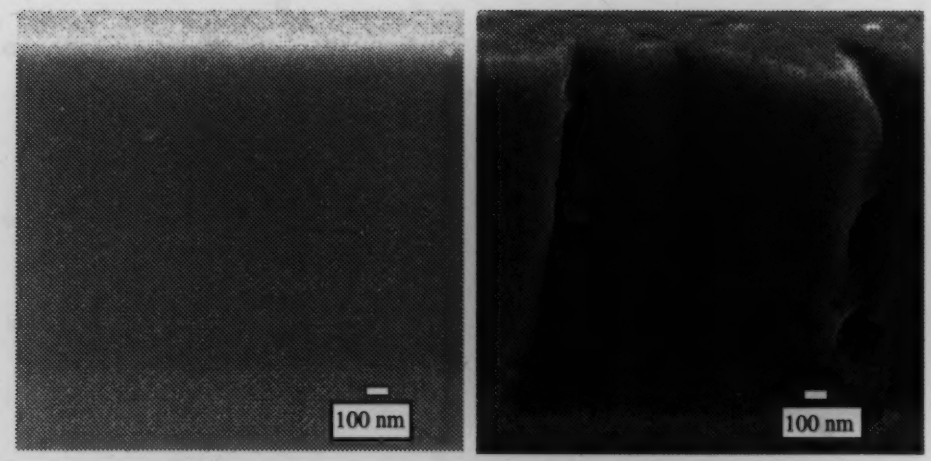

Figure 3.11: Film 1 *(PT00)* at 40,000 times magnification:

(a) Not etched - no features are visible

(b) Definition etched in 50:1 BOE for 10 seconds. Cross sectional features may just be the fracture patterns accentuated by the etch. Structure seems to be visible on the film surface, however.

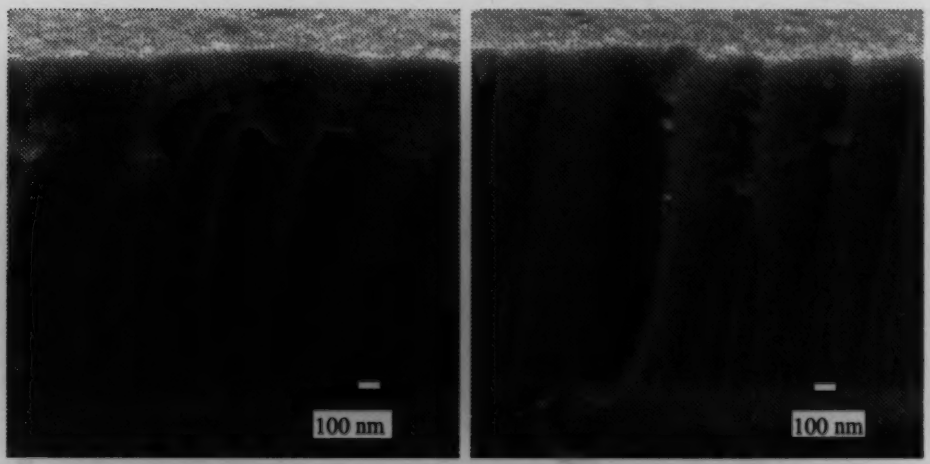

Figure 3.12: Film 2 *(PT01)* at 40,000 times magnification:

(a) Not etched - fracture patterns are visible and may follow actual film microstructure if there is any (this image is at a slight 3D perspective so columns appear to be curving out from the edge of the film).

(b) Definition etched in 50:1 BOE for 10 seconds - the fracture patterns may be accentuated. Delta patterns are clearly accentuated this time. It is not known if this is actual structure or just fracture pattern.

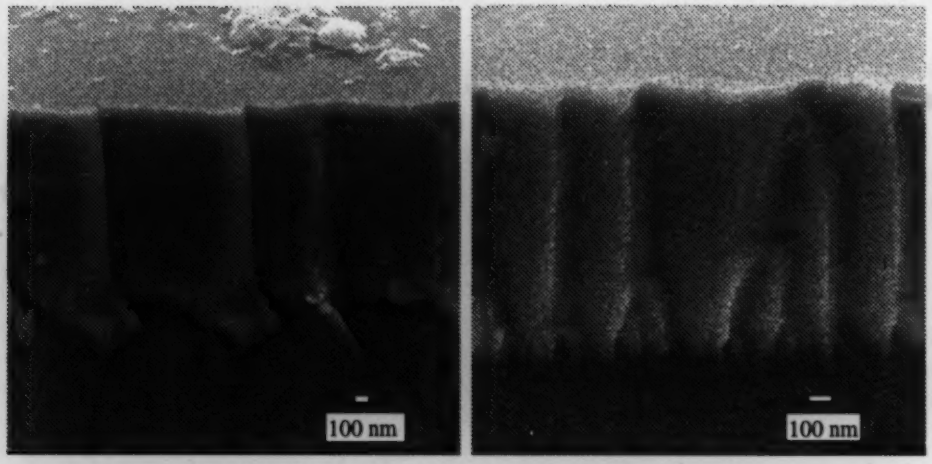

Figure 3.13: Quartz target Film 3 *PT10* at 20,000 times magnification:

(a) Not etched - the structure in this photo is typical of a concoidal glass fracture, so it is suspected that this is just a fracture pattern.

(b) Definition etched in 50:1 BOE for 10 seconds. The concoidal edge profile is still evident but some interesting structure has been delineated by the etch at the bottom of the film

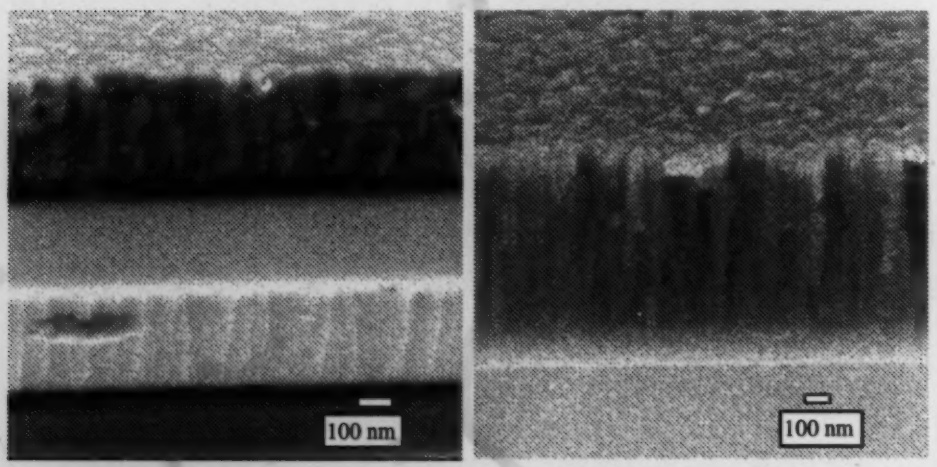

Figure 3.14: Quartz target Film 4 *PT11* at 20,000 times magnification:

(a) Not etched - structure is definitely visible here. (In this image the film has broke away from the CVD underlayer here, so two layers can be seen.) The concoidal lobe patterns visible in previous films can be seen in the bottom CVD layer. This is a strong indication that the "lobes"are not microstructure.

(b) Definition etched in 50:1 BOE for 10 seconds.

Microstructure is very apparent. This seems similar to (but more dense than) a Thornton "zone 1" structure film [62]

General Observations:

With the exception of PT11(QZ), the films did not show much microstructure and were quite amorphous. Large concoidal features are evident in Figures 3.11 to 3.13, however, especially in the short throw runs. It was originally thought that these might indicate some sort of structure within the films. Upon closer examination, the concoidal patterns were found to be merely fracture marks. Similar "lobed" edge features can be seen in Figure 3.14(a) in the fracture pattern of the CVD oxide adhesion layer. Nonetheless, it is possible that the interpretation of the photo is being actually being complicated by the presence of both fracture patterns and structure. For instance, at the base of the etched films there is what looks to be the beginning of vertical columnar growth. As well, in Figure 3.13(b), some "river delta" patterns can be seen in the etched films. Such patterns are consistent with microstructure arising from competitive column growth.[34]

One thing is certain with PT11(QZ). The evidence of glass microstructure is unambiguous. The SEM photos clearly show this, and it was also observed that this film scratched very easily when a plastic scribe was lightly drawn over it. In other words, its loose microstructure caused it to be considerably softer than the other films. It will be shown in the next section that this film also had the lowest index of refraction.

The basic conclusions are that sputtered quartz films are quite amorphous under a range of deposition conditions. Nonetheless, high pressure / long throw deposition seems to produce films with very open microstructure. Such a film would be very poor for transmitting light because most of it would be scattered away at the column boundaries.

Simulation Results:

Figure 3.15 shows the GROFILMS simulation of PT11(QZ). This 9 billion-particle simulation was performed by Loran Friedrich, and the composite image was assembled by me. The simulation methodology used was to try to create a near-Zone 1 film. Loran selected these parameters in order to try to create what he hoped was a "Zone 1" film. This type of growth is typical of materials with high melting temperatures and low diffusion lengths. The films are described by the Thornton Zone Model[62] and are characterized by highly visible microstructure with domed columns. It is clear that the etched film exhibits this type of growth to some degree; although actual Zone 1 material is somewhat less dense than this.[62]

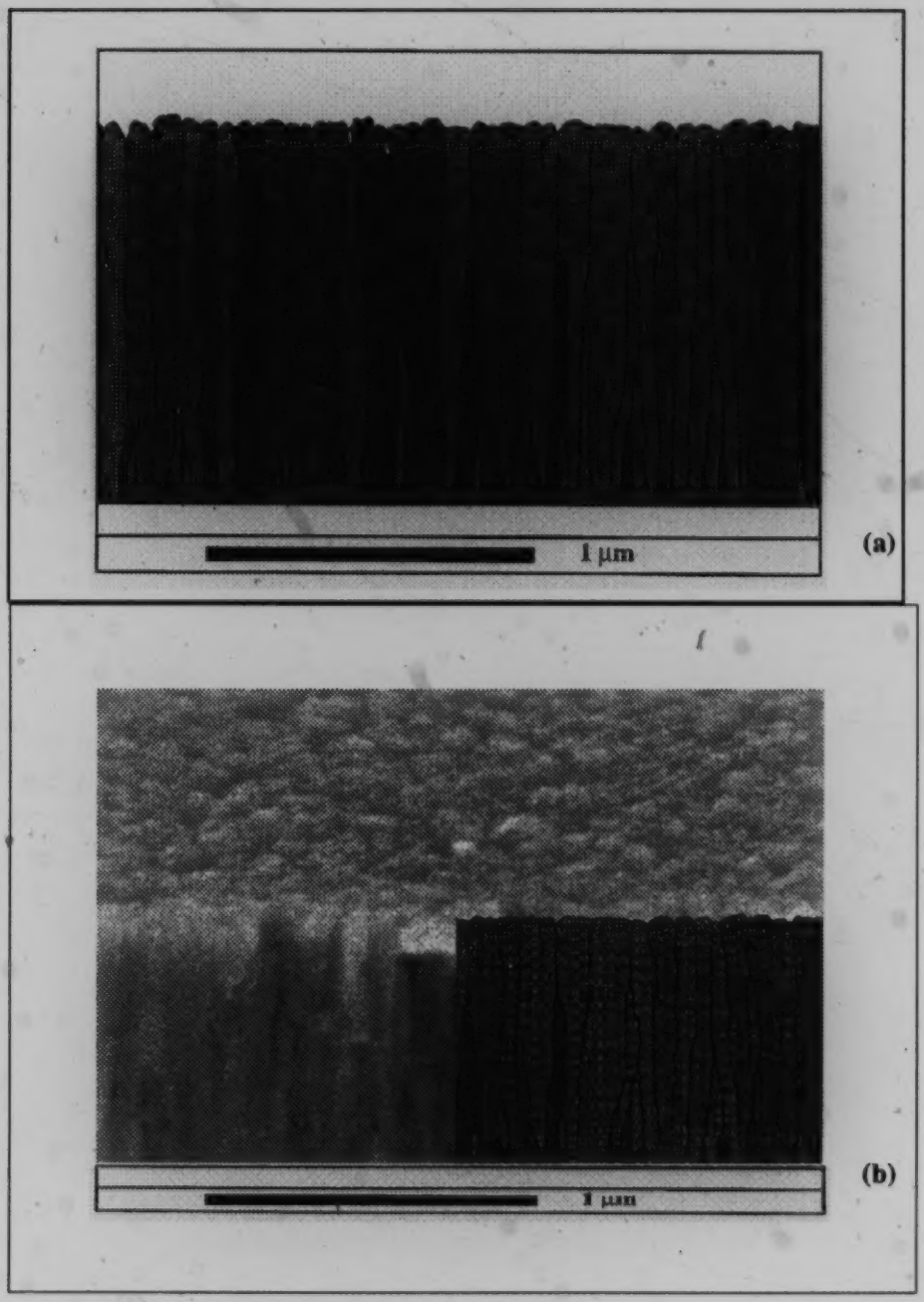

Figure 3.15: (SEM magnification is 20,000 times)

(a) A GROFILMS simulation of Film PT11(QZ)
(b) Actual SEM photo of film PT11(QZ) superimposed with the simulation.

Over the course of its development, a considerable array of GROFILMS simulations for copper were performed by Loran Friedrich.[52] As a result, he had a very good feel for its diffusion characteristics. For instance, copper - which melts at approximately 1083°C[63] - was simulated with a typical diffusion length of near 0.125μm. By means of comparison, fused quartz melts at approximately 1700°C.[56] As a result, a simulation diffusion length of 0.004 μm used for SiO_2. The simulation shown here is essentially a "visual data fit" where parameters are generated based on the operator's experience in order to correlate them with the experimental image.

It is not obvious whether the parameters used would actually have anything to do with the real physical constants of the glass material, but if they do then this is a potentially very powerful way of illuminating complicated and esoteric physical properties of glass films. If not, at least it is a useful demonstration that GROFILMS can be tailored to mimic the size and shape of an arbitrary film quite effectively and easily.

3.5.2 Films From Erbium-Doped Bulk Glass Targets:

Figures 3.16 to 3.18 show a representative sampling of some SEM photos of the 1% erbium-doped films. Only film PT11(1%) was photographed because this was the one that should have exhibited the most microstructure. The films were deposited onto flat and angled substrates, and the substrate angles were increased from 0° to 40° to 60° to 80°. The substrate was tilted in order to help delineate and accentuate any microstructure that may have been present.

Figure 3.16 is a typical cross section of film PT11(1%). It shows no major glass microstructure. This was typical of the films deposited below. At this deposition angle, however, the cross section showed definite traces of glass microstructure. (Notice the column boundaries between alternately shaded regions in Figure 3.17.) Figure 3.18 is a SEM photo of an 80° angle deposited film section that was definition-etched prior to being photographed. In this figure columnar structure is highly visible.

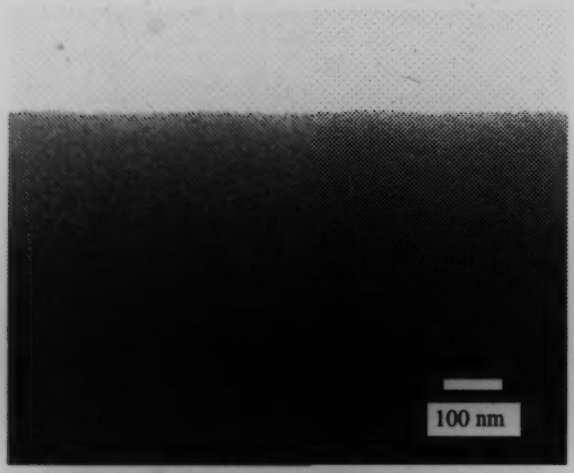

Cross section of PT11(1%) deposited onto a flat substrate.

No microstructure is visible.

Figure 3.16

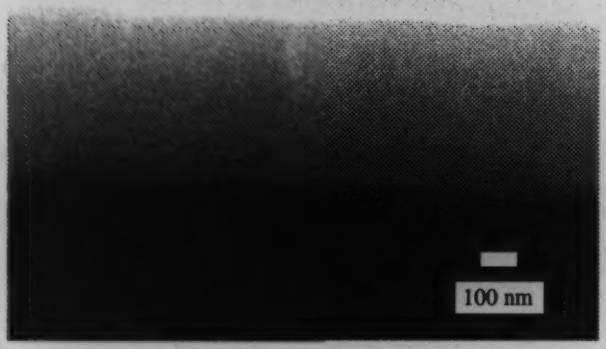

Cross section of PT11(1%) deposited at 80°. No etch was performed here.

Some structure is starting to become evident.

Figure 3.17

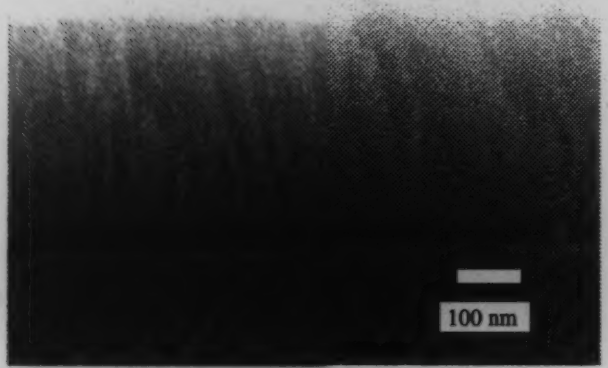

PT11(1%) deposited at 80° and definition etched for 10 seconds in 50:1 BOE.

Structure is now clearly visible.

Figure 3.18

The basic conclusion from this investigation is that the sputtered glass films from these erbium-doped glass targets are essentially amorphous. It was shown, nonetheless, that they can evolve in a columnar manner under extremely highly tilted deposition conditions. The columns become especially evident after a definition-etching has been performed.

3.5.3 Films From Compressed Powder Metal Targets:

The following figures are SEM cross-sections of films PT10(AlSi_RF) and PT10(AlSi_bDC) sputtered from the un-doped powder metal target. No cross section SEM photos were taken of the erbium-doped material.

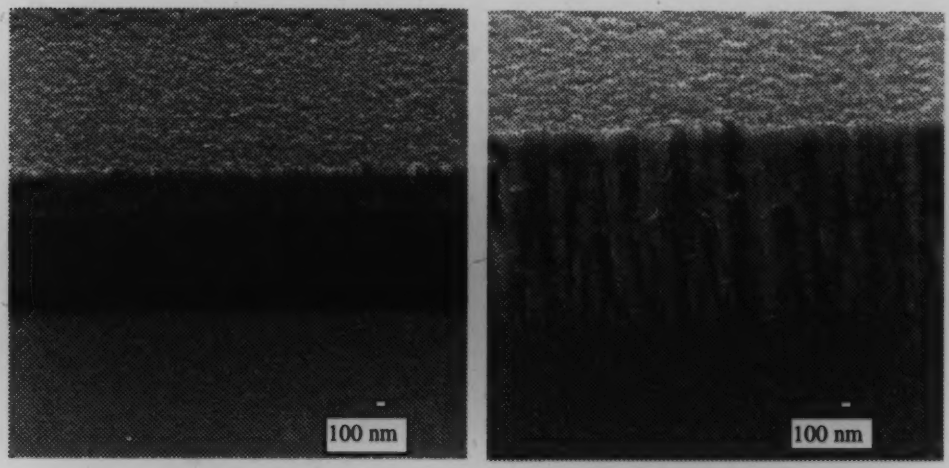

(a) SEM Cross section of the RF sputtered film, PT10(AlSi_RF). (20,000x magnification)

(b) SEM Cross section of bipolar pulsed DC Film, PT10(AlSi_bDC) (20,000x magnification)

Figure 3.19

It is evident from the pictures that these films have quite a porous structure - on the order of or even higher than film PT11(QZ). It is not known why they exhibit such disproportionately higher columnar structure than the previous glasses, but it could have to do with the higher sputtering pressure that was used. High pressure tends to yield looser structure.[28] It is also possible that it could have something to do with the reaction mechanism occurring at the substrate.

From the micrograph, it also appears that the RF sputtered film has the higher density of the two films. This is a difficult to assessment to make visually, and it has not been supported up by any density measurements. Nonetheless, this hypothesis will be supported in Section 3.6.3 where it was determined that the RF sputtered film has a higher refractive index.

3.6 Annealing the Glass Films:

In several papers concerning erbium-doped films, post deposition annealing was seen to improve spontaneous emission properties of the films.[50][51] Consequently, it was decided that this would be an avenue to explore in this thesis, as well. The purpose of this section is to identify an annealing process that would be suitable for subsequent spontaneous emission tests. The point was basically to compare unannealed films to annealed films, not to characterize a number of different annealing conditions. The basic "suitability" criteria was what process caused the least visually observable surface damage to the films.

3.6.1 Tube Furnace Annealing:

Samples of all four 1% erbium-doped films - PT00(1%) to PT11(1%) - were annealed for varying lengths of time in the tube furnace at approximately 300° C. The annealing conditions are shown in Table 3.5. Even at these relatively low temperatures, the appearance of the film surfaces changed significantly. (The temperatures are well below all the individual oxides' boiling points and the manufacturers quoted glass melting temperature of approximately 700° C.) That is, the surfaces became more noticeably spotted. The extent depended on the anneal conditions. The longer the anneal and the higher the temperature- the more spotted the films became. Even after as little as 15 minutes this effect was noticed.

Annealing Conditions:	Observations:
1. 290° C for 30 minutes	*Film surfaces are all speckled.*
	(PT00(1%) is clearly the worst.)
2. 300° C for 5 minutes	*No change of the film surfaces*
3. 300° C for 15 minutes	*Some change of the film surfaces*
4. 300° C for 20 minutes	*Tiny speckles appear on the film surfaces.*
	(Film PT00(1%) is the most noticeable)
5. 350° C for 30 minutes	*Minor change to film surface*
6. 360° C for 15 minutes	*Films all develop more speckles*
	(Again PT00(1%) is clearly the worst.)

Table 3.7 Specific annealing condition data for Er 1% film.

The thicker films, sputtered from relatively close to the target, appeared to suffer more dramatically than the thinner films sputtered from far away. In particular, PT00(1%) consistently suffered the worst. Notably, the pressure_distance product was lowest for this film, so it would have been "pounded" with the highest momentum impinging sputter flux during deposition. It is possible that the spotting observed after annealing was a relief mechanism for internal film stresses that had built up.

Figures 3.20 (a) and (b) are SEM micrographs of the spots. Both shots are of PT00(1%) annealed for 30 minutes at 290° C, and both clearly show voids formed in the film surface. The white regions in the second shot appear to be raised up from the surface. The domed structure could be the result of gas evolution which could have caused bubbles to form and eventually pop. After the bubbles popped, the voids were left behind. Alternatively, these features could also be the result of a stress relief mechanism in the films.

It is possible that the speckles observed prior to annealing could have acted as nuclei for these voids. The previous features did not occur in nearly this density, however, and were mostly oblong-shaped rather than circular. It is plausible, nonetheless, that minimum energy surface tension effects could have caused them to evolve into circles or spheres.

The conclusion is that tube furnace annealing is potentially very problematic. Even so, it was determined that a "conservative" tube furnace anneal at 300° C for 5 minutes was a suitable process for all films. This method was used for the erbium-doped powder target films, as well.

They sustained no visible surface damage during the process. Rapid thermal annealing *(RTA)* might be a better approach since the time available for "void evolution" would be minimized.

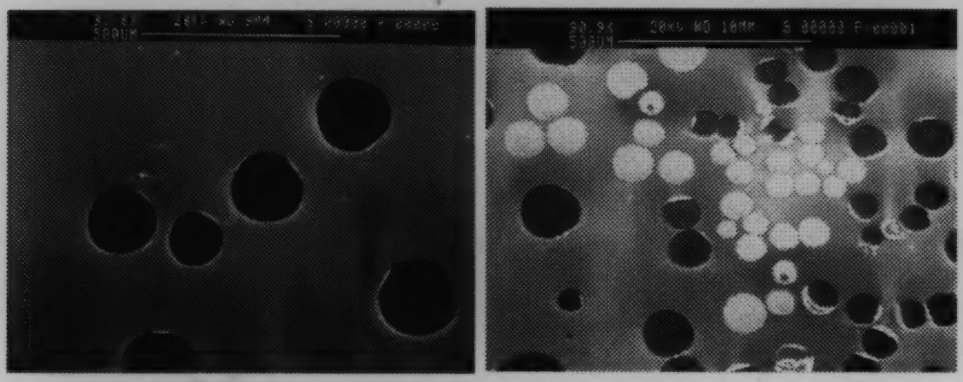

(a) Voids that have formed in PT00(1%) after 30 minutes of annealing at 290° C.

(b) Voids and "bubbles" on the surface of PT00(1%) after 30 minutes of annealing at 290° C.

Figure 3.20 Voids in film from bulk glass targets that form after annealing.

3.6.2 Rapid Thermal Annealing (RTA):

In the process of determining rapid thermal annealing temperatures and times, various conditions were investigated ranging from 10 seconds at 600°C to 45 seconds at 800°C. I decided to used as high a temperature as the films could handle to accentuate any beneficial effects that the annealing action hopefully was going to cause. In the end, a 30 second anneal at 700°C was decided upon.

Visual and SEM inspection of all the films annealed under these conditions showed them to be clear of speckles and delamination. However, closer examination of an array of waveguides etched on film PT00(3%) using the SEM indicated that some microscopic damage may have occurred and was accentuated by the etch. Figure 3.21 shows some circular patterns on the film's surface. Despite these imperfections, all RTA'd films were still tested for spontaneous emission. The results are presented in Chapter 5.

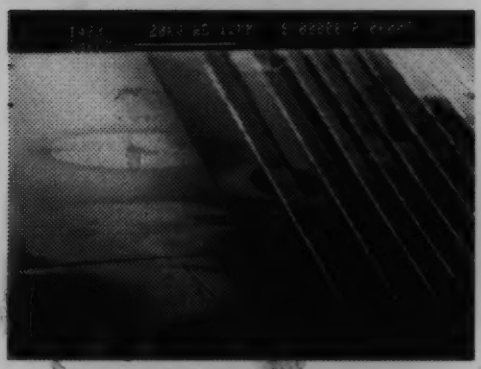

Sample SEM of a PT00(3%) waveguide array RTA'd for 30 seconds at 700°C. Microscopic circles can be seen in the film, but the waveguides were tested for spontaneous emission anyway.

Figure 3.21

3.7 Film Refractive Index Profiles:

The following section shows all the refractive index profiles of the films characterized in this thesis. Refractive index and film thickness readings were output simultaneously from the prism coupler, so these results are actually paired with the thickness measurements from Section 3.4. Profiling was done at 632.8 nm for all films. For the 3% erbium-doped glass and erbium-doped powder target runs, a 1550 nm laser was used, as well. The lateral resolution of the radial distance measurements is +/- 1.5 mm due to the size of the coupling spot.

3.7.1 Films From Fused Quartz Targets:

Figure 3.22 shows the index profiles for the quartz-target films. A bulk index value [61] was overlaid on the data. An experimentally-determined value for the bulk could not be determined using the prism coupler because the target's surface was too rough for light coupling. The reference value used was 1.459.[56]

The ranking of refractive indices from highest to lowest is: PT01(QZ), PT00(QZ), PT10(QZ), then PT11(QZ). One would have perhaps expected PT00(QZ) to have the highest index - not PT01 - because it would apparently have the highest flux impingement momentum at the surface of the wafer. Momentum considerations were not straightforward here, however, since PT01(QZ) was actually run with 50 W more power than PT00(QZ), so the flux would correspondingly be more energetic.

The refractive index profiles were fairly uniform from centre to edge in these films if not slightly *decreasing* in value. This is a fairly intuitive result. One would postulate that the central region of the substrate, where the sputtered particles bombard with the most vertical momentum, would have the most compact and highest density film. Furthermore, the sputtered particles landing at the radial extremities of the wafer will arrive with more oblique incidence, causing a looser microstructure to develop. This can be explained by the "tangent" or "Tait" rules.[36]

What implies that the optical density, or *refractive index*, should be highest at the centre, as well.[36] The hypothesis is confirmed by PT11(QZ) - a film that displayed the strongest tendency to drop in index value from centre to edge over 2 cm and the most visible columnar structure. Curiously Film PT10(QZ)'s index drops off quickly after 2 cm. This drop could suggest that the film is less dense at the radial edges than at the centre of the film.[36]

It is curious that the quoted refractive index of the bulk glass is lower than that of some of the films. Upon first consideration of film versus bulk density, this effect seems counter-intuitive. One would think that the films would almost certainly be less dense than the bulk material, but a closer look reveals that this is not necessarily so. The quoted density of fused quartz is 2.2 g/cm^3. Some experimental results from Chapter 4 show that the film density is actually higher than this. This could be because the films are amorphous while the fused quartz is crystalline. Nonetheless Film PT11(QZ), had an index of refraction that was well below that of the bulk material. This film displayed the most obvious microstructure of the group of films, and it is likely that its density was lower, as well.

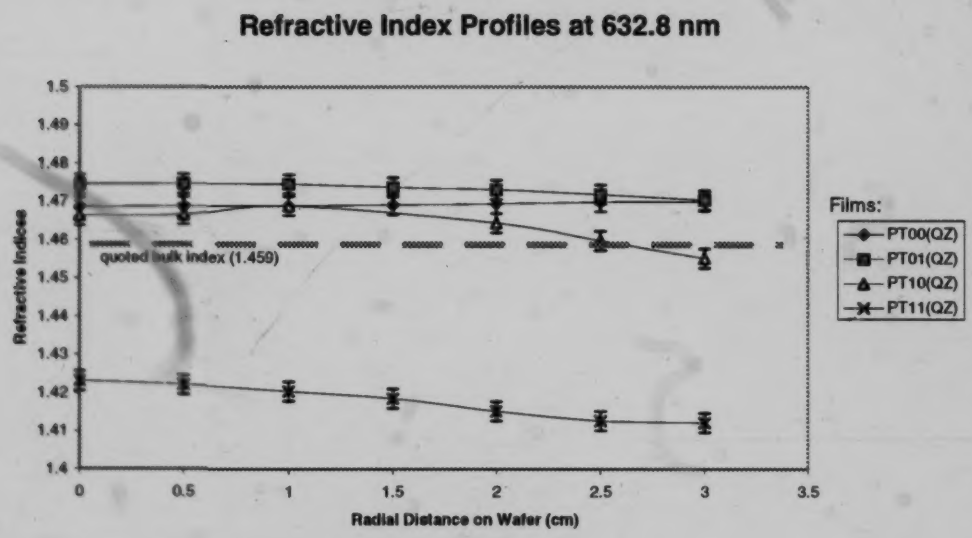

Figure 3.22 Refractive index profiling for the quartz glass at 632.8 nm. Bulk index value provided from [56].

3.7.2 Films From Erbium-Doped Bulk Glass Targets:

Figures 3.23 to 3.25 show the refractive index profiles for films sputtered from erbium-doped bulk glass targets. The first figure shows the refractive index profiles for the 1% erbium, ytterbium-co-doped glass at 632.8 nm; while the latter two figures show the profiles for the 3% erbium-doped material taken with both the 632.8 and 1550 nm lasers. The measured and manufacturer's bulk index values are superimposed on all these plots. The discrepancy in values will be discussed in Appendix A.

One surprising result is that the ranking of refractive indices for both sets of films is the exact opposite to that of quartz. The ranking from highest to lowest is: PT11, PT10, PT00, followed by PT01. I have no explanation for this at this time.

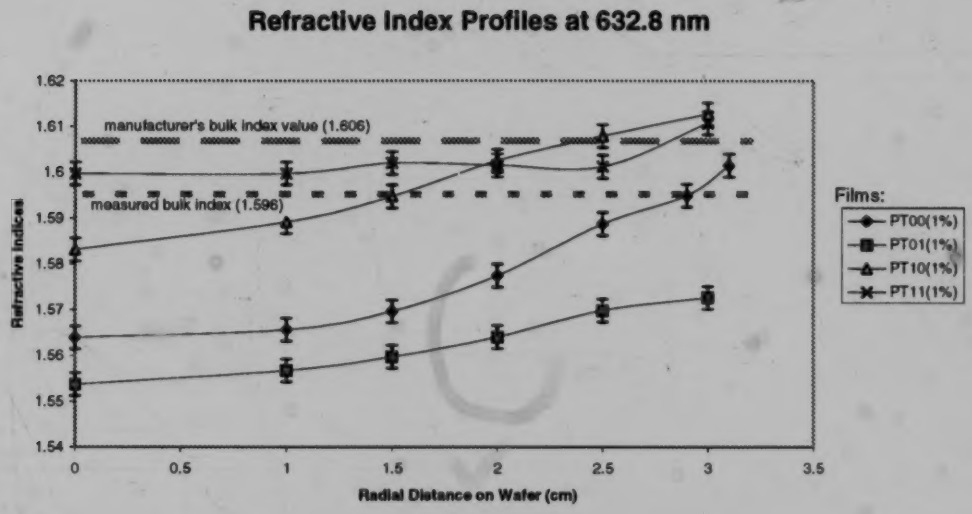

Figure 3.23 Refractive index profiling for the 1% erbium-doped glass at 632.8 nm.

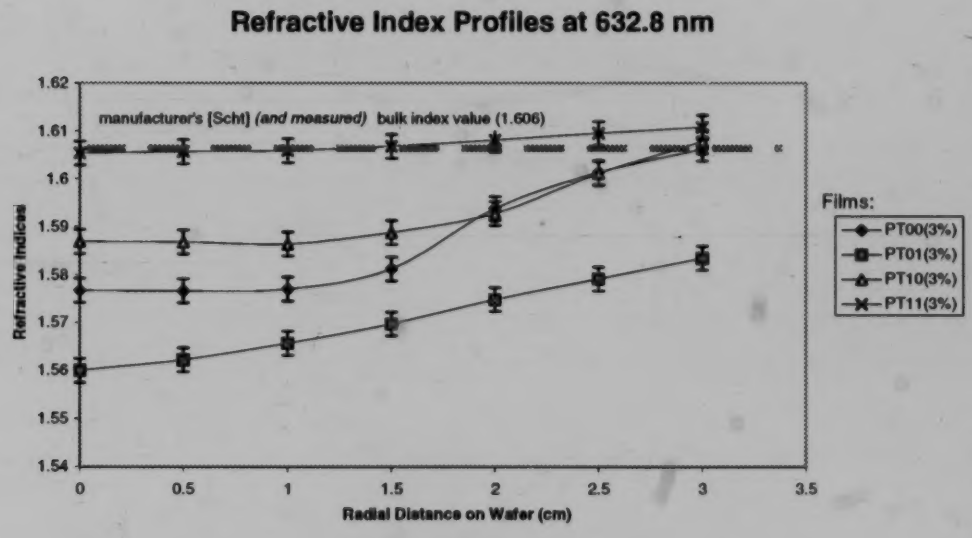

Figure 3.24 Refractive index profiling for the 3% erbium-doped glass at 632.8 nm.

Perhaps an even more unexpected result in this section is that the films' refractive indices increase from the centre to the edge of the wafer. This is true for both the 1% and 3% glass. It was explained in Section 3.5.1 how the central region of the substrate should have the most

compact and highest density film. This is where the sputtered particles bombard with the most vertical momentum, Furthermore, it was described why sputtered particles landing at the radial extremities of the wafer should have a looser microstructure and why this should cause the optical density, or *refractive index*, to be lowest there.[36]

The refractive index behaviour observed here contradicts these predictions. At the centre, the indices are all well below bulk value; whereas at the edge they approach and in some cases cross over the bulk. The most dramatic changes over 3 cm are experienced by PT00(1%) and PT00(3%), where 2.4% and 1.9% increases are observed. These increases equate to fairly significant index changes of 0.0376 and 0.0295, respectively.

These results are very curious and suggest a couple of possible explanations. The first is that the physical density of these films could be varying in a counter-intuitive fashion across the wafer surface, increasing from a low value at the centre to a value closer to bulk edge. This may be an unrealistic hypothesis, however, because the films appeared to be completely amorphous in the SEM photos in Section 3.4.2. As such, it is unlikely that there would be a significant density variation. It is more likely that a chemical variation occurred either during deposition or after the flux landed that caused the index to be so much lower at the centre of the wafer. Both of these hypotheses are investigated in Chapter 4.

One conclusion that can definitely be drawn is that the sputtered films differ from the target material in *some* way. This answers one of the major question proposed in Chapter 1. This result may be a symptom of the problem that inhibits the active optical performance of these films. In Chapter 5, for instance, it is described how sputtered glasses did not exhibit nearly as pronounced light absorption or spontaneous emission as the bulk glass. Also, in Chapter 4, it was confirmed that there are compositional differences between the source glass and film.

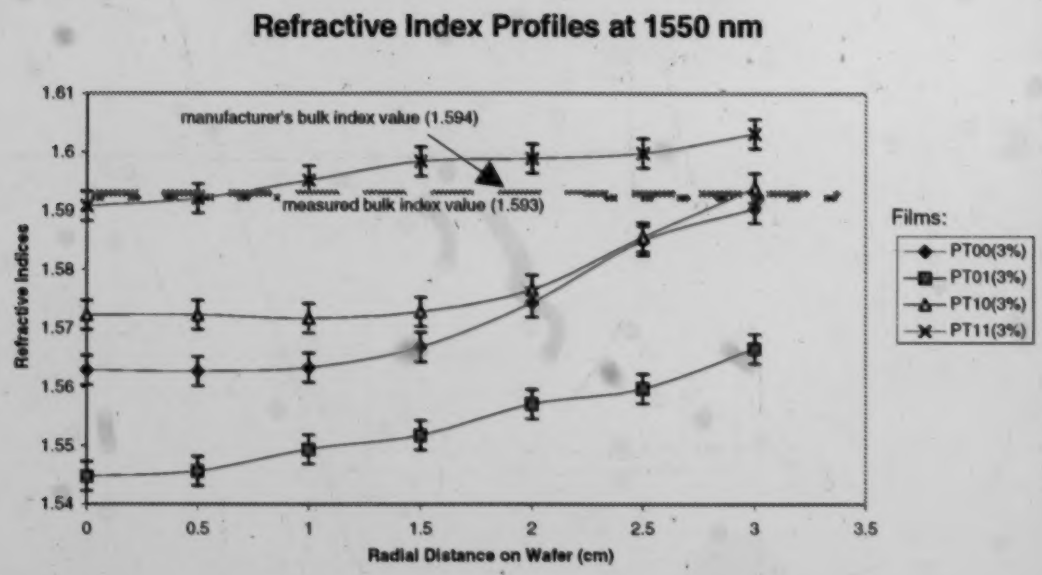

Figure 3.25 Refractive index profiling for the 3% erbium-doped glass at 1550 nm.

In Figure 3.25 it can be seen that the refractive indices of the 3% glass films measured at 1550 nm are lower than at 632.8 nm. The difference is roughly 0.015 on average. This is likely due to a well understood and expected effect caused by wavelength-dependent dispersion.[64]

3.7.3 Films From Conductive Powder Targets:

Figure 3.26 shows the refractive index profiles for the undoped glass films sputtered from compressed alumino-silicate metallic powder targets. The figure indicates that the films exhibit a pronounced drop in index from centre to edge This result is expected considering the high degree of structure that was evidenced in the SEM photos of these films in Section 3.4.3. The bipolar pulsed DC run produced a film with lower refractive index which suggests that RF sputtering produces higher density films.

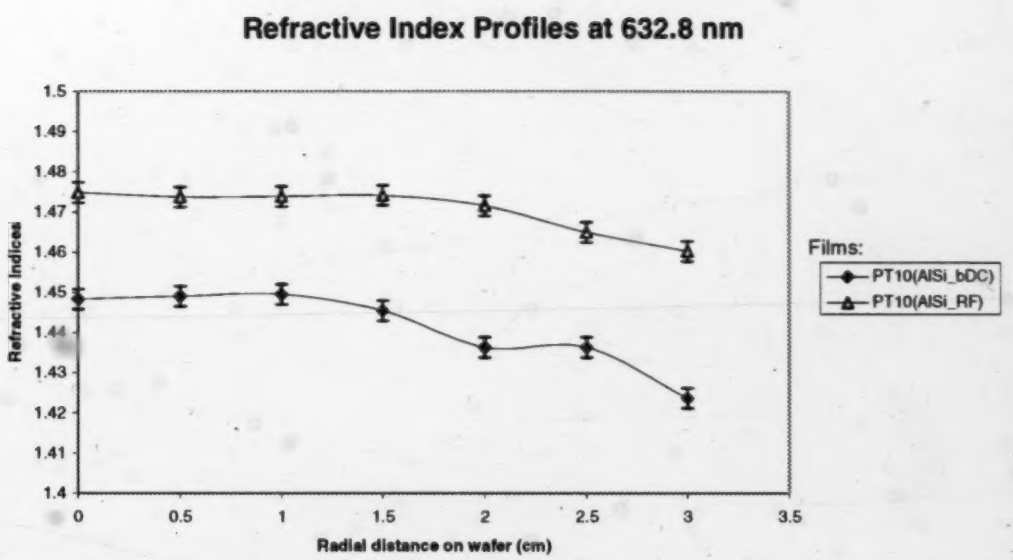

Figure 3.26 Refractive index profiles for the undoped glass films sputtered from conductive alumino-silicate powder pressed targets

Figures 3.27 and 3.28 show the refractive index profiles for the erbium-doped films at 632.8 and 1550 nm. The profiles generally decrease from centre to edge, as well; although PT10(ErAlSi_bDC)'s profile rises before it falls. I cannot account for this; although it may suggest that there is some sort of competition occurring between the index-increasing effects observed with the 1% and 3% Er-doped films and the possibly density-dependent effects observed for the un-doped films. As with the undoped glass, for a given set of run conditions, the RF-deposited films have a higher optical density.

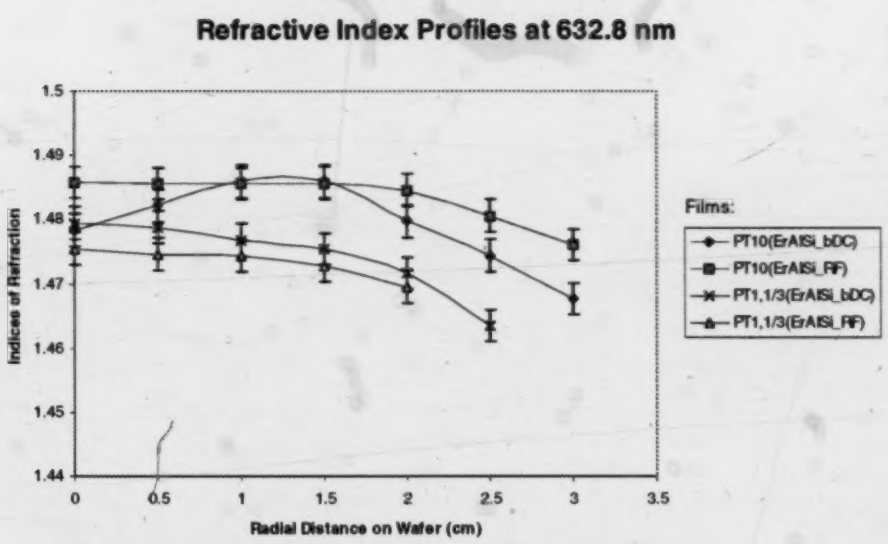

Figure 3.27 Refractive index profiles at 632.8 nm for Er-doped glass films sputtered from metallic alumino-silicate powder pressed targets

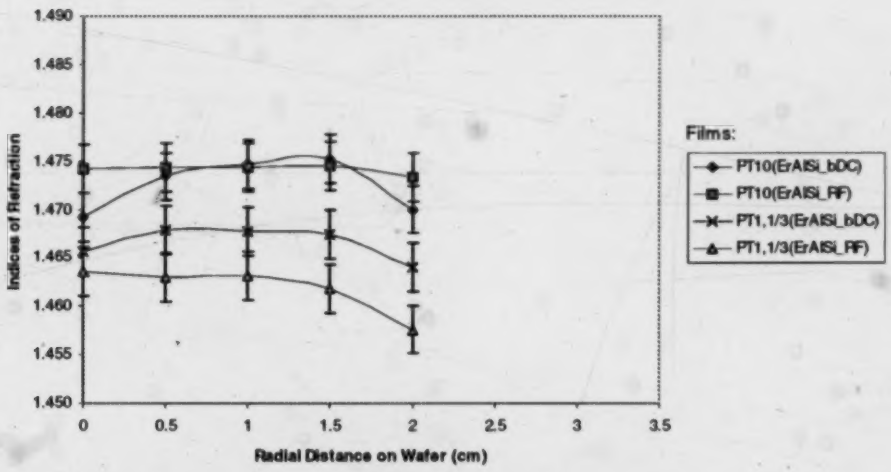

Figure 3.28 Refractive index profiles at 1550 nm for Er-doped glass films sputtered from metallic alumino-silicate powder pressed targets

3.7.4 Summary From Refractive Index Measurements:

The erbium-doped bulk glass targets had average indices in the upper 1.5's to 1.6's; whereas the powder target films were near 1.47. Pressure has the most dominant effect on refractive index. For the 1 and 3% erbium-doped glass, lower pressure runs result in low index films. For quartz, this effect is reversed, and low deposition pressure results in higher index films. Throw length does not seem to have as important a role.

The most interesting observation was that the index of refraction of the films sputtered from bulk glass targets increased in value from the centre to edge of the wafer. This seemed counter-intuitive and was different than the phenomena observed for the other films. For instance, the sputtered-quartz films' index profiles were fairly flat, and the powder target film deposited films' profiles generally decreased from centre to edge. This behaviour was so perplexing that the entire next chapter was dedicated to trying to discover the reason behind it.

Chapter 4.

INVESTIGATION INTO RADIAL REFRACTIVE INDEX INCREASE IN ERBIUM-DOPED SPUTTERED FILMS

4.1 Introduction:

In Chapter 3 a curious phenomenon was observed. The refractive index of the 1% and 3% erbium-doped bulk glass films increased from the centre to the edge of the silicon substrates. This behaviour was counterintuitive since sputtered films should have the highest density in the centre where the vertical impinging flux is most energetic. Sputtering theory describes how this would cause the films to pack highest in this region, causing a tighter film microstructure and higher refractive index.[28]

Sputtered quartz and powder target films exhibit more intuitive refractive index trends. The quartz-sputtered films were reasonably uniform if not slightly decreasing across the wafer surface, and those of the undoped powder target films decreased noticeably from centre to edge. It is possible that the latter behaviour was related to density since those films possess quite an open microstructure whose density is highly-dependent on the incident flux angle.

I hypothesized that erbium-doping might have been the cause of the index increase. It was observed, however, that with the exception of PT10(ErAlSi_bDC), the indices for the erbium-doped powder target films actually decreased over 3 cm, as well, which suggests that erbium, by itself, was probably not the main reason for the increasing index trends. Later in this chapter it will be shown that not only erbium, but the entire complex mixture of dopants in the bulk glass films, play a role in the refractive index increase.

Inhomogeneity in chemical and basic optical properties does not bode well in terms of device performance. Clearly, film chemistry and properties should reflect those of the properly-designed, optically active target. This chapter describes attempts to diagnose the source of the refractive index increase. The film properties investigated are radial variations in density and composition from wafer centre to edge.

It was hypothesized that the density might be varying despite the observation that the erbium-doped bulk-glass films lacked much visible microstructure unless they were deposited at an extremely sharp angle. Another hypothesis was that film chemistry could have changed across the wafer surfaces. In order to investigate this idea, quantitative composition analysis was performed on film PT00(3%) using a wavelength-dispersive electron microprobe. The results are

presented in Section 4.4 and confirm that a radial change in film composition does, indeed, occur.

4.2 Film Density Investigation:

4.2.1 Density Measurements:

In this section, film density profiles are plotted for three particular films from Chapter 3. Each film had to be re-deposited in order to make density measurements. The density-measurement procedure is described in the following paragraphs.

Density-Determination Procedure:

First, a silicon wafer was pre-coated with a thin CVD oxide adhesion layer, roughly 100 nm thick. The wafers were then diced in a computer-controlled, the Micro Automation Model 1100 Micro Dicing Saw. The saw was a diamond-bladed wafer saw with 0.001 cm precision. Three of these die were then individually packaged in sealed plastic containers and transported to Analytical Services on campus where they were weighed on a Mettler UMT2 Microbalance to a precision of 0.1 μg. The operator wore a mask to prevent breath vapour from getting on the films and interfering with the measurements.

Immediately after this, the three samples were returned from Analytical Services and placed inside the sputtering system on top of the sample holder. The inside edge of the first die was positioned at the mid-line of the sample holder, and the pieces were lined up directly adjacent to one another such that the outside of the third bit extended out 3 cm from the centre. The appropriate experimental conditions were then set up, and the sputtering run was engaged. After the run finished, the film-coated bits were returned to Analytical Services where they were re-weighed. The samples' thickness and refractive indices were then measured with the prism coupler by orienting the coupling spot at the centre of each die. By doing this, the thickness and refractive index measurements were made to correspond to positions r = 0.5, 1.5, 2.5 cm on the surface of the wafer.

Density, in g/cm^3, was calculated from the simple formula, $\rho = {}^{\Delta m}/A\, t_{ave}$, where Δm was the difference in the mass measurements from the Mettler Microbalance, A = 1.0 cm^2, and t_{ave} was the thickness measurement taken from the middle of the bit. Since the bits were only 1.0 cm long, it was assumed that the film thickness variations across the bits was linear. As such, t_{ave}, measured in the centre of each piece should be a fairly good representation of the average thickness of that piece.

Target Used:	**Film:**
Quartz:	PT01(QZ_dens)
Er-Doped Bulk Glass	PT10(3%_dens)
Er 3% Metallic: Powder	PT1,1/3(ErAlSi_bDC_dens)

Table 4.1 Films chosen for Chapter 4 density assessment.

The results of this experiment are graphed in Figure 4.1. Error bars were generated using Equation 4.1 and sample data from the graph.

$$\delta\rho = \rho\left[\left({}^{\delta(\Delta m)}/_{\Delta m}\right)^2 + \left({}^{\delta(\Delta A)}/_{\Delta A}\right)^2 + \left({}^{\delta(t_{ave})}/_{tave}\right)^2\right]^{1/2} \qquad (4.1)$$

Some variable values for the quartz run were ρ = 2.30 g/mol, Δm = 0.6314 mg, $\delta\Delta m \cong$ 0.0004 mg, A = 1.0 cm^2, δA = 0.002 cm^2, t_{ave} = 27.4 x 10^{-5} cm, and δt_{ave} = 2.0 x10^{-5} cm. These values resulted in a density uncertainty of approximately 0.2 g/cm^3 which, unfortunately, turned out to be larger in magnitude than any density variation observed on the graph. In other words, these measurements were somewhat inconclusive. Nonetheless, they suggested that, in all likelihood, very little film density variation occurred and that density variation was probably not the source of the rising indices.

Even though the data did not reveal any evidence of density change from film centre to edge, it did provide a relative comparison of the three films' densities. It showed, for instance, that PT10(3%_dens) had the highest density followed by PT1,1/3(ErAlSi_bDC_dens) and then PT01(QZ_dens). Their relative positions on the graph are proportional to the number of dopant elements in each film. This ranking followed the same trend as the refractive indices, so it can be

surmised that the lower the dopant concentration, the lower the density of the material and the lower the refractive index.

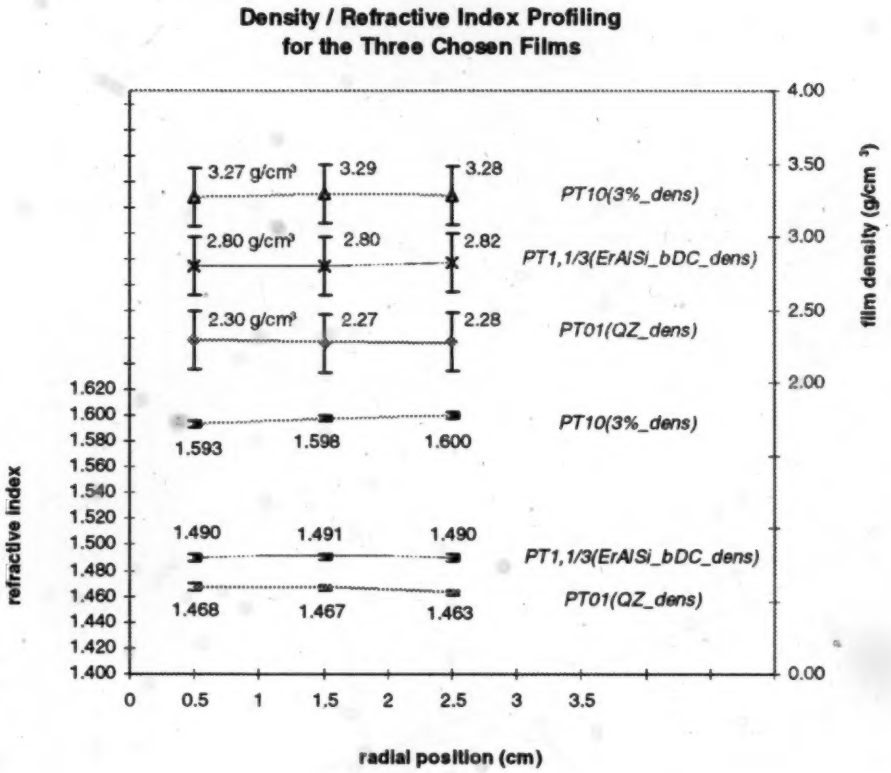

Figure 4.1 Film density/refractive index correlation curves for the three chosen films.

4.2.2 Microstructure:

The preceding numerical study did not yield any major conclusions except that the radial film density variation was probably very minor if it occurred at all. In this section of the thesis, the goal was to use a scanning electron microscope to determine if any variation in film microstructure could be observed in the centre versus the edge of the films. It was anticipated that this would be a difficult assessment to make, but it was attempted anyway. The films investigated here were PT11(QZ), PT00(3%), PT10(AlSi_bDC), and PT10(AlSi_RF) - a reasonably broad sampling of the materials used in this thesis. As it turned out, no variation in

microstructure could be determined using this technique, so none of the photographs are included here.

4.3 Stoichiometry Variation:

Film PT00(3%) Quantitative Stoichiometry Results:

In this section the chemical composition of the 3% erbium-doped bulk glass target and Film PT00(3%) are discussed. This film was chosen because it exhibited a pronounced radial change in refractive index. Using a wavelength dispersive electron microprobe, clear indications were obtained that surface chemistry changed across the surface of film PT00(3%)_thick. It was found that there is a definite compositional deviation both between the source and film and across the film surface from centre to edge.

Microprobe Testing Procedure:

The operator took twenty separate readings from each of three samples - a chunk of 3% bulk glass target for reference, a cleaved section from the centre of film PT00(3%), and a section from the edge. The beam was stepped approximately 10 μm between each measurement and the results were averaged over the set of 20 data points.

The depth of penetration of the electron beam was approximately 8 μm. Therefore, in order for film PT00(3%) to be studied it had to be re-deposited so that there would be at least 8 μm of film at r = 3.0 cm on the wafer. Based on the observation that the film thickness dropped about 50% over this distance, roughly twice that amount of material was needed at the centre. Consequently, sputtering was performed for 53 hours, and the resulting film thickness was 19 μm at the centre and 9 μm at the edge.

Quantitative stoichiometric analyses were performed on two separate groups of samples on two separate occasions using the University of Alberta, Department of Earth and Atmospheric Science's JEOL 8900 Electron Microprobe. The first data set indicated an interesting result that was later confirmed with the second set of measurements.

Results:

The following figures show the microprobe spectra from samples of the target, the centre of the wafer, and the edge of the wafer. Unfortunately, several of the data labels are obscured by the gray shading on the spectral plot. The statistics used for generating error bars in Figure 4.3 are described in Appendix C.

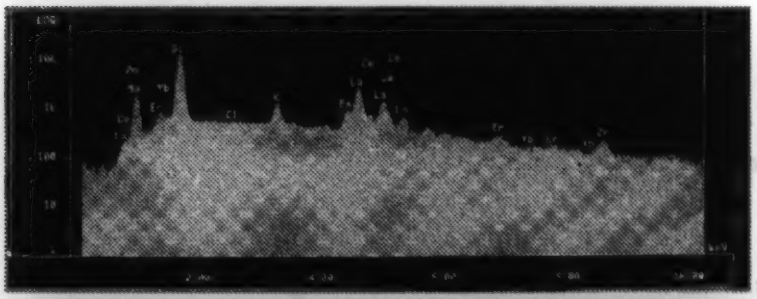

target material

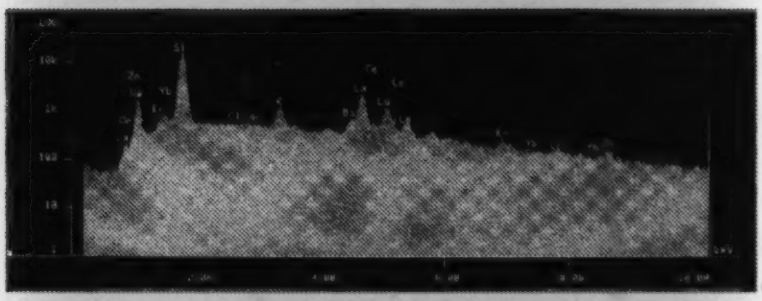

centre of wafer

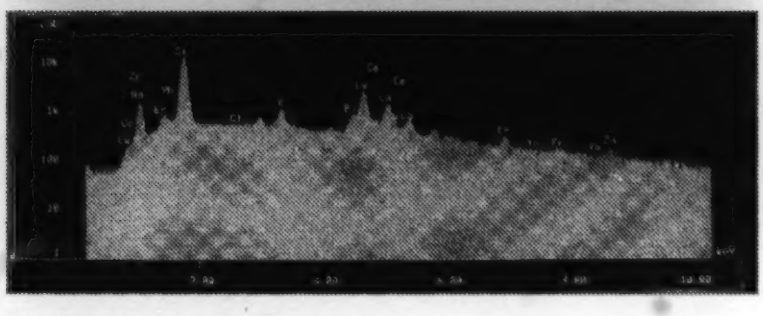

edge of wafer

Beam Energy: 15 kV
Current: 1.503e-08 A
Probe Diameter: 5 μm

Figure 4.2 Microprobe spectra and experimental conditions for the stoichiometric investigation.

The microprobe accounted for all the elements listed in the MSDS for this glass except lithium and boron because they were too light to be detected. It is a reasonable assumption that

B and Li comprise the "missing" data. Oxygen weight percentages were inferred. The weight percentage results from the quantitative analysis are summarized in Tables 4.2 and 4.3.

	O	Si	La	Na	Ba	Er	Zn	K	Ce	Cl *impurity*	totals:	missing:
Source:	33.0	21.5	23.4	7.3	4.7	2.8	2.4	1.7	0.1	0.003	96.9	3.1
Centre:	35.5	25.3	19.0	6.1	3.1	2.7	1.1	1.5	0.1	0.003	94.4	5.6
Edge:	33.0	21.7	24.8	6.6	4.6	3.0	1.5	1.5	0.2	0.001	96.8	3.2

Table 4.2 Weight percentage results from the microprobe spectra.

	SiO_2	La_2O_3	Na_2O	BaO	Er_2O_3	ZnO	K_2O	CeO_2
Source:	1	0.60	0.21	0.11	0.070	0.066	0.044	0.0037
Centre:	1	0.41	0.15	0.064	0.057	0.026	0.034	0.0025
Edge:	1	0.63	0.19	0.11	0.074	0.039	0.038	0.0057

Table 4.3 Stoichiometic summary for the oxides detected. (Normalized to the most common oxide)

The graphs in Figure 4.3 show differences in elemental concentration for *the source versus centre of film* and *source versus edge of film.* The "missing data" was incorporated into the graphs by averaging the atomic weights of lithium and boron to come up with a "missing" single elemental weight value of 8.87 g/mol. This approximated pseudo-element is the first data point on each of the graphs.

The upward trend in Figure 4.2 (a) indicates that, with respect to the bulk glass source, there is an excess of lighter elements and a depletion of heavier elements at the centre of the film. The relatively flat to decreasing trend in Figure 4.2 (b) indicates that the film chemistry is much closer to bulk at the wafer edge. Because the graph dips below the horizontal axis at large atomic mass it shows, in fact, that there is an excess of heavy elements there. The trends observed for oxygen, silicon, and lanthanum are most important since they comprise the bulk of the film.

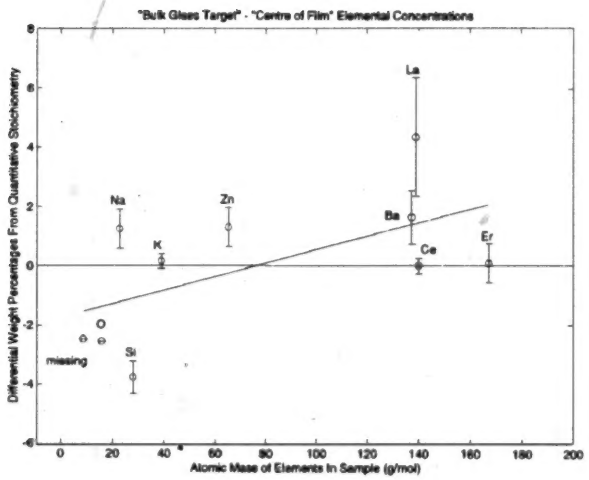

(a)

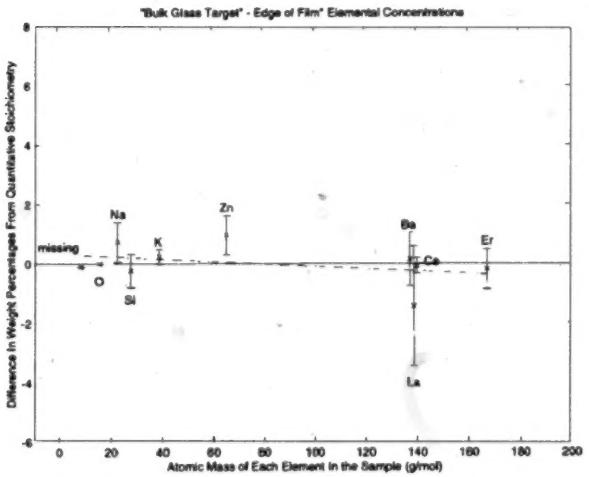

(b)

Figure 4.3

(a) Weight percentage concentration difference between glass target and film centre

(b) Weight percentage concentration difference between glass target and film edge

Elemental concentration differentials plotted with respect to atomic mass of the elements in the samples. The linear trends indicate that the concentration of heavier elements (specifically lanthanum is lower in the centre of the film than at the edge and that the concentration of lighter elements (specifically, silicon) is accentuated in the centre. Also, it shows that the film chemistry more closely resembles the bulk glass sputter target at the edge of the film.

This result seems to contradict the momentum considerations which suggest that heavier elements will be scattered less in a sputtering environment. It is possible that some other phenomenon occurred during or after deposition that interfered with expected elemental distribution.

One proposed explanation was that the heavier oxides evaporated off more readily from the more energetically-bombarded centre region. This theory is unlikely, though, because it turns out that lanthanum oxide has a boiling point of 4200°C while a lighter oxide like sodium oxide, for instance, has a boiling point of 657°C.[61]

Another possible explanation was that the lighter elements were ejected from the target in a more normal fashion while the heavier elements deflected in a broader distribution. For example, it is possible that the lighter elements like silicon or sodium came off with a tighter probability distribution, for instance like a *cosine*^{8}, and that the heavy elements may have come off with a less narrow, *cosine*^{1}-like, distribution, causing the atoms to distribute more broadly. Example thickness profiles for such heavy and light element distributions are shown in Figure 4.4. An argument against such behaviour is that geometrical factors like this would be amplified in the long-throw cases - an effect which was not observed in the data.

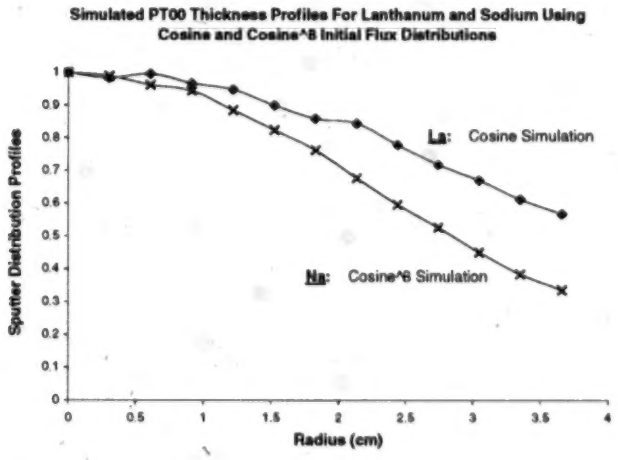

Figure 4.4 Comparison of simulated thickness profiles for La and Na under PT00 conditions. A cosine initial flux distribution is assumed for the heavier element (La), and a sharper cosine^8 distribution is used for the lighter element, sodium.

The last hypothesis I had was that the film may have been re-sputtered by energetic neutrals or negatively-charged ions during deposition. The resputtered particles could have caused lanthanum to be preferentially depleted in the centre of the film as compared to the target and caused silicon levels to be accentuated. It is not obvious why the elements to redistribute in this manner, however.

Assessment:

A correlation has been made between observed refractive increase and variation in film chemistry. This is a major observation in this thesis. It shows not only that the composition of the film differs from the source but that the film chemistry, itself, is radially inhomogeneous. This property may affect the spontaneous emission properties and metastable state lifetimes. It leads me to believe, as well, that I should have tested emission in film samples taken from the edge of the wafer rather than from the centre which I had done to maximize film thickness. It is possible that their improved representation of the source chemistry would have improved the optical properties of the films. A reasonable inference is that material redistribution may have been the result of a resputtering phenomenon.

4.4 Films Deposited on Rotating Substrates:

Based on the previous results, I decided to test an idea. I adjusted the substrate tray so that it could continually rotate back and forth by about 80° under the sputter flux. It was hoped that this would accomplish two goals. Firstly, the film thickness uniformity would be improved on the rotational axis. Secondly, it would show whether this technique could promote greater refractive index uniformity.

The films chosen to be redone for this experiment were PT00(3%) and PT11(3%). It was anticipated that the deposition efficiency would be very low for these runs because of the rotating substrate tray, so the deposition times were increased to 27.5 and 62.75 hours, respectively. The results are shown in Figure 4.6. The film names have been appended with "_rot" to indicate that they were performed on rotating substrates and "in plane" and "out of plane" indicating whether the profiling was done in or out of the plane of rotation.

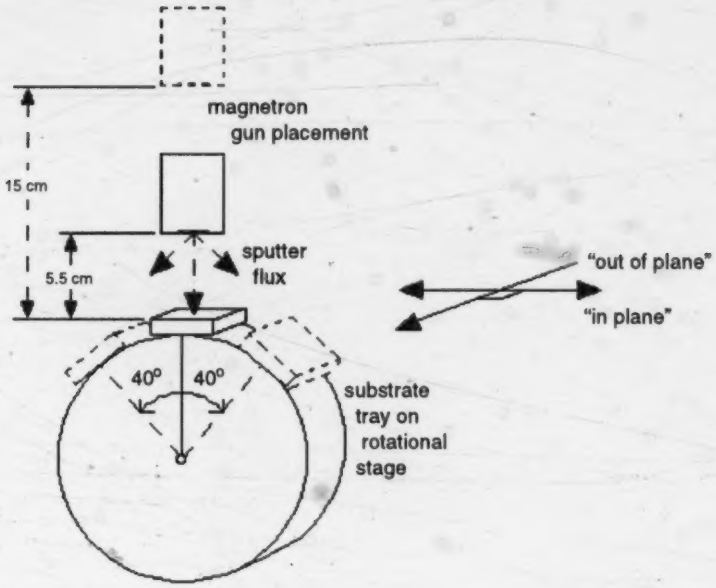

Figure 4.5 Rotating substrate tray assembly.

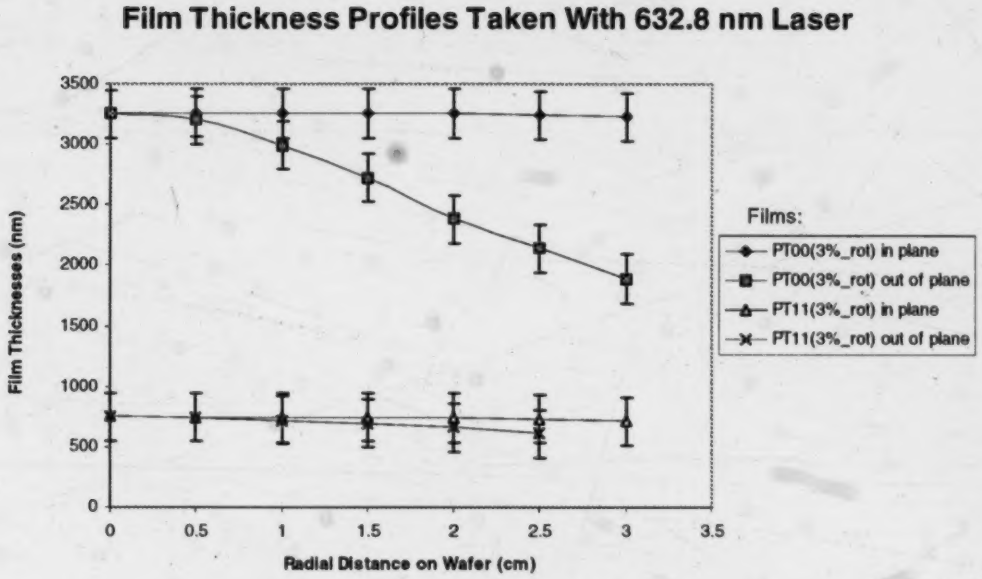

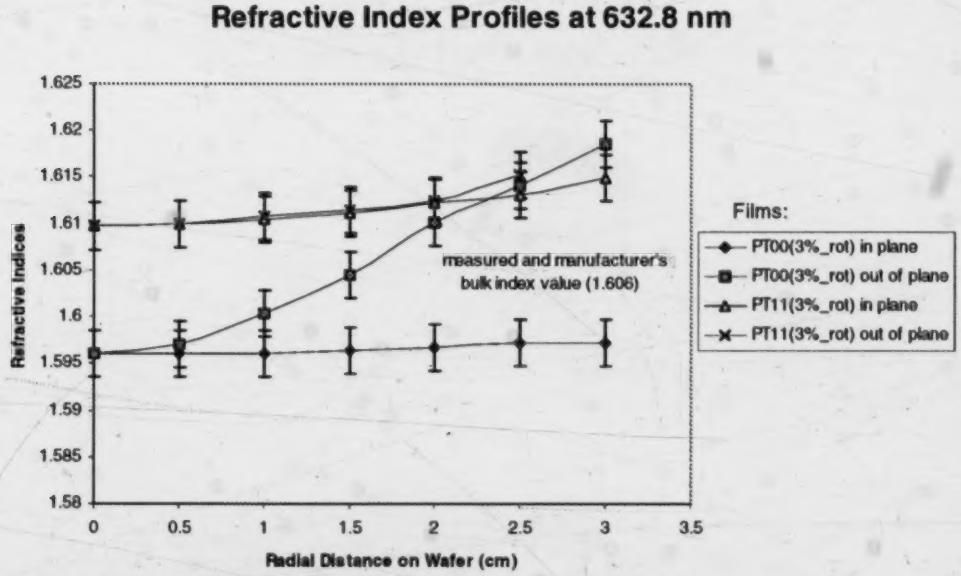

Figure 4.6 Thickness and refractive index profiles *on* and *off-axis* for films PT00(3%) and PT11(3%) deposited onto a continually sweeping substrate that subtends an 80° angle about the midline of the wafer.

The key observation here is that the films' refractive index profiles were considerably more uniform in the plane of rotation than out of plane. The indices still rose from centre to edge to some degree, but the problem was minimized on the rotational axis. It was also observed that the films have quite a uniform thickness profile along their rotational axes and are quite non-uniform off axis, the deposition rates were very low. These results confirmed my hypothesis.

I noted, as well, that there are also some interesting similarities between the off-axis profiles and some of the stationary substrate runs from before. For example, with Film PT00(3%_rot) off-axis there is a 41.9% decrease in film thickness over the 3 cm wafer and 1.9% increase in refractive index. In the preceding runs, PT01(3%) was seen to exhibit a 40.7% decrease in film thickness and an increase of 1.5% in refractive index. This symmetry in results could be due to similarities in deposition conditions. Both runs were performed at low pressure, and the average throw lengths were reasonably long. The average indices of refraction for PT11(3%_rot) off-axis run are also very similar to PT11(3%). On average, the indices differ by only 0.005 over 2 cm.

Assessment:

It can be concluded that this experiment was a success. It showed that both film thickness and refractive index uniformity can be improved in one direction on a silicon wafer substrate if the wafer is rotated back and forth under the sputter flux during deposition. The results suggest, as well, that it might be advantageous to position the substrates on a platform with double-axis, planetary movement. The thickness and refractive index profiles could be improved in both directions.

Chapter 5:

INVESTIGATION INTO LIGHT ABSORPTION AND SPONTANEOUS EMISSION IN BULK GLASS AND FILMS

5.1 Introduction:

So far in this thesis, several material issues have been discussed. These have led to an interesting investigation into refractive index and compositional variation across a film surface. The primary motivation for studying erbium-doped glass, however, is to fabricate optically active films, ie. To produce films which absorb near infrared pump light near 980 nm and spontaneously re-emit in the far infrared in the neighborhood of 1540 to 1550 nm.

In this chapter, the light absorption and spontaneous emission properties of the bulk glass targets, film slabs, and patterned waveguides will be presented. Some films were tube furnace annealed for 5 minutes at 300°C or rapid thermal annealed for 30 seconds at 700°C to see if this improved their optical properties. In addition, some films were deposited onto heated substrates during deposition. All the films to be discussed in this chapter are listed in Table 5.1 along with any special annealing or heating conditions associated with them.

As mentioned in Chapter 1, I originally wanted to avoid having to pattern waveguides into the films. This is an involved process that was not intended to be the point of my research. It was hoped, instead, that the active optical properties of the basic film slabs could be tested. One particular slab did, in fact, provide some useful spontaneous emission measurements, but it was quickly decided that the losses in the waveguides and optical test system were far too high to ensure future success. As a result, ridge waveguides were patterned into all the films to minimize the amount that the light diverged.

It was also hoped that ytterbium co-doped films could be examined, but based on some preliminary investigations and time constraints it was decided that the 1% Er, Yb co-doped glass films would not be studied here. The problem was that some ytterbium-doped waveguiding test films exhibited extremely high losses, possibly, due to excessive pump absorption.

	Film Name	Deposition Method	Target Used	Average Film Thickness (μm)	Cladding Thickness (μm)	Special Fabrication Conditions
1.	PT00 (3%)_thick	RF	3% Er-Doped Glass	15	5.0	extra thick film (made for microprobe tests)
2.	PT00 (3%)_thick_ann	RF		15	5.0	# 1 furnace-annealed for 5 min. at 300° C
3.	PT00 (3%)	RF		9.0	5.0	
4.	PT00 (3%)_RTA	RF		9.0	5.0	# 3 RTA'd for 30 sec. at 700° C
5.	PT00 (3%)_heat	RF		4.0	5.0	# 3 deposited onto heated substrate
6.	PT00 (3%)_heat_RTA	RF		4.0	5.0	# 5 RTA'd for 30 sec. at 700° C
7.	PT01 (3%)	RF		2.0	5.0	
8.	PT10 (3%)	RF		8.0	5.0	
9.	PT11 (3%)	RF		0.95	5.0	
10.	PT10 (ErAlSi_RF)	RF	Er-doped Alumino-Silicate Compressed Conductive Powder	4.5	5.0	
11.	PT10 (ErAlSi_RF)_ann	RF		4.5	5.0	# 10 furnace-annealed for 5 min. at 300° C
12.	PT1,1/3 (ErAlSi_RF)	RF		3.4	5.0	
13.	PT1,1/3 (ErAlSi_RF)_ann	RF		3.4	5.0	# 12 furnace-annealed for 5 min. at 300° C
14.	PT10 (ErAlSi_bDC)	bipolar		4.5	5.0	
15.	PT10 (ErAlSi_bDC)_ann	bipolar		4.5	5.0	# 14 furnace-annealed for 5 min. at 300° C
16.	PT10 (ErAlSi_bDC)_RTA	bipolar		4.5	5.0	# 14 RTA'd for 30 sec. at 700° C
17.	PT10 (ErAlSi_bDC)_heat	bipolar		4.5	5.0	# 14 deposited onto heated substrate
18.	PT1,1/3 (ErAlSi_bDC)	bipolar		3.7	5.0	
19.	PT1,1/3 (ErAlSi_bDC)_ann	bipolar		3.7	5.0	# 18 furnace-annealed for 5 min. at 300° C

Table 5.1: Summary table of films studied in this chapter.

5.2 Experimental Tools and Methodologies:

5.2.1 Pump Absorption and Spontaneous Emission:

There were two techniques used to check for pump absorption and two techniques used to check for spontaneous emission in this thesis. The first absorption-measuring technique was a combination of reflection and transmission spectraphotometry. In a spectraphotometer, a beam of light is directed at and illuminates a sample under investigation. The beam is scanned through a range of wavelengths in order to obtain a transmission or reflection spectrum off the sample. The peaks in the spectrum indicate where the characteristic absorption peaks lie.

In this experiment it was hoped that an absorption peak near 980 nm could be seen in the optically active films. Two spectraphotometers were used - a Pharmacia UV/Visible and Nicolet Magna 750 FTIR, both located at the Spectral Services Department at the University of Alberta. The first was used to obtain transmission spectra of the bulk glass targets, and the latter was used

to perform reflectance scans. Unfortunately, repeated measurements were not possible since 980 nm was below the lower limit of the detector and could not consistently be reached.

The second technique for measuring light absorption required a fibre optic test bench (refer to Figure 5.1). This system was located at TR Labs in Edmonton and will be discussed more thoroughly in Section 5.2.2. Light absorption and spontaneous emission were both measured with this system. Spontaneous emission was also measured from one of the bulk glass targets using a Bomen DA8 Infrared Interferometer located in the Physics Department at Simon Fraser University.

5.2.2 Optical Test Bench:

Description:

The essential premise behind the set-up shown in Figure 5.1 was to pump glass waveguiding films with a (roughly) 980 nm laser beam and observe the output spectra near 1550 nm. This equipment was already set up at TR Labs but was modified for these experiments. The laser system consisted of two 488 nm argon laser sources that double-pump a Ti-Sapphire crystal laser. The infrared output of the Ti-Sapphire laser could be varied from below 900 nm to 988 nm and was steered in free space by multiple-axis-positioning mirrors. Along the free-space path of this laser beam, a chopper could be inserted. By monitoring the chopped output of an erbium-doped waveguide on an oscilloscope, metastable lifetimes could be measured provided they were long enough in duration for the scope to detect.

This free-space beam was coupled into a 7 μm core single mode fibre using a 20x microscope lens. This fibre was actually one branch of a wavelength division multiplexer. On the figure it can be seen that the other branch could be used for a number of other purposes. For instance, by using connection (c), a red HeNe source can be coupled into the waveguide in order to light it up during the alignment phase. With the tracer and pump beams aligned in the WDM, it was assumed that if one was lined-up then the other would be, as well. This is a very handy technique to align an optical system in which the beam is invisible. Without this tracer beam it would have been extremely difficult to determine whether or not light was actually traveling through the cladding, the doped glass, or in free space above the films.

By changing the WDM to connection (d), backscattered light from the films could also be monitored. The premise behind this was to look for spontaneous emission in the reflected signal in addition to forward throughput through the guide. It was hoped that this would enable high-loss waveguides to be tested even if there was not enough light available at (g) to test forward spontaneous emission. By again changing the WDM to connection point (e), a 1547 nm signal could be coupled into the guide in order to perform stimulated emission tests.

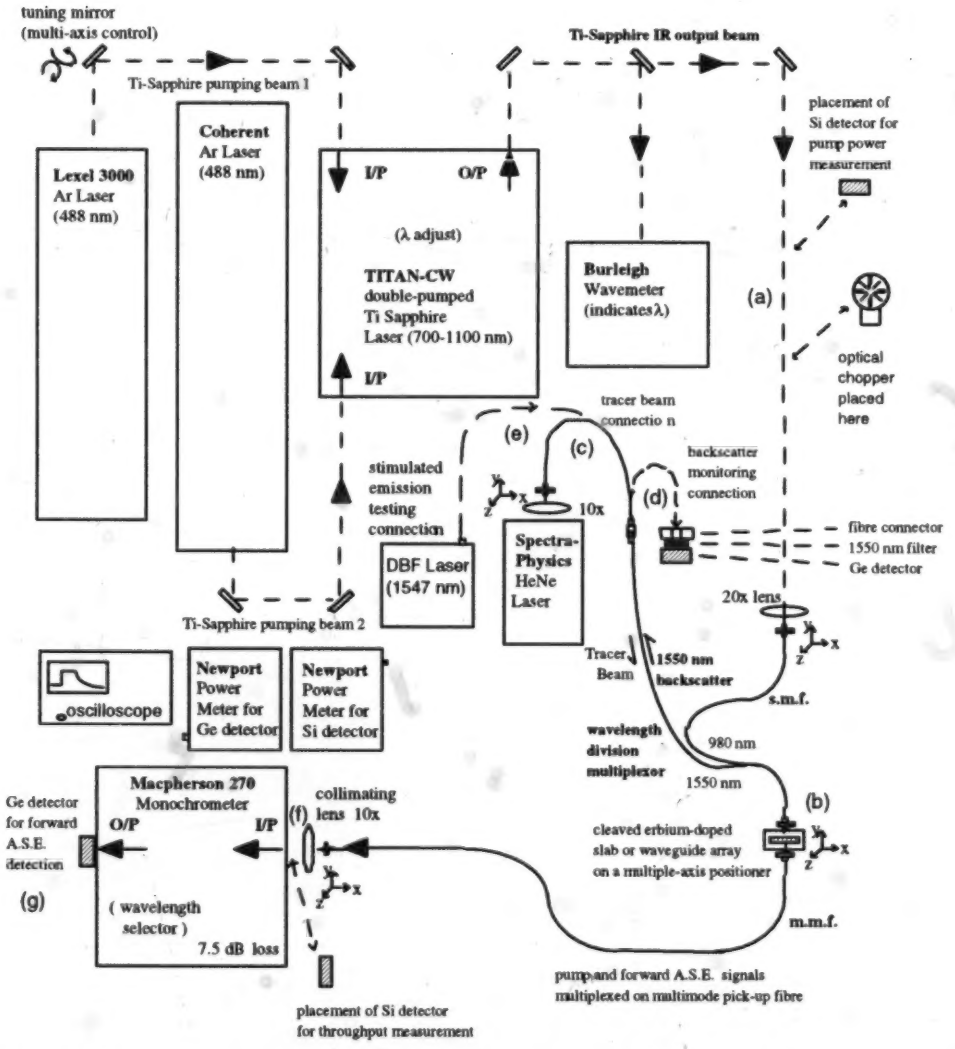

Figure 5.1: Optical bench set-up used to test pump absorption and spontaneous emission.

Each sample of erbium-doped waveguides to be placed on the multi-axis positioner at point (b) was cleaved to a fairly consistent length of 5 +/- 1 mm. The light output from the waveguide was coupled into a 60 μm core multi-mode pick-up fibre which fed into a monochrometer. This device used a movable diffraction grating mechanism to enable the operator to isolate light through a wide range of wavelengths. A germanium detector and Newport power meter were placed at the monochrometer output so that forward spontaneous emission could be monitored.

Data-Taking Methods:

At every major junction in this optical set-up, the light signal had to be optimized in order to maximize power throughput and measurement consistency. In the process, Newport light detectors were used along with silicon and germanium detectors. Silicon detectors were used for the visible and near-infrared light sources and germanium for the far infrared. Fine tuning the fibre optic test bench laser system was a laborious procedure that involved maximizing a large number of degrees of freedom simultaneously. My work during this process was greatly facilitated by the generous help of Madhu Krishnaswamy, who had considerable experience and expertise tuning the system.

Before a waveguide was placed in the optical system, the coupled pump power was maximized at point (b). At 980 nm, this power was usually about 150 mW. A waveguide was then placed onto the multi-axis positioner and the light power was maximized at point (f) by fine tuning the position of the waveguide and multi-mode pick-up fibre. If the power there was at least a few mW at 975 nm then a throughput spectrum was taken at point (g). If the power was less than this, then no scans were taken because the signal would be too weak to be registered through the monochrometer. Low power could have either been due to high absorption or waveguide losses.

The monochrometer was scanned through a range of roughly 1500 to 1600 nm to cover output at the wavelength region of interest. Light absorption and backscattered intensity were monitored as a function of input wavelengths by monitoring the power at points (a), (f), and (d) as a function of λ_{in}. This procedure required that the silicon detector be physically moved from point (a) to point (f) which took some time to do because it required lifting the power cord over top of all the critically aligned components in the optical system.

In order to check the back scattered spontaneous emission, the WDM had to be physically disconnected from the tracer-beam connection at point (c) and re-connected to the power connector at point (d). As such, the tracer-beam connection had to be re-established after almost every measurement was taken to ensure that the beam was still aligned through the guide. These operations took more time and unfortunately increased the potential that the system time would drift or be knocked out of alignment.

5.3 Examples of Some Waveguide Images:

Films From Bulk Glass Targets:

Most of the 3% bulk glass-sputtered waveguides resembled the one shown in Figure 5.2(a) Some sustained considerable surface damage from the etch, however, and were quite non-uniform such as the one shown in Figure 5.2(b). (The mask used had several different waveguide widths.)

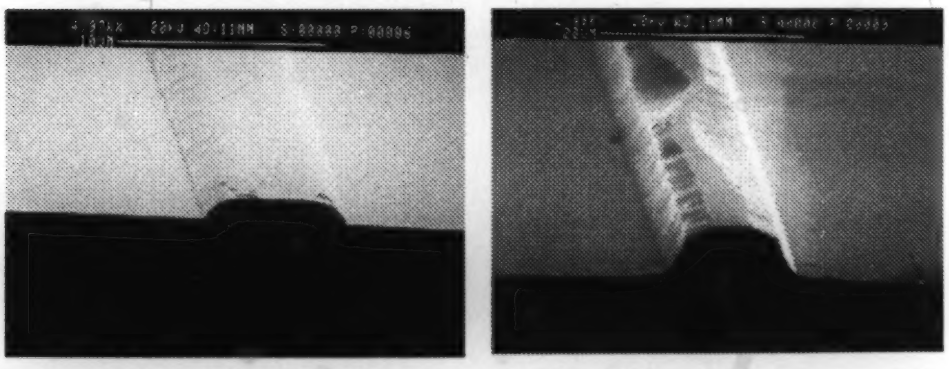

(a) Film PT00(3%): Typical etch profile (b) Film PT10(3%): Highly uneven, rough etch.

Figure 5.2 Sample SEMs of PT00(3%) waveguides.

A typical waveguide from another film, PT10(3%), is shown in Figure 5.3. It etched quite consistently without sustaining much damage. The sidewalls all displayed a concave profile from undercut during the etch. This particular waveguide lit up extremely well with a HeNe tracer beam and provided by far the best light coupling of any of the waveguides. PT10(3%) is the only waveguiding film to undergo stimulated emission testing. A gain of 0.46 dB was measured on a 1550 nm carrier multiplexed through the waveguide. I suspect that this gain was actually just an

artifact of "pump leakage"; however, and did not actually represent real gain. The "pump leakage" phenomenon will be discussed in Section 5.5.3.

Sample SEM micrograph of PT10(3%) waveguide. More sidewall etching is evident here.

Figure 5.3

Films From Powder Targets:

The preceding waveguides had little or no visible microstructure. This is desirable for maximizing light throughput, but this advantage was often offset by poor quality and uneven etching. By contrast, the films sputtered from powder targets all displayed highly columnar glass, but all etched very uniformly with reasonably sharp edges. Figure 5.5 shows typical cross section and perspective images for these films. The particular waveguide shown is PT10(ErAlSi_RF).

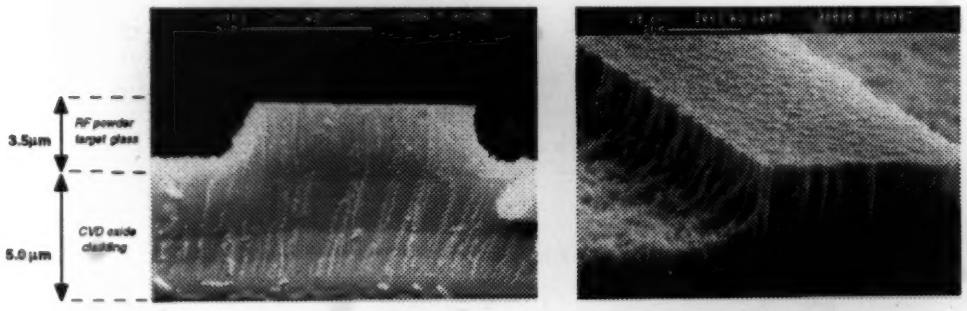

(a) cross sectional view **(b)** perspective view

Figure 5.4 SEM micrograph of PT10(ErAlSi_RF) waveguide. This waveguide looks like all the other films made from powder targets.

5.4 Experimental Results: Light Absorption In Bulk Glass and Films:

5.4.1 Absorption In Bulk Glass Targets *(from spectraphotometry)*

The first property investigated was absorption of 980 nm pump light in the bulk glass targets. Good pump absorption is obviously a very important parameter that is necessary to obtain population inversions at the metastable $I_{13/2}$ state. Furthermore, without optically active starting material, the chance of producing optically active films is probably very slim.

The Pharmacia UV/Visible spectraphotometer was used to obtain transmission spectra of both bulk glass targets from 300 to 1200 nm. Over this wavelength range, this instrument was only equipped to perform transmission scans. The results are shown in Figures 5.5 and 5.6 and are overlaid with the manufacturer's plots. The 1% erbium, ytterbium co-doped sample was 1.09 mm thick while the 3% sample was 1.95 mm thick.

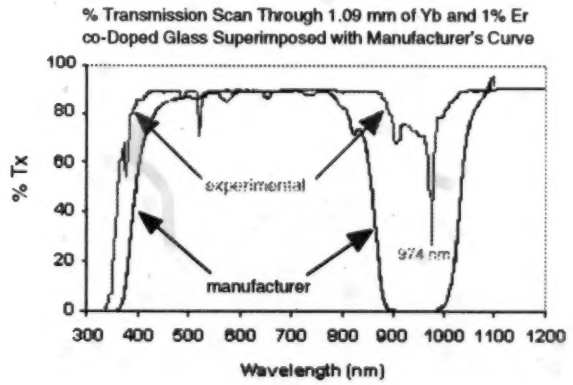

Figure 5.5 Spectral Transmission scan and manufacturer's data for the Er 1%, Yb co-doped target

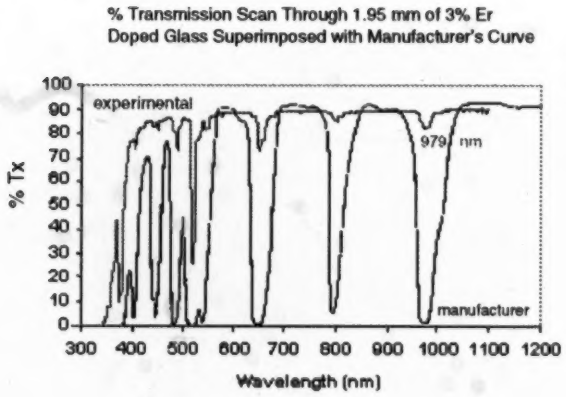

Figure 5.6: Spectral Transmission scan and manufacturer's data for the Er 3%-doped target.

From the figures it is clear that both glasses absorb near 980 nm as hoped. There are several curiosities in the two spectra, however. First of all, the claimed peaks in both of the manufacturer's spectra are considerably broader and deeper than the experimental results would suggest. In particular, the experimental absorption peak for the 3% glass is particularly narrow and shallow compared to the manufacturer's. It is possible that the manufacturer's spectra was obtained from a much thicker sample which would account for the deeper absorption peaks. Unfortunately, the sample thickness data was not available.

Another interesting feature from the spectra was that the main absorption peaks near 980 nm differ by 5 nm for the two glasses. The centre for the 1% glass is at 974 nm and for the 3% glass it is at 979 nm. As expected, the ytterbium-doped material has a much broader and deeper absorption cross section.

5.4.2 Absorption In Film PT00(3%): *(from spectraphotometry)*

Transmission Scans:

Two different spectraphotometers were used to try to determine the film's spectral absorption characteristics. Since silicon is opaque below 1000 nm, the film was deposited onto fused quartz substrates. Transmission scans were first performed on film PT00(3%) using the Pharmacia UV/Vis Spectraphotometer. There was 91% transmission through the quartz blank at

approximately 980 nm and approximately 90% with the film on top. The spectra was flat, however, so no absorption peak could be detected and the plot is not included here.

Reflectance Scans:

I was not confident or satisfied with the previous result. As a results, another means of investigation was attempted - reflectance measurements. These were performed on the quartz slab and film using the Nicolet Magna 750 FTIR Spectraphotometer and the results are shown in Figure 5.7. At 980 nm there is a dip in the reflection spectra of the film. It is not obvious whether this is an absorption peak or whether it is just an artifact of the instrument's poor resolution at this wavelength. For instance, the quartz substrate baseline scan clearly starts to become noisy at near 1030 nm (9700 cm^{-1}) which raises suspicion as to the authenticity of the measurements on the film. In fact, despite repeated attempts, the operator could only perform measurements down to this wavelength on this one particular sample.

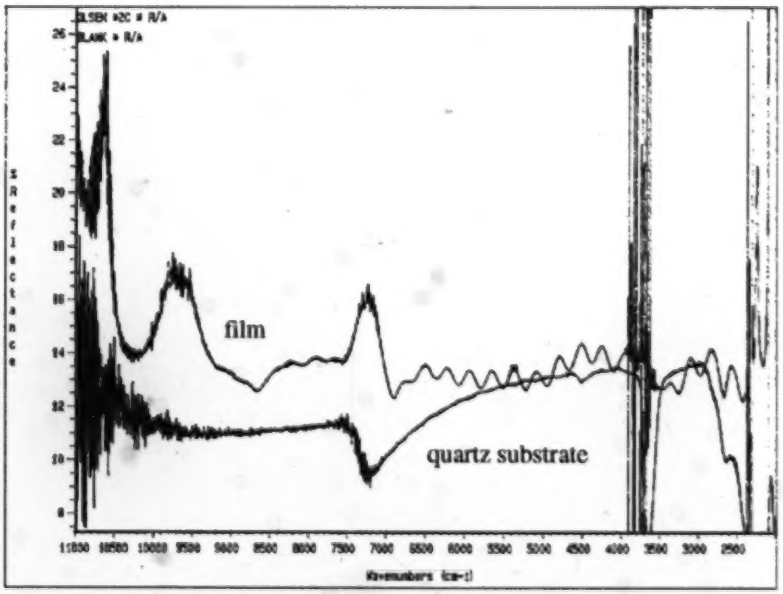

Figure 5.7: Reflection scans of the uncoated quartz substrate as well as film PT00(3%) taken from 11,000 to 2500 cm^{-1}. This corresponds to 909 to 4,000 nm.

I attempted to resolve ambiguity in this data by repeating the reflectance measurements using a Varian spectraphotometer located in the Electrical Engineering Department at the University of Alberta. The device was equipped to perform spectral scans from 200 nm to well above 2000 nm. To do this, the machine automatically switched detectors at 800 nm. Below 800 nm, a highly sensitive silicon detector is used, but above this, a photomultiplier tube took over. It was considerably less sensitive. As a result, there was never enough light reflected from any of the samples' surfaces into the photomultiplier tube to register a signal above 800 nm. This detector cross-over could not be over-ridden by computer control, unfortunately, so this instrument was abandoned.

5.4.3 General Absorption Measurements In All Films: *(using the optical test bench)*

Table 5.2 is a list of observations from the light absorption tests performed with the optical bench. The value, the "dB contrast" was defined as the difference in optical throughput power in the system (in decibels) at wavelengths that were at and far away from the main pumping wavelength. I defined the "main pumping wavelength" as the wavelength for which total system throughput power was lowest, or the point at which the film appeared to absorb most strongly. It was found that this wavelength was usually between 973 to 980 nm for all the films tested. The values were not consistent even for films of the same material, so it is possible that experimental error in measurement may have occurred in measurement or that different fabrication conditions actually alter the main absorption wavelength.

It should be noted here that absolute waveguide loss measurements were not the main concern because this was not the focus of my research. Instead, I concentrated on the dB contrast measurements. Characterizing the individual waveguide losses in dB/cm would not have been a time-efficient exercise for me, especially considering this was not one of my research objectives. In order to do this properly, numerous "cut-back" loss measurements would have to be performed on each waveguide in order to compensate for inconsistent end facet fracture quality and fibre coupling losses.

In order to determine contrast values, throughput measurements were taken above and below the central wavelength. The lower test wavelength was usually 950 nm, and the higher was approximately 985 nm. The higher the contrast value, the stronger the light absorption.

Unfortunately, 985 nm was not much higher than the central wavelength, but this was as high as the system would go.

The overall system losses with these 5 mm waveguides varied from 5.4 to 30.2 dB due to such factors as reflections, misalignments, scattering losses, and absorption. The throughput contrast values ranged from 0 to 3.70 dB for the bulk glass target films and 0 to 4.7 dB for the powder target films. As a figure of merit, 3 dB contrast represents a 50% reduction in light throughput.

Interestingly, the contrast values in Table 5.2 are often higher between the centre wavelength and 985 nm than with 950 nm, a considerably more distant wavelength. I would have expected the lower dB contrast value to have been consistently greater simply because of the increased spread between the wavelengths. I cannot account for this behaviour except to suggest that it is either an artifact of experimental error or that the absorption bands may drop off more sharply above the central wavelength than below in some of the films.

	Film	Test Wavelengths (nm)	Throughput Contrast (dB) Between Indicated λ's	Optical System Backscatter at 1550 nm	Loss at Centre λ (dB)
Films from 3% Erbium-Doped Bulk Glass Targets	PT00(3%)	955 973 985	0.629 2.631	none observed	15.6
	PT00(3%)_RTA	950 978 985	0.539 2.805	none observed	13.3
	PT00(3%)_heat	958 975 985	3.698 3.276	see next figure	30.2
	PT00(3%)_heat_RTA	950 978 985	0.26 0	none observed	9.3
	PT01(3%)	950 975 978	1.817 0.872	none observed	15.3
	PT10(3%)	955 980 985	2.056 1.094	none observed	5.4
	PT11(3%)	950 978 983	1.873 0.499	none observed	17.8
Films from 3% Erbium-Doped Bulk Glass Targets	PT10(ErAlSi_RF)	950 976 990	1.626 1.317	none observed	27.0
	PT1.1/3(ErAlSi_RF)	950 975 985	1.606 1.476	none observed	10.0
	PT10(ErAlSi_bDC)	960 977 985	0.282 0	none observed	23.0
	PT10(ErAlSi_bDC)_RTA	950 979 985	2.911 2.827	none observed	20.0
	PT10(ErAlSi_bDC)_heat	950 975 N/A	4.7 N/A	none observed	19.0
	PT1.1/3(ErAlSi_bDC)	950 968 985	0 1.057	none observed	17.0
	PT1.1/3(ErAlSi_bDC)_RTA	950 978 985	1.928 1.262	none observed	14.0

Table 5.2 Throughput contrast and backscattered spontaneous emission test results.

Films From Bulk Glass Targets:

The essential conclusion that can be drawn from Table 5.2 is that heating the substrate during deposition seems to improve the film's ability to absorb the pump. This is certainly evidenced by the film, PT00(3%)_heat. This film exhibits high contrast values somewhere in the mid 3 dB range both above and below 975 nm. Annealing does not seem to produce the same effect, however. In fact, after rapid thermal annealing, the upper and lower contrast values decrease noticeably to roughly 0 dB, so it would appear to deteriorate pump absorption properties.

I find this observation difficult to believe and suspect that the system probably drifted out of alignment slightly and was not fully re-optimized during successive throughput measurements. For truly accurate absorption measurements to be done, each measurement should be taken with an optimally-tuned system. In Section 5.5.3 annealing was seen to improve the emission characteristics of the films quite noticeably. As a result, I suspect the results here are not accurate absorption characterizations.

Films From Powder Targets:

The dB contrast values for the films from powder targets were of the same order of magnitude as the values from bulk glass target films. Here, however, rapid thermal annealing was actually seen to improve dB contrast, at least for films, PT10(ErAlSi_bDC) and PT1,1/3(ErAlSi_bDC).

Film PT10(ErAlSi_bDC)_heat displayed a 4.7 dB contrast between 975 and 950 nm, which was the highest value observed for any of the films. However, the power throughput at 985 nm was negligible and could not be measured. In other words, the system either absorbed very strongly at this wavelength or went out of alignment.

Assessment:

It is difficult to draw many conclusions from this data except that heating erbium-doped sputtered glass films seems to improve their ability to absorb a pump in the 975 nm range. This confirms what has been printed in the literature on the subject (refer to Chapter 1). Unfortunately, the technique used to assess absorption was inherently flawed, I feel, because the system may not have been equally optimized at different wavelengths and for different individual

readings. Consequently, I will rely more heavily on the spontaneous emission curves in Section 5.5.3 to assess the active optical properties of these films.

5.5 Experimental Results: Spontaneous Emission Testing:

5.5.1 Spontaneous Emission From 3% Erbium-Doped Bulk Glass:

(using Bomen DA8 Infrared Interferometer)

The 3% glass slab was examined using a Bomen DA8 Infrared Interferometer in the Physics Department at Simon Fraser University. A sample was illuminated from above with a 980 nm laser source, and a spectral scan of the reflected light signal was performed. The results are displayed in Figure 5.9 and clearly show a spontaneous emission peak at near 1540 nm.

The incident beam was also chopped with an optical chopper and a decay lifetime of 3.6 ms was observed on an oscilloscope. A representative decay lifetime plot for erbium-doped glass is shown in Figure 5.10. This plot was adopted from an erbium-doped fibre characterization that I performed some time earlier. An identical decay trend was observed for this bulk glass except here τ = 3.6 ms. Since the actual output from the bulk glass measurement is not available, this figure is included for illustration, and the decay time is left in algebraic form.

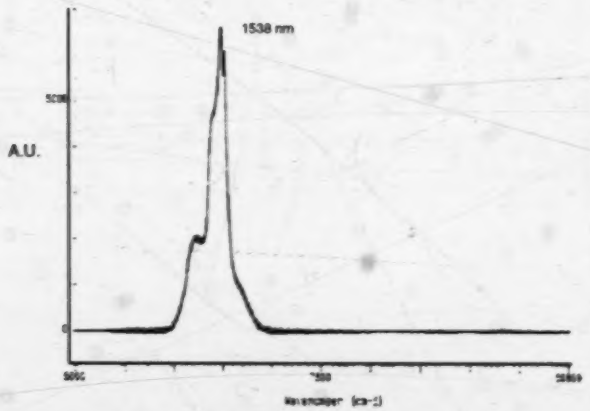

Figure 5.9: Spontaneous emission from 3% erbium-doped glass target. Measurement were performed with a Bomen DA8 Infrared Interferometer at Simon Fraser University.

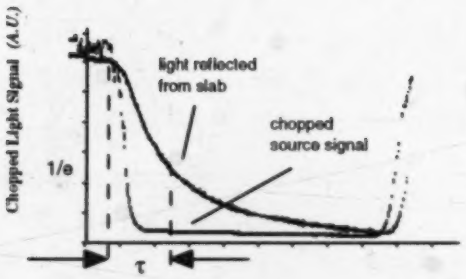

Figure 5.10: Chopped beam and spontaneous emission decay. (decay lifetime τ)

5.5.2 Spontaneous Emission From Unpatterned Film Slabs: *(using optical test bench)*

Several waveguiding film slabs were tested on the optical test bench. The first glass film studied was "PT00(3%)_thick." This film was approximately 10-15 μm thick and was originally fabricated for microprobe analysis. The film depth had to be large enough to accommodate the probe beam penetration. It was aligned in the optical set up and pumped at 979 nm. The signal at the output of the monochrometer was weak, but a spectral plot was taken from 1520 to 1570 nm. The spectrum is plotted in Figure 5.11.

There appears to be a dominant peak at approximately 1540 nm and a sub-peak at 1550 nm. This resembles the expected Stark-split emission peaks of an erbium-doped glass as shown in Figure 1.11. The sample was annealed and re-tested, but the spectrum did not change, so it was not included here. This film was labeled "PT00(3%)_thick_ann" in Table 5.1. No throughout or backscatter tests were performed on this film because this system modification was not set up at the time of these experiments.

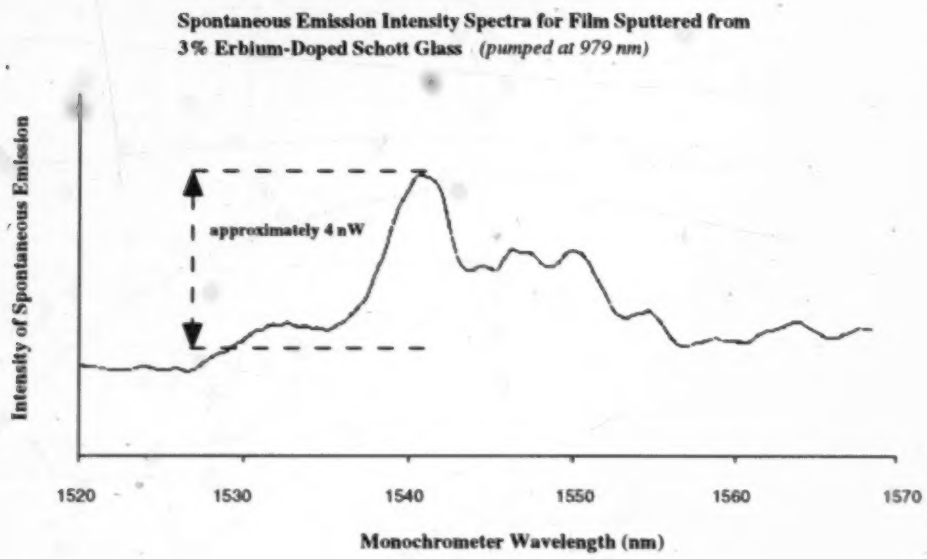

Figure 5.10 Monochrometer output from film PT00(3%)_thick.
The peaks suggest that spontaneous emission is occurring.

Lifetime measurements were taken on the slab, and are shown on the oscilloscope traces in Figure 5.12. Unfortunately, the decay lifetime was too short to be measured. In fact, no decay lifetime value could be measured for *any* of the films studied in this thesis.

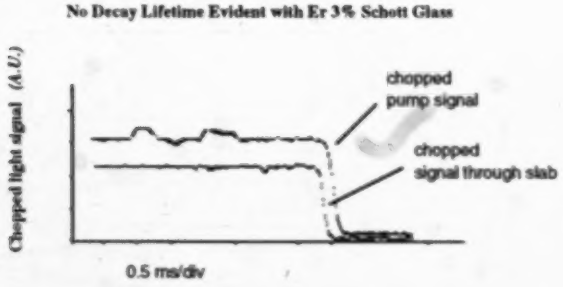

Figure 5.11 Oscilloscope traces of chopped pump beam
and signal through the erbium-doped glass slab.

Films made from the reactively-sputtered powder pressed targets were also investigated, but none of them displayed any forward spontaneous emission or decay lifetimes either before or

after being annealed in the tube furnace. The losses were so high during these tests that it was determined the raised ridge waveguides would be used from here on in.

5.5.3 Spontaneous Emission From Ridge Waveguides: *(using optical test bench)*

In the following section, the major forward spontaneous emission results are presented. Two main pump wavelengths were tested: 974 and 978 nm. In some cases, a 968 nm test wavelength was used, as well. Results were obtained by taking power readings at the output of the monochrometer while it was swept from 1500 to 1580 nm. Some measurements were taken manually and others were generated on a plotter. Only the most impressive results from the films studied are presented here.

All the spectra in the upcoming pages have a dominant peak near 1510 nm. This was not spontaneous emission but an artifact because the peak was also present in the background spectra without the waveguides present. It is possible that the pump somehow leaked through the internal optics of the monochrometer at this wavelength or that this was a harmonic of some element in the optical system. It is of interest to note that at lower pump laser wavelengths the peak shifted to the left.

This unknown origin of this peak was disconcerting, and I began to suspect that all the spontaneous emission peaks near 1530 - 1550 nm may have been mere "artifacts." I cross-checked this as fully as possible, however, by characterizing the background pump spectrum at comparable powers and pump wavelengths without waveguides present in the system. These were overlaid with the appropriate emission spectra and are presented in the following pages. After examining the overlying spectra, I am now quite confident that the peaks observed in the range of 1530 to 1550 nm were actual spontaneous emission.

PT00(3%):

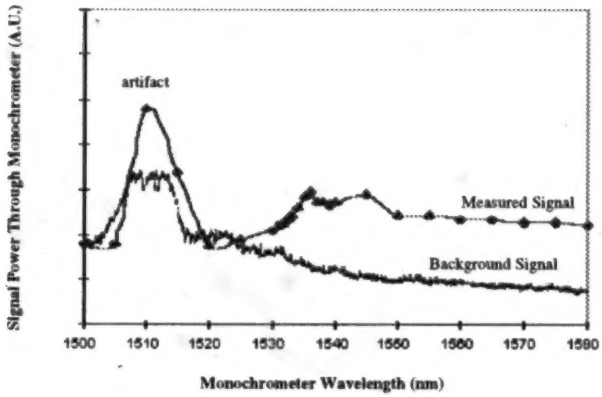

Figure 5.12 Waveguide output spectra from Film PT00(3%) pumped at 974 nm. Spontaneous emission peaks are observed between 1535 and 1545 nm.

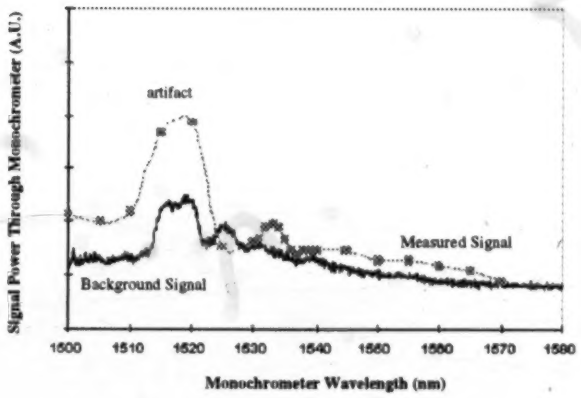

Figure 5.13 Waveguide output spectra from Film PT00(3%) pumped at 978 nm. Spontaneous emission peak observed near 1534 nm.

PT00(3%) RTA:

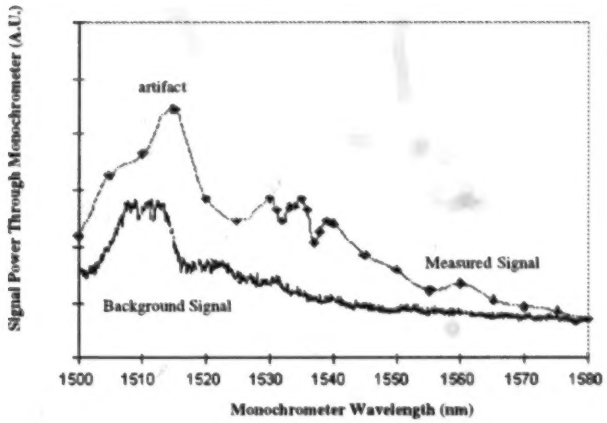

Figure 5.14 Waveguide output spectra from Film PT00(3%)_RTA pumped at 974 nm. Spontaneous emission peaks are observed between 1528 and 1540 nm.

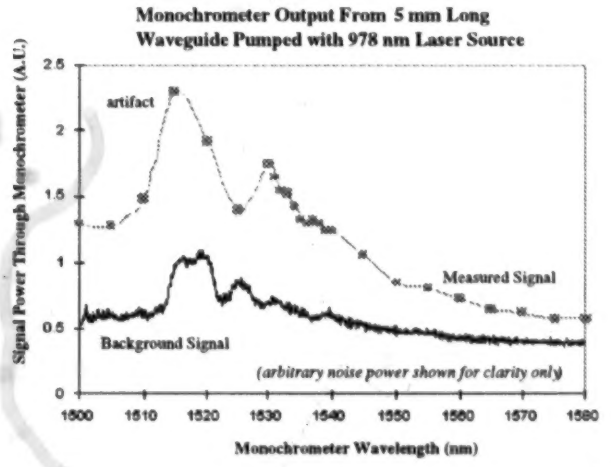

Figure 5.15 Waveguide output spectra from Film PT00(3%)_RTA pumped at 978 nm. Spontaneous emission peak observed near 1534 nm.

PT00(3%)_heat_RTA:

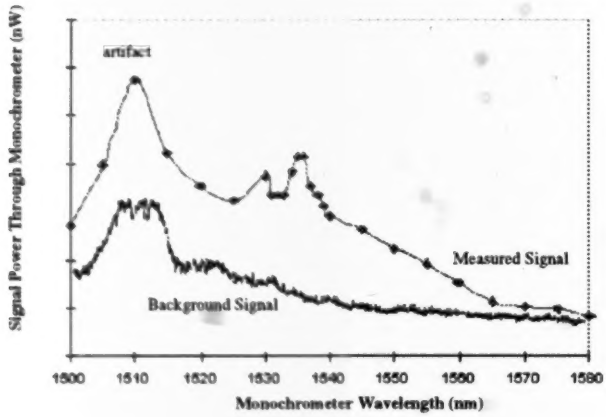

Figure 5.16 Waveguide output spectra from Film PT00(3%)_heat_RTA pumped at 978 nm. Spontaneous emission peak observed near 1534 nm.

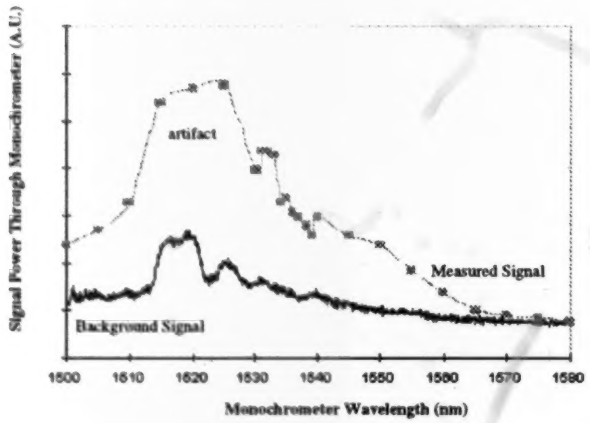

Figure 5.17 Waveguide output spectra from Film PT00(3%) pumped at 978 nm. Spontaneous emission peak observed near 1534 nm.

PT1,1/3(ErAlSi_bDC):

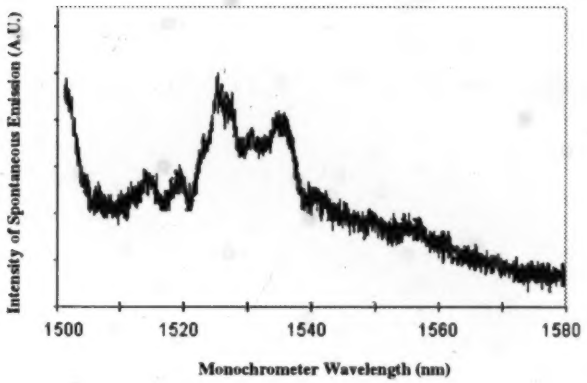

Figure 5.18 Waveguide output spectra from Film PT1,1/3(ErAlSi_bDC) pumped at 968 nm. Spontaneous emission peak observed near 1533 and 1538 nm.

PT1,1/3(ErAlSi_bDC)_RTA:

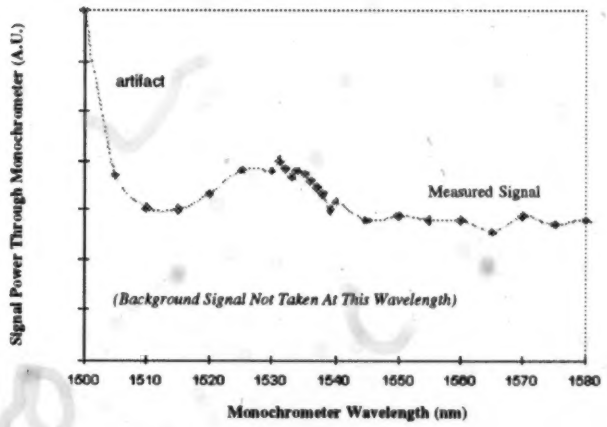

Figure 5.19 Waveguide output spectra from Film PT1,1/3(ErAlSi_bDC) pumped at 968 nm. Spontaneous emission peak observed near 1533 and 1538 nm.

Assessment of Results:

Figures 5.12 to 5.19 show that it was possible to obtain spontaneous emission from several of the films. Film PT00(3%) was the best from the PT00(3%) to PT11(3%) run group. Its output spectrum shows a reasonably broad emission peak from 1530 to 1550 nm when a 974 nm pump wavelength was used. It is possible that the twin peaks observed here were from "Stark splitting" of the 4f energy levels. This is a commonly observed effect.[23][43]

Figures 5.14 and 5.15 show spontaneous emission spectra from Film PT00(3%)_RTA. It would appear that the spontaneous emission observed from this film pumped at 978 nm-pumped film was improved after rapid thermal annealing. The tube furnace anneal did not seem to have a noticeable effect on emission properties.

Figure 5.16 shows the forward throughput spectrum for Film PT00(3%)_heat_RTA - a film that was heated during deposition. In this figure the film was pumped at 974 nm. The peaks clearly became more enhanced, distinct, and more separated than before. Unfortunately, a forward throughput scan on the unannealed PT00(3%)_heat could not be taken because the losses were too high.

Figure 5.18 shows the spontaneous emission for PT1,1/3(ErAlSi_bDC). This is a particularly good emission spectra. The next figure shows the spectra from the same film rapid thermal annealed. Its emission spectra is roughly the same width but does not appear to have the same twin-peak structure. In general, annealing did not appear to improve things, but more tests would have to be performed in order to state this conclusively.

Determination of Best Deposition Procedure:

Bulk Glass Targets:

From the data collected in this thesis for the bulk glass material, it can be concluded that of the films studied, depositing at low pressure (3.3 mTorr) from close range (5.5 cm) and rapid thermal annealing afterwards is the best basic fabrication approach for producing optically active waveguides. It is fortunate that these sputtering conditions also result in the highest deposition rate of all the bulk glass films tested. The deposition rate was far less than was achievable with the powder targets, however.

This film was also the least uniform, which unfortunately is not good for production applications. If a planetary-motion substrate tray had been employed during deposition then film uniformity could be improved. It is my suspicion, as well, that if a commercial substrate heater had been used during deposition then the number of film surface contaminants would be reduced significantly as compared to my makeshift apparatus. This could lead to fewer losses which would make measuring spontaneous emission easier.

Powder Targets:

One definite advantage of using the powder targets was that higher deposition rates could be obtained than for bulk glass. Among the films made from powder targets, the bipolar pulsed DC method produced the film with the most spontaneous emission. The optimum deposition conditions were found to be high pressure (15 mTorr) and a mid-range throw (8.5 cm). It did not appear that rapid thermal annealing was as effective for these films. Unfortunately, the heated-substrate runs were mostly contaminated, so they could not be tested, and there was not enough time to re-deposit them to re-test their optical properties. As a result, no conclusions could be drawn.

5.6 General Discussion On Optical Activity of Films:

I was happy to have obtained forward spontaneous emission from my films even if the results were not as pronounced as those reported in the literature. The major problem I encountered was that the metastable lifetimes of every film studied was too small to be measured. This is a major disadvantage because long lifetimes are required to maintain the population inversions required for stimulated emission.

It is possible that erbium clustering was the culprit. As mentioned in Chapter 1, clustering of erbium ions can lead to a host of problems that reduce the glass' ability to undergo radiative transitions. Aluminum was added to the powder targets to help alleviate this problem since it is known to improve erbium solubility in a glass host. Clearly, it did not help matters sufficiently here. This leads me to wonder whether the deposition system was clean enough for this sputtering application. That is, perhaps the base pressure of mid 10^{-6} Torr was too high given the long deposition times.

A more likely explanation for the lack of reasonable lifetimes stems from chemical composition inconsistency between the target and film. The microprobe results clearly show that film chemistry for film PT00(3%) was inconsistent with the source target, especially at the centre of the wafer. Since the source was optically active, it would seem imperative that film and source chemistry should be identical.

Although film chemistry was inhomogeneous across the surface, it was seen to approach that of the target at the outer edge. As a result, emission measurements should probably have been performed on this region of film rather than the centre. It is possible that the chemistry and/or physical arrangement of the film matrix at the centre did not allow erbium to properly form in the Er^{3+} valence state. In order to investigate this hypothesis, some XPS scans were performed on several of the films to try to ascertain the state of the erbium in the film. Unfortunately, the only information this yielded was that the erbium appeared to be fully oxidized. The particular instrument used at Simon Fraser University was not able to distinguish more than this.

Another possible explanation for the lack of measurable lifetimes was that the films were over-pumped with optical power. Miniscalo, for instance, has pointed out that over-pumping waveguides can actually quench the erbium ions.[44] The primary reason was identified as multi-phonon emission which can occur inside the film when it is overheated. As described in Chapter 1, this can cause phonons to bridge the energy gap and prevent radiative transitions from occurring. This effect also dramatically reduces metastable lifetimes.[44] Alternatively, excited state absorption or upconversion could have been the culprits. I suspect that ESA was not the main problem because no green light was observed radiating from any of the waveguides.

Other authors have reported successful spontaneous emission from films pumped at up to 400 mW[65], so it seems that multi-phonon emission (or whatever process is the problem here) is very material-dependent. Other sources have claimed to observe spontaneous emission and optical amplification using pump powers as low as 30 Watts[66]. As a test, I also pumped some films at low pump powers in this range. Unfortunately, there was not enough light reaching the detector on the output of the monochrometer to register a signal above background noise. The major problem seemed to be coupling losses in, through, and out of the waveguides.

As a procedural improvement, I believe that if some sort of prism-coupling mechanism had been rigged up to couple light in and out of unpatterned films as opposed to a single mode fibre optic / waveguide test system then testing would have been greatly facilitated. With reduces losses lower pump powers could be investigated. This kind of improvement is currently being investigated at AMC.

Chapter 6:

CONCLUSIONS:

Over the course of this thesis, several material and device application issues pertaining to erbium-doped sputtered glass films were investigated. Two main sputtering methods were used. The first, RF sputtering, was used to deposit film from undoped fused quartz as well as erbium and multiple-oxide bulk glass targets. Several issues such as adhesion to silicon and response to annealing were studied. The films from the bulk glass targets required the most care. They would not adhere to plain silicon and selectively "bubbled" off the wafer under even moderate annealing conditions. Adhesion was improved by putting a CVD adhesion layer on the silicon first. This was convenient in this thesis because it also served as the optical cladding layer for the waveguiding tests that were performed later.

The film thickness profiles of these oxide materials were simulated using SIMSPUD which is a commercial software program designed primarily for metal simulation. Through a unique weighted average-calculating algorithm, the sputtering of a complex multiple oxide target was simulated with a fair degree of accuracy. Depending on the experimental conditions chosen, it was observed that by changing the flux emission distribution from the default cosine to cosine^8, a sharper distribution, the simulation accuracy could sometimes be improved. This is a significant observation that shows that some modifications like this one could be incorporated into future versions of the program in order to improve oxide simulation accuracy.

The films sputtered from doped bulk glass targets exhibited a strange property. That is, their refractive indices increased monotonically from the centre out to the edge of the wafers. This is a counter-intuitive phenomenon that contrasted with all the other films studied. A quantitative microprobe analysis was initiated on one of these films, and the chemistry was found to change across the surface. It was found that the concentration of heavy elements was depleted and the concentration of light elements was accentuated at the centre of the film. In fact, the chemistry more closely approached that of the bulk glass source material at the radial edge of the wafer. This definitely accounts for the outward increase in index, but does not explain why the effect was occurring. It was postulated that the film re-sputtering may have been the cause of this behaviour. Further experiment showed that the effect could be minimized by rotating the substrate back and forth under the sputter target during deposition.

The light absorption and spontaneous emission properties were also studied for various films. Unfortunately, no decay lifetimes could be measured from any of the films studied.

Nonetheless, spontaneous emission was observed from several films. The best one from the erbium-doped sputterd bulk glass target was deposited from 5.5 cm away at 3.1 mTorr in a 3:1 Ar to O_2 background gas ratio. It was found that rapid thermal annealing and substrate heating during deposition improved the spontaneous emission characteristics. The best performing film sputtered from the powder targets was deposited from 8.5 cm away at 15.0 mTorr in a 4:1 gas ratio environment. Annealing was not seen to improve performance of these films.

My recommendations for future work include resputtering films from the bulk glass targets, this time with a higher percentage of oxygen in the chamber during deposition. I would reprofile the refractive index trends to see if a radial increase in index of refraction was still observed. Also, I would develop a prism coupling system to be incorporated in the optical test bench at TR Labs so that the films' spontaneous emission could be checked without having to pattern waveguides into them. Hopefully, this would minimize coupling issues and allow lower pump powers to be tested. Also, I would perform more tests on heated and annealed films to see how much the spontaneous emission properties could be enhanced.

References:

[1] V.W.S. Chan, "All Optical Networks", *Sci. Amer. 150th Anniversary Issue.* 72-76 (Sept. 1995).

[2] A. Polman, "Erbium Ion Implantation for Optical Doping", *Materials Synthesis and Proceedings Using Ion Beams.* 385-396 (Nov./Dec. 1993).

[3] Nishihara, H., Haruna, M., Suhara, T., *Optical Integrated Circuits.* U.S.A..: McGraw-Hill Book Company (1985).

[4] A. Polman, D.C. Jacobson, D.J. Eaglesham, R.C. Kistler, J.M. Poate, "Optical Doping of Waveguide Mterials by MeV Er Implantation," *J. Appl. Phys.*. **70** (6), 3778-3785 (Oct. 1991)

[5] R.A. Soref, "Silicon-Based Optoelectronics", *Proc. IEEE*, **81**, No. 12, 1993, 1687-1701.

[6] Keiser, G. *Optical Fibre Communications.* U.S.A., McGraw-Hill, Inc. 1991.

[7] Pollock, Clifford R., *Fundamentals of Optoelectronics.* U.S.A.: Richard D. Irwin, Inc., 1995.

[8] P. Ayliffe, J. Parker, S. Bertolini, T. Clapp, M. Green, P. Harrison, R. Peall, "The Hybrid Integration of Optical and Electronic components on Silicon", *International Journal of Optoelectronics* **9(2)** 179-191 (1994).

[9] G. Zhang, S. Honkanen, A. Tervonen, C.M. Wu, S.I. Najafi, "Glass Integrated Optics Circuit for 1.48/1.55 and 1.30/1.55 μm Wavelength Division Multiplexing and 1/8 Splitting", *Applied Optics* **33(16)** 3371-3374 (June 1994).

[10] K. Jinguji, "Planar Lightwave Circuits: Optical Devices for Processing Optical Signals as Light without Transforming them into Electrical Signals", *NTT Review* **7(1)** 80-86 (Jan. 1995).

[11] U. Hilleringmann, K. Goser, "Optoelectronic System Integration on Silicon: Waveguides, Photodetectors, and VLSI CMOS Circuits on One Chip", *IEEE Transactions on Electron Devices* **42(5)** 841-845 (May 1995).

[12] S.K. Dew, *EE 619 Course Notes*, Department of Electrical Engineering, University of Alberta. (1995).

[13] F.D. Pasquale, M. Federighi, "Modelling of Uniform and Pair-Induced Upconversion Mechanisms in High-Concentration Erbium-Doped Silica Waveguides", *J. Lightwave Technol.* **13**, No. 9. 1858-1864 (Sept. 1995).

[14] R.S. Quimby, W.J. Miniscalco, B. Thompson, "Clustering in erbium-doped silica glass fibres analyzed using 980 nm excited-state absorption", *J. Appl. Phys.* **76** (8), 15 October 1994, 4472-4478.

[15] Jose M. Mir, J.A. Agostinelli, "Optical Thin Films for Waveguide Applications", *J. Vac. Sci. Technol.* **A12(4)** 1439-1445 (Jul./Aug. 1994).

[16] H.K. Kim, C.C. Li, X.M. Fang, G Nykolak, P.C. Becker, "Er-Doped Silicate Glass Films Prepared by Co-sputtering for Optical Amplifiers". *Proc. of the SPIE - The Int. Soc. For Opt. Engineering.*, **2149**, 12-21 (1994).

[17] E.J. Lerner, "Fibre amplifiers expand network capacities", *Laser Focus World*, 85-96, (August 1997)

[18] Y. Lacroix, P. Vella, "How to Optimize Performance of Fibreoptic Amplifiers", *Las. Foc. Wld.* 97-100 (Jan. 1995).

[19] Bjarklev, Anders, *Optical Fibre Amplifiers: Design and System Applications*. Norwood, MA: Artech House, Inc., 1993.

[20] M.R.X. deBarros, G. Nykolak, D.J. DiGiovanni, A. Bruce, W.H. Grodkiewicz, P.C. Becker, "Performance of a High Concentration Er^{3+}-Doped Alumino Silicate Fibre Amplifier", *IEEE Photonics Technology Letters* **8(6)** 761-763 (Jun. 1996).

[21] G. Nykolak, P.C. Becker, J. Schmulovich, Y.H. Wong, D.J. DiGiovanni, A.J. Bruce, "Concentration-Dependent $I_{13/2}$ Lifetimes in Er^{3+} Doped Fibres and Er^{3+} Doped Planar Waveguides", *IEEE Photonics Technology Letters* **5(9)** 1014-1016 (Sep. 1993).

[22] H.K. Kim, C.C. Li, X.M. Fang, G. Nykolak, P.C. Becker, "Er-doped silicate glass films prepared by co-sputtering for optical applications," *SPIE* **2149**, 12-21.

[23] A. Polman, D.C. Jacobson, D.J. Eaglesham, R.C.Kistler, J.M. Poate, "Optical doping of waveguide materials by MeV Er Implantation", *J. Appl. Phys.* 70/71, October 1991, 3778-3784.

[24] S. Raoux, A.S. Barriere, H.J. Lozykowski, I.G. Brown, "High Concentration Erbium Implantation of Epitaxially Grown CaF_2/Si Structures", *Mat. Res. Soc. Symp. Proc.*, **392**, 1995 Materials Research Society, 247-252.

[25] T.Feuchter, E.K. Mwarania, J. Wang, L. Reekie, J.S. Wilkinson, "Erbium-Doped Ion Exchanged Waveguide Lasers in BK-7 Glass", *IEEE Photonics Technology Letters*, **4**, No. 6, June 1992, 542-544.

[26] K. Shuto, K. Hattori, T. Kitagawa, Y. Ohmori, M. Horguchi, "Erbium-Doped Phosphosilicate Amplifier Fabricated by PECVD" *Electronics Letters*, 21 January 1993, **29**, No. 2, 139-141.

[27] S.M. Rossnagel, "Dynamic Interactions in the Physical Properties of Magnetron Deposition Systems", *Material Science and Engineering* **A140** 510-516 (1991).

[28] Brett, M., *UAEM Special Short Course on Thin Film Technology*. Course Notes, University of Alberta, 1996.

[29] J.M. Harper, S. Berg, C. Nender, I.V. Katardjiev, S. Motakef, "Enhanced Sputtering On One Species In the Processing of Multielement Thin Films", *J. Vac. Sci. Technol.*, **10**, No. 4, 1765-1771 (Jul./Aug. 1992).

[30] Vossen, John L., Kern Werner, *Thin Film Processes*. San Diego: Academic Press, Inc., 1991.

[31] J.C. Sellers, "Asymmetric Bipolar Pulse DC: An Enabling Technology for Reactive PVD", 39th Annual Technical Conference Proceedings, Society of Vacuum Coaters (1996).

[32] EN1 DCG-100 Operation Manual Addendum for use with RPG-50, RPG-100.

[33] S. Scaglione, L. Caneve, and F. Sarto, "Sputtering Yield of Optical Materials: Sigmund's Model and Experimental Results", *J. Vac. Sci. Technol.* A **12** (4) 1523-1527 (Jul. 1994).

[34] Dew, Steven K., *Processes and Simulation for Advanced Integrated Circuit Metallization*. PhD. Thesis, Department of Electrical Engineering, University of Alberta, Edmonton, 1992.

[35] Nakamoto, K., *Infrared Spectra of Inorganic and Coordination Compounds*, New York, John Wiley & Sons, 1963.

[36] R.N. Tait, S.K. Dew, T. Smy, M.J. Brett, "Ballistic Simulation of Optical Coatings Over Topology", *SPIE - The Int. Soc. For Optical Engineering*, **1324**, 112-119 (Jul. 1990).

[37] W.J. Minniscalco, "Erbium-Doped Glasses for Fibre Amplifiers at 1500 nm", *J. Lightwave Technol.* **9**, No. 2, 234-250 (Feb. 1992).

[38] F.D. Pasquale, M. Federighi, "Modelling of Uniform and Pair-Induced Upconversion Mechanisms in High-Concentratio Erbium-Doped Silica Waveguides", *J. Lightwave Technol.* **13**, No. 9 1858-1864 (Sept. 1995).

[39] R.N. Tait, *Thin Film Microstructure Effects in VLSI Metallization*, PhD. Thesis, Department of Electrical Engineering, University of Alberta, Edmonton, 1992.

[40] A. Polman, E. Snoeks, G.N. van den Hoven, J.S. Custer, B. Hendriksen, "Erbium Ion Implantation Doping of Opto-Electronic Materials Operating at 1.5 μm", *ECOC '93 19th European Conference on Optical Communication Proceedings*, **2**, 61-64.

[41] O. Lumholt, A. Bjarklev, T. Rasmussen, C. Lester, "Rare Earth-Doped Integrated Glass Components: Modelling and Optimization", *Journal of Lightwave Technology*, **13**, No. 2, February 1995, 275-282.

[42] Feldman, Leonard C. and Mayer, James W, *Fundamentals of Surfaces and Thin Film Analysis*. Netherlands: Elsevier Science Publishing Co. Inc., 1986.

[43] A. Polman, "Erbium Ion Implantation For Optical Doping", *Mat. Res. Soc. Symp. Proc.*, **316**, 1994, 385-396.

[44] W.J. Miniscalco, "Erbium-Doped Glass for Fibre Amplifiers at 1500 nm", *Journal of Lightwave Technology*, **9**, No. 2, February 1991, 234-250.

[45] V. McGahay, M. Tomozawa, "Phase Separation in Rare-Earth-doped SiO_2 Glasses", *Journal of Non-Crystallin Solids*, 159 (1993), 246-252.

[46] R.S. Quimby, Quimby, W.J. Miniscalco, B. Thompson, "Clustering in Erbium-Doped Silica Glass Fibres Analyzed Using 980 nm Excited-State Absorption", *J.Appl. Phys.* **76** (8), 4472-4478 (Oct. 1994).

[47] T. Ohtsuki, N. Peyghambarian, "Gain characteristics of a high concentration Er^{3+}-doped phosphate glass waveguide", *J. Appl. Phys. 78* (6), 15 September 1995, 3617-3621.

[48] M. Federighi, I. Massarek, P.F. Trwoga, "Optical Amplification in Thin Optical Waveguides with High Erbium Concentration", *IEEE Photonics Letters*, **5**, No. 2, February 1993, 227-229.

[49] J.T. Kringlebotn, P.R. Morkel, L. Reekie, J.L. Archambault, D.N. Payne, "Efficient Diode-Pumped Single Frequency Erbium:Ytterbium Fibre Laser", *IEEE Photonics Technology Letters*, **5**, No. 10, October 1993, 1162-1164.

[50] J. Schmulovich, "Er-doped glass waveguide amplifiers on silicon", SPIE Vol. 2996, 143-151.

[51] J. Schmulovich, A. Wong, Y.H. Wong, P.C. Becker, A.J. Bruce, R. Adar, "Er^{3+} Glass Waveguide Amplifier at 1.5 mm on Silicon" *Electronics Letters*, 18 June 1992, **28**, No. 13, 1181-82.

[52] Friedrich, Loran, *Simulation of Sputter Reflow of Copper*. PhD. Thesis, Department of Electrical Engineering, University of Alberta, Edmonton, 1997.

[53] F. Pasquale, M. Federighi, "Modelling of Uniform and Pair-Induced Upconversion Mechanisms in High-Concentration Erbiu-Doped Silica Waveguides" *Journal of Lightwave Technology*, **13**, No. 9, September 1995, 1858-1864.

[54] M.J. Brett, R.N. Tait, S.K. Dew, T. Smy, S. Kamasz, and A.H. Labun,"Nodular defect growth in thin films",*Journal of Materials Science: Materials in Electronics* **3**, 64-70 (1992).

[55] Scott, V. D., Love, G., *Quantitative Electron-Probe Microanalysis*. England: Ellis Horwood Lt, 1983.

[56] Muller, Richard S., Kamms, Theodore I., *Device Electronics for Integrated Circuits*. Canada: John Wiley and Sons, Inc., 1977.

[57] H. Rigneault, F. Flory, S. Monneret, "Non-linear totally reflecting prism coupler: thermomechanical effects and intensity-dependent refractive index of thin films", *Applied Optics*, **34**, No. 21, 20 July 1995, 4358-4368.

[58] Hook, J.R., Hall, H.E., *Solid State Physics: Second Edition*. England: John Wiley and Sons Ltd., 1991.

[59] C. Kittel, *Introduction to Solid State Physics, Sixth Edition*, Wiley, New York, 1986.

[60] *Fwave IV A Vector E-M Wave Solver, Instructions For Use*, MRS Taylor, 1996.

[61] *CRC Handbook of Chemistry and Physics: 67th Edition, 1986-87*. U.S.A.: Chemical Rubber Publishing Company.

[62] B.A. Movchan, A.V. Demchishin, "Study of the Structure and Properties of Thick Vacuum Condensates of Nickel, Titanium, Tungsten, Aluminum Oxide, and Zirconium Dioxide", *Fiz. Metal. Metalloved.*, **28**, No.4, p. 653, 1969

[63] Flinn, Richard A., Trojan, Paul K., *Engineering Materials and Their Applications: Fourth Edition*. Boston: Houghton Mifflin Company, 1990.

[64] Hecht, *Optics: Second Edition*. U.S.A.: Addison-Wesley Publishing Company, Inc., 1987.

[65] H.K. Kim, C.C. Li, "Photoluminescence and electrical properties of erbium-doped indium oxide films prepared by r.f. sputtering", *J. Appl. Phys.* **76** (12), 15 December 1994, 8209-8211.

[66] W.J.. Wang, S.I. Najafi, S. Honkanen, Q.He, C.Wu, J. Glinski, "Erbium-Doped Composite Glass Waveguide Amplifier", *Electonics Letters*, Sept. 24 1992, **28**, No. 20, 1872-1873.

[67] Heavens, O.S., *Optical Properties of Thin Solid Films*. New York: Dover Publications Inc., 1991.

[68] Herman, Irving P., *Optical Diagnostics for Thin Film Processing*. U.S.A.: Academic Press, 1996.

[69] Streetman, Ben G., *Solid State Devices: Third Edition*. New Jersey: Prentice-Hall, 1990.

[70] O'Conner, D.J., Sexton, B.A., Smart, R.St.C., *Surface Analysis Methods in Material Science*. Berlin: Springer-Verlag, 1992.

[71] Halliday, David, Resnick, Robert, *Fundamentals of Physics: Third Edition*. New York: John Wiley and Sons, Inc., 1988.

[72] Varshveya, Aruu, *Fundamentals of Inorganic Glasses*. New York: Academic Press, Inc, 1994.

[73] Adams, M.J., *An Introduction to Optical Waveguides*. New York: John Wiley and Sons Ltd., 1981.

[74] Knittl, Zobuek, *Optics of Thin Films*. Czechoslovakia: John Wiley and Sons Ltd., 1976

[75] Nudelman, Sol, Mitia, S.S., *Optical Properties of Solids*. New York: Plenum Press, 1969.

[76] Lerner, Rita G., Trigg, George L., *Encyclopedia of Physics: Second Edition*. New York: VCH Publishers, Inc., 1991.

[77] Illingworth, Valerie, *Dictionary of Physics*. England: Longman Group Ltd., 1991.

[78] Anderson, Herbert L., *A Physicist's Desk Reference*. New York: American Institute of Physics, 1989.

[79] A. Ishimaru, "Optical Multiple Scattering by Particles", Part. Part. Syst. Charact. **11** 183-188 (1994).

[80] H. Jerominek, S. Patela, J.Y.D. Pomerleau, C. Delisle, R.Tremblay, "Some Properties of R.F. Planar Magnetron-Sputtered Corning 7059 Glass Films", Thin Solid Films **146** 191-200 (1987).

[81] A.M. Meyers, J.R. Doyle, R. Abelson, D.N. Ruzic, "Monte Carlo Simulations of Magnetron Sputtering Particle Transport", J. Vac. Sci. Technol. **A9(3)** 614-618 (May/Jun 1991).

[82] R. Kaltofer, G. Weise, "Plasma Diagnostic Studies of Low-energy Ion Bombardment in R.F. Magnetron Sputter deposition", Surface and Coatings Technology **74-75** 469-473 (1995).

[83] R.E. Somekh, "The Thermalizatio of Energetic Atoms During the Sputtering Process", J. Vac. Sci. Technol. **A2(3)** 1285-1291 (July/Sept. 1984).

[84] R.S. Robinson, "Energetic Binary Collisions in Rare Gas Plasmas", J. Vac. Sci. Technol. **16(2)** 185-189 (Mar./Apr. 1979).

[85] G.M. Turner, I.S. Falconer, B.W. James, D.R. McKenzie, "Monte Carlo Calculations of the Thermalization of Atoms Sputtered from the Cathode of a Sputtering Discharge", J. Apll. Phys. 65(9) 3671-79 (May 1989).

[86] S.M. Rossnagel, D. Mikalsen, H. Kinoshita, J.J. Coumo, "Collimated Magnetron Sputter Deposition", J. Vac. Sci. Technol. **A9(2)** 261-265 (Mar./Apr. 1991).

[87] H.M. Urbassek, D. Sibold, "Sputtered Atom Transport in High-Current Gas Discharges: A self-consistent Computer Simulation Study", J. Vac. Sci. Technol. **A11(3)** 676-681 (May/Jun. 1993).

[88] W.N.G. Hitchon, G.J. Parker, J.E. Lawler, "Accurate Models of Collisions in Glow Discharge Simulations", IEEE Transactions on Plasma Science, Vol. 22 No. 3 (June 1994).

[89] S.M. Rossnagel, K. Schatz, S.J. Whitehair, R.C. Guarnieri, D.N. Ruzic, J.J. Cuomo, "The Effects of Substrate Potentials on Electron Cyclotron Resonance Plasmas", J. Vac. Sci. Technol. **A9(3)** 702-706 (May/Jun. 1991).

[90] S.M. Rossnagel, M.A. Russak, J.J. Cuomo, "Pressure and Plasma Effects on the Properties of Magnetron Sputtered Carbon Films", J. Vac. Sci. Technol. **A5(4)** 2150-2153 (Jul./Aug. 1987).

[91] A.M. Ektessabi, "Ion-beam-assisted Sputter Deposition of Thin Oxide Films", Surface and Coatings Technology **68/69** 208-216 (1994).

[92] G.M. Turner, "Monte Carlo Calculations of Gas Rarefaction in a Magnetron Sputtering Discharge", J. Vac. Sci. Technol. **A13(4)** 2161-2169 (Jul./Aug. 1995).

[93] G.M Turner, J.S. Falconer, B.W. James, D.R. McKenzie, "Monte Carlo Calculations of the Properties of Sputtered Atoms at a Substrate Surface in a Magnetron Discharge", J. Vac. Sci. Technol. **A10(3)** 455-461 (May/Jun. 1992).

[94] S.M. Rossnagel, "Gas Density Reduction Effects in Magnetrons", J. Vac. Sci. Technol. **A5(1)** 19-24 (Jan./Feb. 1988).

[95] S.M. Rossnagel, "Energetic Particle Bombardment of Films during Magnetron Sputtering", J. Vac. Sci. Technol. **A7(3)** 1025-1029 (May/Jun. 1989).

[96] S.M. Rossnagel, J.J. Whitehair, C.R. Guarnieri, J.J. Cuomo "Plasma Induced Heating in Electron Cyclotron Resonance Sources", J. Vac. Sci. Technol. **A8(4)** 3113-3117 (Jul./Aug. 1990).

[97] R.N. Tait, S.K. Dew, T. Suny, M.J. Brett, "Ballistic Simulation of Optical Coatings Deposited over Topography", SPIE **1324** Modelling of Optical Films II 112-119 (1990).

[98] L.J.Friedrich, S.K. Dew, M. Brett, T. Suny, "Thin Film Microstructure Modelling through Line-Segment Simulation", Thin Solid Films **266** 83-88 (1995).

[99] S. Schiller, K Goedicke, V. Kirchhoff, T. Kopte, "Pulsed Technology - A New Era of Magnetron Sputtering", 38th Annual Technical Conference Proceedings, Society of Vacuum Coaters (1995).

[100] F. Ladonceur, J.D. Love, T.J. Senden, "Effect of Side Wall Roughness in Buried channel Waveguides", IEEE Proceedings in Optoelectronics **141(4)** 1439-1445 Jul./Aug. 1994).

[101] H. Ding, P. Gerard, P. Benech, "Radiation Modes of Lossless Multilayer Dielectric Waveguides", IEEE Journal of Quantum Electronics, **31(2)** 411-416 (Feb. 1995).

[102] R.A. Soret, "Silicon-based Optoelectronics", Proceedings of the IEEE, **81(12)** 1687-1702 (Dec. 1993).

[103] S. Yokoyama, T. Nagata, Y. Kuroda, T. Doi, T. Namba, K. Miyake, T. Miyamoto, S. Miyazaki, M. Koyangi, M. Hirose, "Optical Waveguides on Silicon Chips", ", J. Vac. Sci. Technol. **A13(3)** 629-635 (May/Jun. 1995).

[104] S. Suzuki, M. Kawachi, "Planar Lightwave Circuits Based on Silica Waveguides on Silicon", Electronics and Communications in Japan, Part 2 **77(11)** 184-193 (1994).

[105] D. Zurhelle, J.P. Schmidt, R. Hoffman, D. Sander, J. Muller, "Coupling Structures for Active and Passive Integrated Opto-electronic Components and Circuits on Silicon", SPIE **2397**, 666-682.

[106] T. Nagata, T. Namba, Y. Kuroda, K. Miyake, T. Miyamoto, S. Yokoyama, S. Miyazaki, Mkoyanagi, M. Hirose, "Single-Chip Integration of Light Emitting diode, Waveguide, and Micromirrors", Jpn. J. Appl. Phys., Vol. 34 Pt. 1, No. 2B 1282-1285 (1995).

[107] H. Nakagima, "Advanced Optical Packaging Technology for Practical Integrated Photonic Modules", Electronics and Communications in Japan, Part 2 **78(1)** 352-362 (1995).

[108] T. Numai, "Surface Emitting Optical Devices for 2-D Integration", SPIE **2145** 58-68.

[109] J.Y. Chen, S.I. Najakfi, "Adiabatic Polymer-glass Waveguide All-Optical Switch", Applied Optics **33(16)** 3375-3383 (1994).

[110] C.Y. Li, J. Chisham, M. Andrews, S.I. Najafi, J.D. MacKenzie, N. Peyhambarian, "Sol-gel Integrated Optical Coupler by UV Light Imprinting", Electronics Letters **31(4)** 271-272 (16th February 1995).

[111] S. Jacobson, P. Landi, T. Findakly, J. Stamatoff, H. Yoon, "Non-Linear optical Polymers in Advanced Photonics", Journal of Applied Polymer Science **53** 649-663 (1994).

[112]H. Honmou, M. Itoh, "Optical Coupling of Laser Diode Array to Single-mode Fibre Array with Heat-treated Hemispherical Microlens", Electronic Letters **31(10)** 793-794 (May 1995).

[113] S.I. Najak, S. Honkanen, "Ion-exchanged Glass Waveguides for Active Integrated optical Devices", Electrochemical Society Meeting, Toronto, invited paper (1992).

[114] A. Wakahara, K. Pak, T. Sato, H. Yonezu, A. Yoshida, "A Novel Selective Heteroepitaial Growth Method of InP on GaAs by Metallorganic Vapor Phase Epitaxy", J. Electrochem. Soc. **137(6)** 1995-1997 (June 1990).

[115]V. Rodino, "Packaging Integrated Optics to Withstand Environmental Rigors", Photonics Spectra 116-118 (Aug. 1994).

[116] R. Comerford, "The Internet's Growing Pains", Spectrum 46-55 (Sept.1996).

[117] T. Kitagaws, K. Hattori, K. Shuto, M. Yasu, M. Kobayashi, M. Horiguchi, "Amplification in Erbium-Doped Silica-Based Planar Lightwave Circuits", Electronics Letters, **28**, No. 20, Sept. 10, 1992, 1872-1873.

[118] T.H. Hockstra, P.V. Lambeck, H. Albers, T.J.A. Popma, "Sputter-Deposited Erbium-Doped Y2O3 Active Optical Waveguides", Electronics Letters, **29**, No. 7, 01 April 1993, 581-583.

[119] B. Wu, P.L. Chu, J. Arkwrite, "Ytterbium-Doped Silica Slab Waveguide with Large Nnlinearity", IEEE Photonics Technology Letters, **7**, No. 12, December 1995, 1450-1452.

[120] F.D. Pasquale, M. Federighi, "Improved Gain Characteristics in High-Concentration Er^{3+}/Yb^{3+} Codoped Glass Waveguide Amplifiers", IEEE Journal of Quantum Electronics, **30**, No. 9, Sept. 1994, 2127-2131.

[121] M. Federighi, F.D. Pasquale, "The Effect of Pair-Induced Energy Transfer on the Performance of Silica Waveguide Amplifiers with High Er^{3+}/Yb^{3+} Concentrations", IEEE Photonics Technology Letters, **7**, No. 3, March 1995, 303-305.

[122] P. Laporta, S. Taccheo, O. Svelto, "High-Power and High Efficiency Diode-Pumped Er:Yb:Glass Laser", Electronics Letters, **28**, No. 5, 27 February, 1992.

[123] C. Lester, A. Bjarklev, T. Rasmussen, "Modelling of Yb3+-Sensitized Er3+-Doped Silica Waveguide Ampifiers", Journal of Lightwave Technology, **13**, No. 5, May 1995, 740-743.

[124] S. Raoux, S. Anders, K.M. Yu, I.C. Ivanov, I.G. Brown, "Plasma Synthesis of Rare Earth Doped Integrated Optical Waveguides", Mat. Res. Soc. Symp. Proc., **392**, 1995 Materials Research Society, 241-246.

[125] M. Nakazawa, Y. Kimura, "Electron Beam Vapour-Deposited Erbium-Doped glass Waveguide Laser at 1.53 μm", Electronics Letters, **28**, No. 22, 22 October, 1992, 2054-2056.

[126] R.P. Tumminelli, B.C. McCollum, E. Snitzer, "Fabrication of High Concentration Rare-Earth Doped Optical Fibres Using Chelates", Journal of Lightwave Technology, **8**, No. 11, Nov. 1990, 1680-1683.

[127] G.N. van den Hoven, J.H. Shin, A. Polman, S. Lombardo, S.U. Campisano, "Erbium in oxygen-doped silicon: optical excitation", J. Appl. Phys., **78**, (4), 15 August 1995, 2642-2649.

[128] C. Buchal, "Ion Implantation for Optical Applications", Nuclear Instruments and Methods in Physics Research, **B** 96 (1995), 370-373.

[129] R.Scheps, "Photon Avalanche Upconversion in Er3+:YAlO3" IEEE Journal of Quantum Electronics, **31**, No. 2, February 1995, 309-316.

[130] W. Xu, S. Dai, L.M. Toth, G.D. Del Cul, J.R. Peterson, "Green Upconversion Emission from Er3+ Ion Doped Into Sol-Gel Silica Glasses Under Red Light (647.1 nm) Excitation", J. Phys. Chem. **1995**, 99, 4447-4450.

[131] G.N. van den Hoven, E. Snoeks, A. Polman, C. van Dam, J.W.M. van Uffelen, M.K. Smit, "Upconversion in Er-Implanted Al2O3 Waveguides", J. Appl. Phys. **79** (3), 1 February 1996, 1258-1265.

[132] J. Thorgersen, N. Bjerre, "Multiphoton absorption and cooperative upconversion excitation in Er3+-doped fibres", Optics Letters, **18**, No. 3, 1 February 1993, 197-200.

[133] P. Blixt, J. Nilsson, T. Cailnas, B. Jaskorzynsha, "Concentration-Dependent Upconversion in Er3+-Doped Fibre Amplifiers: Experiments and Modelling", IEEE Transactions Photonics Technology Letters, **3**, No. 11, November 1991, 996-998.

[134] D.A. Turnbull, V. Krasteva, G.H. Sigel, S.G. Bishop, "Broad Band Excitation of Rare Earth Emission in Chalcogenide Glasses", SPIE Vol. 2996, 20-24.

[135] S. Honkanen, T. Ohtsuki, S. Jiang, S.I. Najafi, N. Peyghambarian, "High Concentration Phosphate Glasses for Planar Waveguide Amplifiers", SPIE Vol. 2996, 32-39.

[136] J.E. Shelby, J.T. Kohle, "Rare-Earth Aluminosilicate Glasses", J. Am. Ceram. Soc., **73** (1), 1990, 39-42.

[137] G. Nykolak, M. Haner, P.C. Becker, J. Schmulovich, Y.H. Wong, "Systems Evaluation of an Er3+-Doped Planar Waveguide Amplifier", IEEE Photonics Technology Letters, **5**, No. 10, October 1993, 1185-1187.

[138] O. Lumholt, A. Bjarklev, T. Rasmussen, C. Lester, "Rare arth-Doped Integrated Glass Components: Modelling and Optimization", Journal of Lightwave technology, **13**, No. 2, February 1995, 275-282.

[139] E. Delevaque, T. Georges, M.Monerie, P. Lmonber, J. Bayon, "Modellin of Pair-Induced Quenching in Erbium-Doped Silicate Fibres" IEEE Photonics Technology Letters, **5**, No. 1, January 1993, 73-75.

[140] T. Pfeiffer, H. Bulow, "Analytical Gain Equation fot Erbium-Doped Fibre amplifiers including Mode Field Profiles and Dopant Distribution", IEEE Photonics Technology Letters, **4**, No. 5, May 1992, 449-451.

[141] J.V. Gates, A.J. Bruce, J. Schumulovich, Y.H.Wong, G. Nykolak, M.R.X. deBarros, R. Ghosh, "Fabrication of Er Doped Glass Films as used in Planar Optical Waveguides", Mat. Res. Soc. Symp. Proc. **392** 209-216.

[142] R.N. Ghosh, J. Schmulovich, C.F. Kane, M.R.X. deBarros, G. Nykolak, A. Bruce, P.C. Becker, "8-mW Threshold Er3+-Doped Planar Waveguide Amplifier", IEEE Photonics Technology Letters **8(4)** 518-520 (Apr. 1996).

[143] G.N. van den Hoven, R.J. Koper, A. Polman, C. van Dam, J.W. van Uffelen, M.K. Smit, "Net optical gain at 1.53 μm in Er-Doped Al2O3 waveguides on silicon", Appl. Phys Lett. **68** (14), 1 April 1996, 1886-1888.

[144] M. Federighi, J. Masserek, P.F. Trwoga, "Optical Amplification in Thin Optical Waveguides with high Er Concentration", IEEE Photonics Technology Letters, **5**, No. 2, February 1993, 227-229.

[145] M. Shimizu, M. Yamada, M. Horiguchi, E. Sugita, "Concentration Effect on Optical Amplification Characteristics of Er-Doped Silica Single-Mode Fibres", IEEE Photonics Technology Letters, **2**, No. 1, January 1990, 43-45.

[146] J.L. Wagener, P.F. Wysocki, M.J.F. Digonnet, H.J. Shaw, "Effects of Concentration and Clusters in Erbium-Doped Fibre Lasers", OPTICS LETTERS, **18**, No. 23, 1 December 1993, 2014-2016.

[147] H. Savaloni, M.A. Player, "Morphological changes in UHV deposited Er/a-C films: nucleation, growth and grain structure", Thin Solid Films **256** (1995), 48-58.

[148] Metricon Model 2010 Prism Coupler Thin Film Thickness / Refractive Index Measurement System operating and Maintenance Guide Rev. (9/91).

[149] R. Ulrich, R. Torge, "Measurement of Thin Film Paramenters with a Prism Coupler", Applied Optics, Dec. 1973, **12**, No. 12, 2901-2908.

[150] A.C. Adams, D.P. Schinke, C.D. Capio, "An Evaluation of the Prism Coupler for measuring the Thickness and Refractive Index of Dielectric Films on Silcon Substrates", **126**, No. 9, Sept. 1979, 1539-1541.

APPENDIX A: *Prism Coupler Operating Principles*

Prism coupling is a technique for determining film thickness and refractive index of the non-absorbing films. It is accepted among current literature as the most accurate tool available to perform thickness and index measurements. A laser beam is coupled by a prism into a planar light-guiding film.[57] The prism is placed in direct contact with the film slab and both are rotated on a motorized mechanism such that the incident beam subtends a large angle of incidence with respect to the prism face. Refer to Figure A1. Reflected light shines onto a photodetector, and intensity is plotted as a function of Θ.

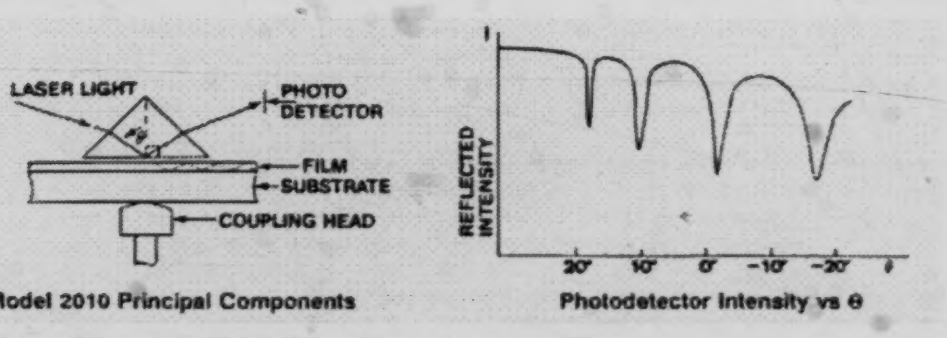

Figure A1 Prism coupling mechanism and example mode spectra.[PC1]

The reflected light intensity on the detector face decreases sharply at angles were the light couples into the film. Strong coupling occurs when the incident phase velocity of the light, vi, equals the phase velocity of one of the characteristic modes in the film.

$$v_{phase} = {}^{c}/_{n_{prism}} \sin \Theta \qquad \text{(A1.1) [57]}$$

Coupled light will propagate down the film by total internal reflection and maintains lateral beam confinement for several centimeters.

There is a computer connected to the instrument which performs simultaneous calculations of film thickness and refractive index. This is possible as long as at least two modes are supported in the film and the film is within the thickness range of the instrument.[57] Using the Metricon Model 2010, one parameter can be measured at a time from 0.2 to 0.5 μm only. Between 0.5 and 15 μm both can be measured simultaneously.[57] Measurements can also be taken for single or double-layer films provided the top layer has a higher index of refraction.

The angular position of the modes depends on film thickness and refractive index. With at least two modes supported, the computer can calculate *t* and *n* using an algorithm found in the literature.[57] Multiple modes allow the computer to reduce the standard deviation in the calculations in order to improve calculation accuracy. If only one film mode is supported then one parameter can be calculated as long as the other is defined by the user.

In Figure A2 the Alpha-Step / Prism Coupler correlation accuracy can be seen to be within around +/- 50 to 75 nm. To be conservative and to take into account that the profilometer could be out by perhaps as much as 50 to 75 nm, it is reasonable to assume that the prism coupler thickness measurements have a +/- 150 nm uncertainty.

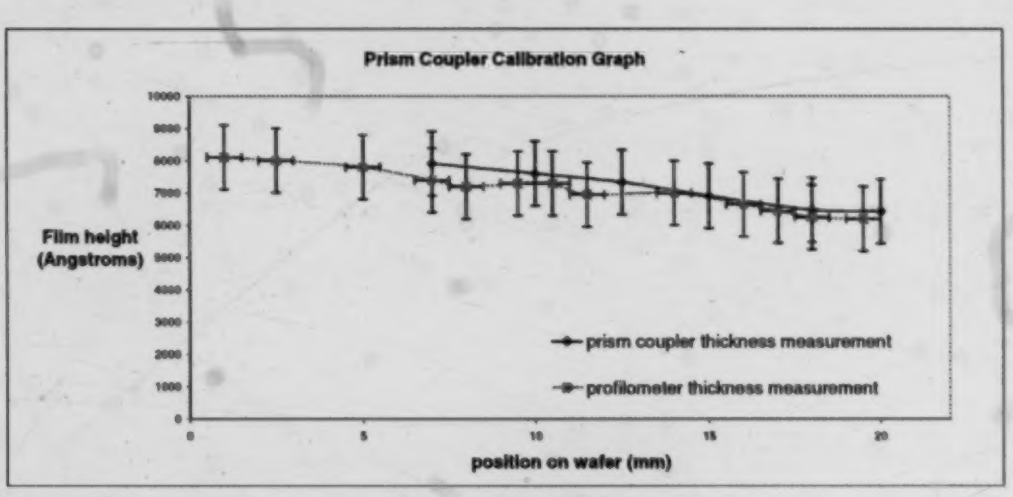

Figure A2 Comparison of prism coupler output and alpha-step profilometer.
Error bars drawn here are 100 nm tall but choose 150 nm as the estimate.

Example Thickness and Refractive Measurements:

(using a CVD oxide layer as a reference)

Figure A3 shows the prism coupler coupled mode spectra for a PECVD oxide film on a silicon wafer. Since 632.8 and 1550 nm lasers are available, I used both to take measurements with. Using the same position on the wafer as a test spot, I checked the film thickness and refractive index at both wavelengths. The left figure shows the results for 632.8 nm light; while the left is for 1550 nm light. The thickness and refractive index values are shown below. Notice that more modes are captured for the 632 nm light. Repeated measurements were taken, and an estimate of 0.001 was determined for the refractive index inconsistency.

The intended purpose of this figure is to assess the consistency of the thickness-measuring capacity of the device at two wavelengths and to compare the index at 632 nm index value to the accepted standard value of around 1.46 for CVD oxide.[56] As we can see, the thickness values are similar, and the measured index is close to 1.46.

Data:	*632.8 nm laser*	*1550 nm laser*
	n = 1.459 (+/- 0.001)	*n = 1.448 (+/- 0.001)*
	t = 5.048 μm (+/- 150 nm)	*t = 4.947 μm(+/- 150 nm)*

Figure A3 Prism coupler mode spectra for 5 micron CVD oxide layer.
Measurements are taken at two wavelengths (632.8 nm and 1550 nm).

There is roughly a 100 nm difference in thickness between the measurements at 632 and 1550 nm. This is within the 150 nm error bar determined for this instrument. In addition, the accepted value for a CVD film is 1.46 at the HeNe wavelength, 632.8 nm. According to this instrument, the refractive index is 1.459 at this wavelength. This is within the 0.001 error bar that I determined from repetitive measurements.

Dual Film Mode:

The prism coupler had to be operated in a special "dual-film" mode for the films that were deposited onto optical cladding layers. This feature allowed for simultaneous measurement of the thickness and refractive index of two vertically adjacent glass layers provided at least two modes were captured in each film. The following figure shows an example of a dual-film mode spectra for a 3% Er-doped film on top of 5 microns of oxide. The left half belongs to the upper film; while the right half belongs to the cladding layer.

The computer distinguishes the two layers based on the refractive index it calculates for each. It cannot always distinguish whether modes belong to the upper or lower film especially if the films are similar in index value. To compensate, the user specifies a "dead zone" width between the two regions so that it does not get confused.

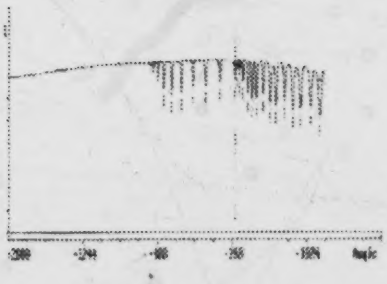

The mode pattern on the left hand side of the spectra corresponds to the upper film while the right corresponds to the lower film. The laser wavelength was 632.8 nm.

Data: *632.8 nm laser*

Upper Film:	*Lower Film:*	***Uncertainty***
n = 1.606	*n = 1.460*	*(+/- 0.001)*
t = 4.517 μm	*t= 5.058 μm*	*(+/- 150 nm)*

Figure A4 A typical dual film measurement

Refractive Measurements on Bulk Glass:

The prism coupler can be used to measure the refractive index of bulk materials, as well. The principle of operation is simple. Laser light directed at the base of a prism will be totally reflected at the base of the prism until the angle of incidence drops below the critical angle. The critical angle is simply

$$\Theta = \arcsin(n/n_p). \qquad \text{(A1.2)}$$

I utilized this feature to attempt another check on the refractive index measuring capability of this instrument. That is, I measured the refractive indices of the bulk glasses to determine if there was any discrepancy between the manufacturer's quoted values and the numbers that the prism coupler produced. The index of the 3% erbium-doped glass was quite close to the manufacturer's, but there was a fairly significant difference between the quoted and measured values for the 1% glass. I cannot account for this discrepancy with much certainty, except to suggest that this particular bulk glass sample could have been off-spec from the manufacturers quote due to manufacturing inconsistencies.

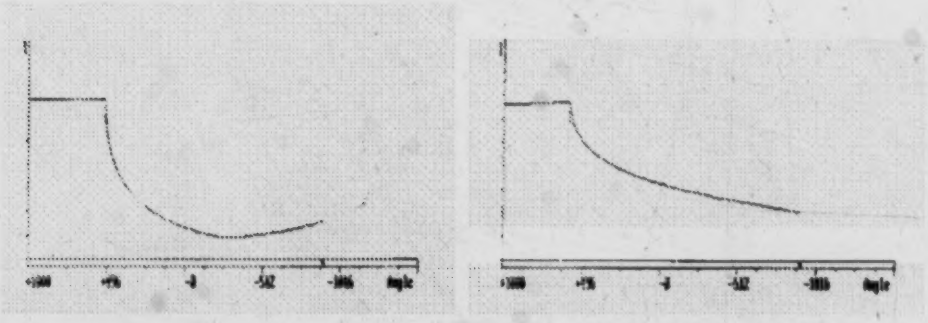

(a) Glass A (632.8 nm) (b) Glass B (632.8 nm)

* Measured Refractive Indices Data for Bulk Glass:

	Glass A (1% erbium):	*Glass B (3% erbium):*	***Uncertainty***
632.8 nm	*n = 1.596*	*n = 1.606*	*(+/- 0.001)*
1550 nm	*n = 1.582*	*n = 1.593*	*(+/- 150 nm)*

* Manufactureer's Refractive Indices Data for Bulk Glass:

	Glass A (1% erbium):	*Glass B (3% erbium):*
632.8 nm	*n = 1.606*	*n = 1.606*
1550 nm	*n = 1.595*	*n = 1.594*

Figure A5 Example Bulk glass refractive index measurements.

APPENDIX B: *Procedure for Assembling Simulated Film Thickness Profiles for Multiple-Species Oxides*

All the parameters for sputter simulations were contained in the files "default.spud" and "[run_name].spud." An example of a specific simulation file for the erbium metal PT00(3%) can be found below for a cosine[1] simulation.

```
gen_stop 9000000
binding_E 3.29
particle_mass 167.26
gas_temperature 125
max_radius 3.81
sim_radius 15.0
sub_distance 5.5
pressure 3.1
sigma 42
therm_sigma 26
target_voltage 160
seed 101
thick_bins 30
lin_prof_bins 25
target_file "ti.liu.target"
emission_file "cos_1.emit"
```

The key parameters to note here are the number of particles generated - *9000000*, the cohesive binding energy - *3.29 eV for erbium*, [59] molar mass - *167.26 g/mol*, the assumed plasma temperature - *125 degrees Celcius*, the net DC bias on the target - *160 Volts*, the target-substrate throw distance - *5.5 cm*, the combined pressure of the background argon and oxygen gases - *3.1 mTorr*, the target erosion file - *"ti.liu.target"*, and the emission distribution file - *"cosb.emit"*, and the sigma and thermal sigma values.

The *sigma* and *therma sigma* values were unknown for most of the elements detected by the microprobe. Some empirically-determined values were, nonetheless, available for Al, Cu, Mo, Ti, and W. After some investigation, it was concluded that among the obvious properties that one can find in data books - like atomic radius and binding energy - sigma values are most

strongly dependent on atomic mass. The known sigma and thermal-sigma values were plotted as a function of atomic mass, and the others were interpolated from the graph in Figure B1. The results are summarized in Table B1.

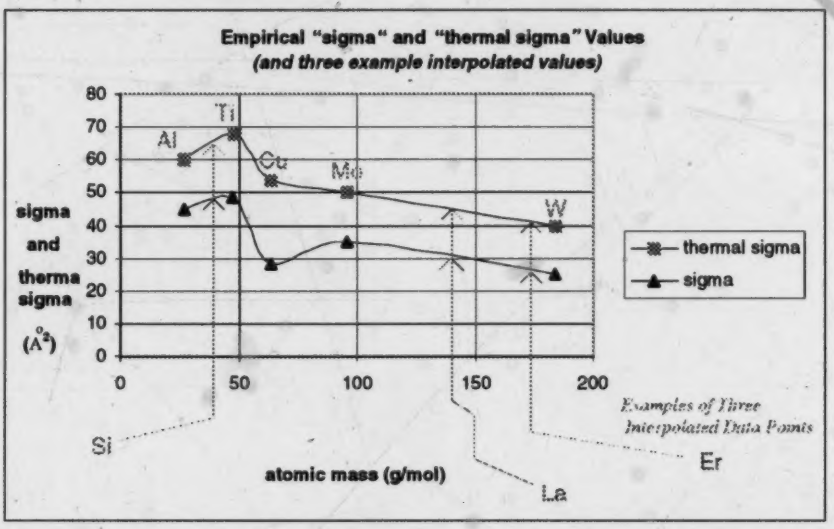

Figure B1 Interpolating sigma and thermal sigma values from atomic weight distribution.

species	atomic number	particle mass	specific gravity oxide molecule	calculated molecular volume ($x10^{-23}$ cm^3)	sigma (Angstrom²)	therm_sigma (Angstrom²)	binding_E (eV/atom)
Na	11	22.99	2.27	4.53	60.00	45.00	1.11
Al	13	26.98			60.00	45.00	3.39
Si	14	28.09	2.19	4.56	55.00	42.00	4.63
K	19	39.10	2.32	6.74	64.00	47.00	0.93
Ti	22	47.90			68.00	48.00	4.85
Cu	29	63.55			54.00	28.00	3.49
Zn	30	65.38	5.61	2.41	54.00	28.00	1.35
Mo	42	95.94			50.00	35.00	6.82
La	57	138.91	6.51	8.31	46.00	29.00	4.47
Ba	56	137.33	5.72	4.45	32.00	46.00	1.90
Ce	58	140.12	7.132	4.01	28.00	42.00	4.32
Er	68	167.26	8.64	7.35	42.00	26.00	3.29
W	74	183.85			40.00	25.00	8.90

Table B1 Table of known and interpolated values from above graph.

The algorithm for assembling the weighted composite film profiles will now be described. First, sputter distributions were simulated for the eight metals detected by the microprobe - Ba, Ce, Er, K, La, Na, Si, and Zn. All four deposition conditions were simulated using both

cosine[1] and cosine[8] initial sputter flux distributions. This required 64 runs, each using 9 million particles. The key output from these runs were the film thickness profiles and deposition efficiencies for each element.

Once each element was simulated, the relevant output was imported into an Excel spreadsheet, and each thickness distribution was normalized. To do this, all the thickness values in the distributions were summed from wafer centre to edge and then each individual value was divided by the sum. This was done for all eight elements and all eight simulation conditions.

In order to calculate a weighted average of arriving flux, the source material's stoichiometry had to be incorporated into the worksheet. This presented a small challenge because SIMSPUD's thickness profile numbers represent a *numerical quantity* of deposited atoms while quantitative microprobe analysis numbers are in terms of relative atomic *mass percentages*. As a result, the microprobe weight percentage data had to be converted to atomic percentages.

To simplify matters, the number of atoms, N, in a single gram (1g) of each element were calculated using, $N = {}^{(1g)}N_A / M$, where N_A is Avogadro's number and M is the molecular weight of the element in g/mol.

These numbers were then multiplied by the mass fraction of each element from Table 3.5. This gave the number of atoms of each element in one gram of the target, $N_{indiv(1g)}$. By summing all these individual elemental values, the total number of atoms in 1 gram of target sample was determined. Of course, there was some error in this calculation due to the statistical error in the microprobe data and because missing data was not accounted for. Nonetheless, the individual *atomic* percentages for each element could easily be calculated this way by dividing the sum into each $N_{indiv(1g)}$ value.

This process accomplished the task of converting the microprobe stoichiometry from weight percentages to atomic percentages. This, in turn, allowed an average elemental thickness profile to be calculated. To do this, each of SIMSPUD's normalized radial thickness profiles were multiplied by their *atomic* percentage in the target. Then they were multiplied by the simulated deposition efficiencies calculated for each element. This gave the amount of *landed flux* for each element.

The second last step in obtaining the composite thickness profiles was to incorporate the approximate diameter of each oxide. In order to bring a more realistic physicality to the simulations. Individual molecule volumes were calculated using specific gravity values for each oxide[61] using the formula:

$$V_{(molecule[cm^3])} = {}^{M_{(molcular\_weight[g/mol])}} / {}_{Na[1/mol] \times \rho[g/cm^3]} \qquad (B1.1)$$

Since spherical volume is proportional to diameter^3, the average diameter of each molecule was approximated by taking the cube root of Equation B1.1. Each "landed flux" profile was then multiplied by this number. The final step was to sum all eight simulated elements at each radial position in the distributions and plot the result in the graphs in Figure 3.8. The figure shows cosine^1 and cosine^8 simulations superimposed with experimental values. The simulated data was normalized to the r=0.0 data point from the experimental runs.

APPENDIX C: *Calculation Procedure For Uncertainty In Microprobe Data*

The uncertainties in the data were calculated strictly on a statistical basis using classic statistical argument from the binomial distribution that the uncertainty in an arbitrary data set equals $^1/\sqrt{n}$, where n is the size of the data sample. In this case n corresponds to the number of X-ray counts. The number of counts for any particular element is determined from the major peaks on the microprobe spectra by using Equation C1.1.[55] The parameters for this equation are listed in Figure C1 and were extracted from the spectral peaks using built-in microprobe software. Some examples of these parameters for elements Si and Er are listed in Table C1. These numbers are the result of averaging over 20 samples. Table C2 shows the uncertainties for the elements.

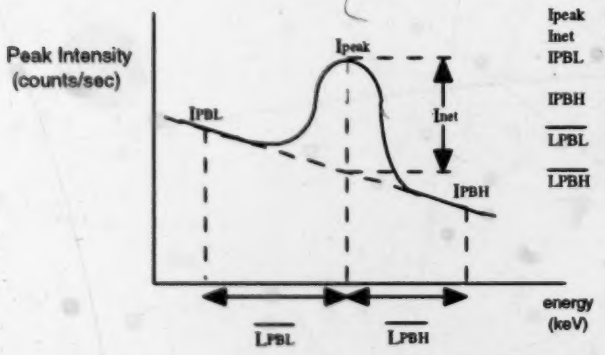

Ipeak = X-ray intensity at peak (cps)
Inet = Net X-ray intensuty (cps)
IPBL = Background X-ray intensity (cps) *low angle side.*
IPBH = Background X-ray intensity (cps) *high angle side.*
$\overline{LPBL}$ = Background measurement distance *low angle side*
$\overline{LPBH}$ = Background measurement distance *high angle side.*

Figure C1
Statistical way to determine number of counts in an elemental peak.

$$Inet = Ipeak - \frac{IPBH \times \overline{LPBL} + IPBL \times \overline{LPBH}}{\overline{LPBL} + \overline{LPBH}} \quad \text{(C1.1)}$$

	Ave weight % over 20 points	Oxide Weight %	I_peak Ave (cps)	I_PBL Ave (cps)	I_PBH Ave (cps)	L_PBL	L_PBH	I_net (cnts)	uncertainty n^(-1/2)	uncertainty as a function of weight %
Silicon	25.26	54.03	7488.38	36.00	25.70	5.00	5.00	7457.53	0.01	0.29
Erbium	2.71	3.10	106.38	35.90	32.80	1.50	1.50	72.03	0.12	0.32

Table C1 Example microprobe data from Si and Er for uncertainty calculations.

	O	Si	La	Na	Ba	Er	Zn	K	Ce	Cl *impurity*
Source:	N/A	0.26	0.99	0.35	0.46	0.33	0.37	0.13	0.10	N/A
Centre:	N/A	0.29	0.90	0.30	0.37	0.32	0.28	0.12	0.08	N/A
Edge:	N/A	0.28	1.02	0.33	0.45	0.34	0.30	0.12	0.16	N/A

Table C2 Statistical uncertainty in microprobe measurements for all elements.